Study of Lorentz Effect Imaging and Neuronal Current MRI Using Electromagnetohydrodynamic Models

by

Navid Pourtaheri

Department of Biomedical Engineering
Duke University

Date:_____
Approved:

_____
Craig S. Henriquez, Supervisor

_____
Trong-Kha Truong

_____
Warren M. Grill

_____
Angel V. Peterchev

_____
Linda Leithe-Gray

Dissertation submitted in partial fulfillment of
the requirements for the degree of Doctor of Philosophy in the Department of
Biomedical Engineering in the Graduate School
of Duke University

2013

ABSTRACT

Study of Lorentz Effect Imaging and Neuronal Current MRI Using

Electromagnetohydrodynamic Models

by

Navid Pourtaheri

Department of Biomedical Engineering
Duke University

Date:_____
Approved:

_____
Craig S. Henriquez, Supervisor

_____
Trong-Kha Truong

_____
Warren M. Grill

_____
Angel V. Peterchev

_____
Linda Leithe-Gray

An abstract of a dissertation submitted in partial
fulfillment of the requirements for the degree of Doctor of Philosophy in the
Department of Biomedical Engineering in
the Graduate School of Duke University

2013

Copyright by
Navid Pourtaheri
2013

Abstract

Neuronal current MRI (ncMRI) is a field of study to directly map electrical activity in the brain using MRI, which has many benefits over functional MRI. One potential ncMRI method, Lorentz effect imaging (LEI), has shown promise but needs a better theoretical understanding to improve its use.

We develop three computational models to simulate the LEI experiments of an electrolyte filled phantom subject to a current dipole based on: ion flow, particle drift, and electromagnetohydrodynamics (EMHD). With comparative experimental results, we use the EMHD model to better understand the Lorentz effect over a range of current strengths. We also quantify the LEI experimental images and assess ways to measure the underlying current strength, which would greatly benefit comparative brain mapping.

EMHD is a good predictor of LEI signal loss. We can measure the underlying current strength and polarity in the phantom using LEI images. We can also use trends from the EMHD model results to predict the required current density for signal detection in future LEI experiments. We can also infer the electric field strength, flow velocity, displacement, and pressure from the predicted current magnitude in an LEI experiment.

The EMHD model provides information that greatly improves the utility and understanding of LEI. Future study with our EMHD model should be performed using shorter dipole lengths, higher density and lower strength of current sources, and varying current source frequencies to understand LEI in the setting of mapping brain activity.

Dedication

I would like to dedicate this dissertation and the successful completion of the PhD to my father, who taught me the importance of hard work.

I would also like to recognize my mother for teaching me compassion and sociability, my grandmother for her magnificent spirit and helpful prayers, and my brothers for their constant belief, support, and relief.

Table of Contents

Abstract iv

List of Tables ix

List of Figures x

Acknowledgements xii

1. Noninvasive brain imaging and MRI 1

1.1. Neuronal current MRI (ncMRI) 3

1.2. Lorentz effect imaging (LEI) vs. BOLD-fMRI 4

1.2.1. Hemodynamic changes and BOLD-fMRI 4

1.2.2. The MRI signal and transverse relaxation 7

1.2.3. The LEI protocol 11

1.3. LEI progress in experiments 12

2. Modeling LEI contrast 25

2.1. Computational model of an electrolyte phantom 25

2.1.1. Model assumptions 26

2.1.2. Computing the electric field 29

2.2. The Lorentz effect in electrolyte solutions 32

2.2.1. Lorentz effect on electrical currents 33

2.2.2. Lorentz effect on ions 34

2.2.3. Lorentz effect on conductive fluids 35

2.2.3.1. Particle drift 36

2.2.3.2. Electromagnetohydrodynamics 37

2.3. Computing phase shift and signal loss 38

2.3.1. Phase shift accumulation from displacement 40
2.3.1.1. Particle tracking method 40
2.3.1.2. Reynolds transport method 44
2.3.2. Signal contribution from phase shift 46
2.3.3. Relative signal strength 47
3. EMHD and particle drift 48
3.1. Inter-model comparison methods 48
3.2. Study of EMHD flow results 51
3.3. Discussion of the EMHD flow effect and particle drift 64
4. Model and experiment LEI image comparison 69
4.1. Model and experiment image generation 69
4.2. Computational model and experimental phantom LEI image comparison 71
4.3. Discussion of computational LEI models 78
5. Measuring current strength and fluid dynamics with LEI based on EMHD 83
5.1. Measuring current strength using the LEI signal 84
5.2. Estimating fluid dynamics from the LEI signal 93
5.3. Discussion 99
6. Conclusions and future work 105
6.1. Summary of EMHD in LEI 105
6.2. Future methods to improve model accuracy 108
6.2.1. Computational phantom model 109
6.2.2. Flow effects 110
6.2.3. Noise and SNR 110
6.3. Future EMHD model studies of LEI in the brain 111

6.3.1. Shorter dipole length 112
6.3.2. Higher density and smaller strength of current sources 113
6.3.3. Varying firing rates and gradient widths 115
6.3.4. Restricted spaces 116
6.4. Discussion 119
Appendix: MATLAB function code m-files 120
MHD_Square.m 120
MHD_SquareTimed.m 157
avg.m 163
K1.m 164
rsize.m 165
ang2.m 166
circle.m 167
exbound.m 168
imageFOV.m 170
LEIcompare.m 173
dispimg.m 175
Works Cited 177
Biography 183
Publications and presentations from graduate work 184

List of Tables

Table 2.1: Potential Lorentz force interactions within the electrolyte phantom 33

Table 3.1: Particle drift model mean and maximal velocity, displacement, and relative signal change for 5 mA current pulses 53

Table 3.2: Fluid velocity updates for each term in the EMHD model 60

Table 4.1: EMHD model mean and maximal velocity, displacement, and signal loss for ±5 mA current pulses 72

Table 4.2: EMHD model mean and maximal velocity, displacement and signal loss for 0.5 mA current pulses 76

List of Figures

Figure 1.1: Time-response of BOLD-fMRI compared to neuronal activity 2

Figure 1.2: BOLD-fMRI blood oxygenation during rest and activity 6

Figure 1.3: MRI scanner cutaway diagram 8

Figure 1.4: MRI transverse relaxation 9

Figure 1.5: LEI vs. fMRI contrast based on transverse relaxation 10

Figure 1.6: Lorentz effect imaging pulse sequence diagram 11

Figure 1.7: First results of LEI in a gel and copper wire phantom 13

Figure 1.8: LEI signal profiles from the gel and copper wire phantom 14

Figure 1.9: MRE protocol used to detect displacements as small as 0.1 μm 15

Figure 1.10: LEI activation map showing neuroelectric activity *in vivo* along the human median nerve 17

Figure 1.11: MRI signal time response of the LEI vs. BOLD-fMRI 18

Figure 1.12: LEI of a gel phantom with randomly oriented carbon wires 20

Figure 1.13: Electrolyte phantom imaged in LEI experiments 22

Figure 1.14: LEI of ionic currents in $CuSO_4$ solution 23

Figure 2.1: Formation of the computational model phantom domain 27

Figure 2.2: Computational model representation of a square electrolyte phantom 28

Figure 2.3: Electrical potentials within the computational phantom model for current strength of 5 mA 32

Figure 3.1: LEI protocol used in the computational models 49

Figure 3.2: Lorentz force induced flow velocity from electromagnetic drift 52

Figure 3.3: Particle drift model mean velocity and displacement over time 55

Figure 3.4: EMHD model mean velocity and displacement over time 57

Figure 3.5: Particle drift model maps of the electric field, relative signal change, velocity, and displacement for a 5 mA current pulse 59

Figure 3.6: Direction and distribution of flow velocity, displacement, and pressure after updates from each component of the EMHD model for a single time step 62

Figure 4.1: Experimental signal image and EMHD maps of signal, velocity, and pressure for a 5 mA current pulse 73

Figure 4.2: Experimental signal image and EMHD maps of signal, velocity, and pressure for a -5 mA current pulse 75

Figure 4.3: Experimental signal image and EMHD maps of signal, velocity, and pressure for a 0.5 mA current pulse 77

Figure 5.1: EMHD model and experiment relative signal change in the phantom over a range of current strengths..... 86

Figure 5.2: EMHD model and experiment proportion of the total relative signal change in different regions of the phantom over a range of current strengths 88

Figure 5.3: EMHD model and experiment percentage of voxels with relative signal change below a -40% threshold in different regions of the phantom over a range of current strengths..... 90

Figure 5.4: Measured current strength from LEI experiment images using SRLT and comparison with EMHD model results..... 92

Figure 5.5: EMHD model and LEI experiment predicted electric field, velocity, and displacement magnitudes over a range of currents strengths..... 94

Figure 5.6: EMHD model and LEI experiment predicted pressure magnitude over a range of current strengths 96

Figure 5.7: EMHD model and LEI experiment predicted electric field, velocity, and displacement magnitudes over a range of currents strengths..... 97

Figure 5.8: EMHD model and LEI experiment predicted pressure magnitude for a range of SRLT 98

Figure 6.1: Summary of EMHD model and LEI experiment results in an electrolyte phantom..... 107

Acknowledgements

I would like to acknowledge the Duke University Department of Biomedical Engineering and my advisor Craig Henriquez for allowing me the opportunity to accomplish this tremendous undertaking. I would also like to thank Trong-Kha Truong and the rest of my esteemed committee for their support and feedback towards the successful completion of this dissertation.

I also am thankful for the Duke University School of Medicine, for providing me with wonderful mentors and tremendous personal and academic growth that has contributed to my success in this work and will continue to do so in my future career.

I would also like to recognize the financial support of grants R01EB009483 and R01EB012586 from the National Institutes of Health.

1. Noninvasive brain imaging and MRI

The "holy grail" of human brain imaging [1] has been described as a non-invasive technique that allows direct mapping of brain activity with a spatial resolution on the order of a cortical column (100 μm x 100 μm [2]) and temporal resolution on the order of a postsynaptic potential (10 msec [2]) or even an action potential (1 msec [2]).

Non-invasive recording of local electrical fields from neuronal tissue has long been accomplished using scalp EEG [3-5]. EEG has great temporal resolution on the order of milliseconds, but has major limitations in spatial resolution and depth, thereby making it an effective means for cortical mapping [6].

MRI on the other hand, has high spatial resolution on the order of millimeters with good depth of analysis providing anatomic images with no data on brain activity [6, 7]. Cerebrovascular blood volume (CBV) functional MRI (fMRI) [7] and blood oxygenation level dependent (BOLD) fMRI [8-12] are methods used to overlay maps of brain function based on hemodynamic changes and have some recent use in mapping brain activity [13]. The recorded hemodynamic changes in fMRI are limited by a timescale of 5-6 seconds [14, 15], and do not directly correlate with or match the time-scale of most brain activity, thereby making fMRI unable to aid in critical decisions in the absence of direct brain mapping [1, 16-18].

By comparing BOLD-fMRI activity maps to microelectrode recordings of local field potentials showing activity spikes in the occipital cortex, there is a lack of correlation and extended time scale of the BOLD response compared to the neuronal activity [15], shown in the figure below.

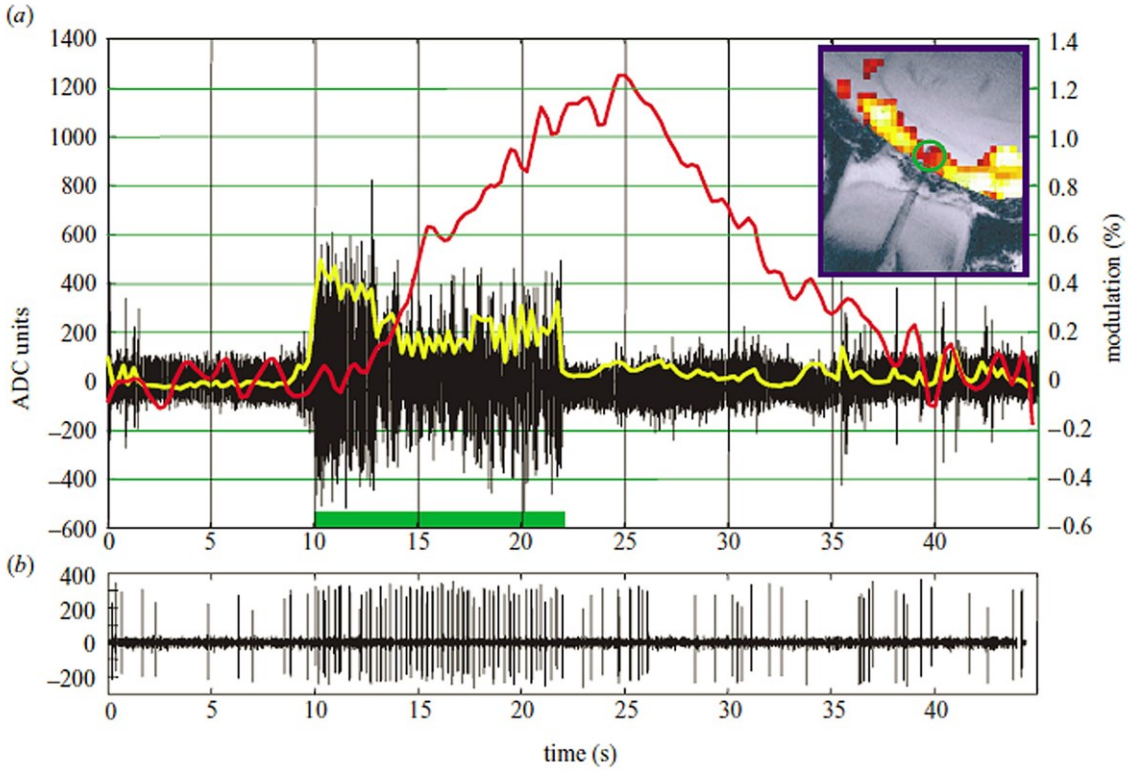

Figure 1.1: Time-response of BOLD-fMRI compared to neuronal activity
From Logothetis 2002 [15]. Visually evoked response recorded using BOLD-fMRI and concurrent local field potential (LFP) from microelectrodes in the occipital cortex. (a) Comprehensive signal from LFP recording of neural signaling (black: raw, yellow: RMS). BOLD response (red) from average time-series of voxels within green circle of T2*-weighted image in the inset, showing a maximum BOLD-fMRI signal change on the order of 1.2% with its peak occurring several seconds after the end of the stimulus presentation period (green horizontal bar). (b) Action potential sequence from the comprehensive signal, isolated using statistical methods, with a rate that reflects the output response activity of the studied area.

In Figure 1.1 microelectrode recordings show that the neuronal activity response has an increased firing rate over a period of time that coincides exactly with the visual stimulus presentation period. The BOLD signal on the other hand has a period twice that of the stimulus presentation period, is delayed in onset, and does not reach its peak until several seconds after the end of the visual stimulus presentation period [15].

In addition, BOLD-fMRI uses large voxel sizes to enhance the MRI signal modulation (on the order of 1% even with large voxels) and decrease scan time, which results in the images of the hemodynamic response within a relatively large area (100,000 neurons and billions of synapses) compared to the resolution of specific neurons creating the output activity [15, 18-20]. Furthermore, the area of measured BOLD response is widened by the downstream flow of blood from the area of increased activity, thereby limiting spatial interpretation of the BOLD-fMRI images [15, 19].

Therefore, a non-invasive brain imaging modality is needed with a contrast mechanism that has improved temporal and spatial correlation with the underlying brain activity over BOLD-fMRI.

1.1. Neuronal current MRI (ncMRI)

To improve the accuracy of neuronal activity dependent imaging, several methods have been proposed to combine the high spatial resolution of MRI with the high temporal resolution of EEG [3, 10]. It is ideal to use the high spatial resolution of MRI to directly map neuroelectrical activity in the brain. However, as opposed to inferring brain activity indirectly from relatively slow hemodynamic changes as in fMRI, an imaging contrast mechanism is needed that has higher temporal correlation and resolution approaching that of EEG, a field of study referred to as neuronal current MRI (ncMRI) [1].

ncMRI has been described as the holy grail of functional neuroimaging for directly imaging neuroelectrical activity, yet its theory and feasibility are still a topic of

debate [1]. In the past fifteen years, a variety of methods have been performed for the study of MRI mapping and modeling of electrical activity in brain [21-33], nerve [32, 34-36], and phantoms [37, 38]. Many of these methods attempt to neuronal current induced inhomogeneities in the magnetic field, referred to as neuromagnetic fields (NMFs), which are on the order of 10^{-14} – 10^{-12}T [39]. Currently NMFs are undetectable using MRI because their magnitude is far smaller than the inhomogeneities of most MRI magnets, and therefore require special devices for detection called SQUID magnetometers (superconducting quantum interference devices) with very limited spatial resolution [39].

1.2. Lorentz effect imaging (LEI) vs. BOLD-fMRI

More recently, one form of ncMRI called Lorentz Effect Imaging (LEI) [16, 40-42] was introduced, which employs oscillating magnetic field gradients to amplify and detect the signal loss resulting from a spatially incoherent, yet temporally synchronized, water displacement caused by the neuronal activity. To depict the significance of LEI (as an ncMRI method) we will compare the physics underlying how the MRI signal is being generated in BOLD-fMRI vs. LEI.

1.2.1. Hemodynamic changes and BOLD-fMRI

The BOLD signal in fMRI takes advantage of the change in magnetic properties of hemoglobin (Hb) [15, 19]. When Hb is oxygenated (oHb) it is diamagnetic and causes little magnetic field change versus deoxygenated (dHb) which is paramagnetic and causes

a greater magnetic field change [43]. The oxygen itself is used in cellular respiration to generate ATP that is used by ion channels during cell rest and activity, and is supplied by the Hb in red blood cells that travel through capillaries from the arterial (oxygenated) to venous (deoxygenated) circulation [19].

In response to neuronal activity, cellular metabolism releases vasoactive agents that increase blood flow to meet the increased oxygen demand. This increase in blood flow "overshoots" the required demand causing a higher ratio of oHb:dHb than in the resting state [19, 20].

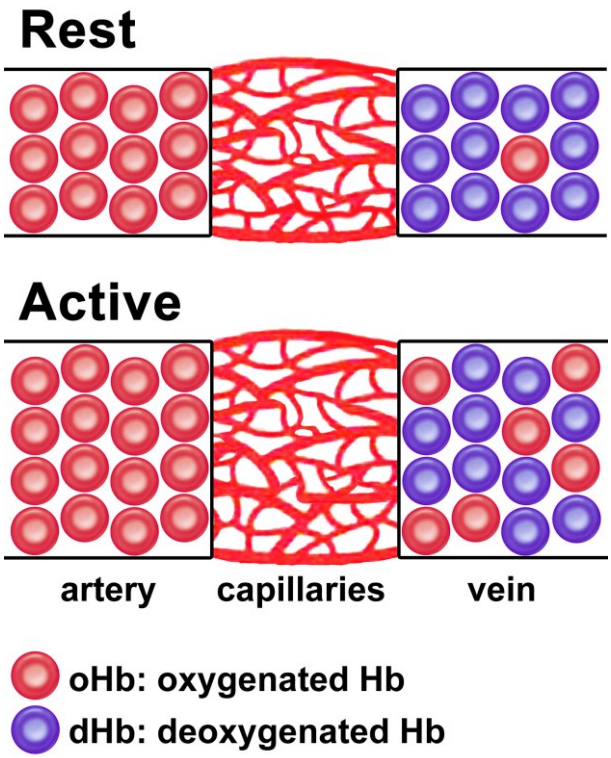

Figure 1.2: BOLD-fMRI blood oxygenation during rest and activity
Oxygen is supplied to neurons from hemoglobin (Hb) in red blood cells through capillaries. During periods of rest, neuronal activity is matched to the incoming arterial blood supply where the majority of oxygenated Hb (oHb) leaves as deoxygenated (dHb) with a low venous oHb:dHb ratio (low BOLD signal). During periods of activity spikes, neuronal metabolism produces vasoactive agents that increase blood flow to meet the increased oxygen demand. The overshoot in blood flow causes a higher oHb:dHb ratio in the outgoing venous blood and therefore a relative increase in the BOLD signal.

The venous oHb:dHb ratio is higher in the active state due to increased blood flow, a process which occurs over several seconds [15]. The local magnetic field changes from Hb are less in the active state than at rest because there is a lower proportion of paramagnetic dHb in the venous blood. As a result, the BOLD MRI protocol is one that maximizes T2* signal loss from magnetic field inhomogeneities [14], which we will explain next.

1.2.2. The MRI signal and transverse relaxation

An MRI signal is recorded from the radio waves or energy that is released from the relaxation of water proton magnetic moments (spins) occurring in the radio frequency (RF) spectrum. At rest, proton spins align with the scanner's strong magnetic field (along the z-axis) in a parallel or anti-parallel fashion. An RF pulse is then applied to knock spins out of their z-axis orientation into the transverse plane. After a certain amount of time, the spins return from the transverse plane to their z-axis orientation. The total MRI signal is proportional to the alignment of all the proton magnetic moments in the tissue.

Below is a cutaway diagram of a typical MRI scanner which has a hollow bore magnet, magnetic gradient coils, and an RF coil used to detect the MRI signal.

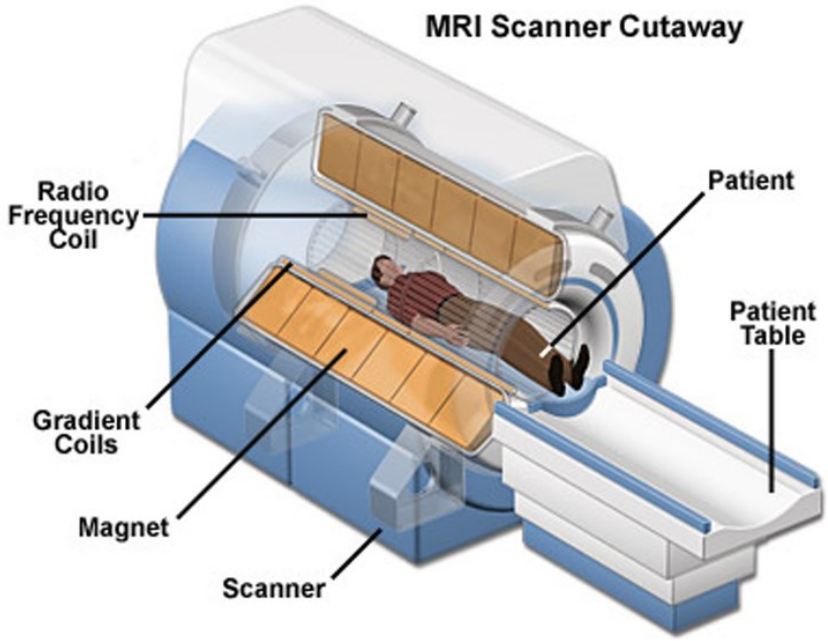

Figure 1.3: MRI scanner cutaway diagram
From Coyne [44]. MRI scanner has a hollow bore magnet that produces a magnetic field oriented along the longitudinal (z-axis). Gradient coils in the scanner introduce linear magnetic field variations with strength (slope, dB/d**x**) on the order of mT/m in the x, y, and z directions. The RF coil is used to flip the proton magnetic moment spins in the subject and subsequently record the radio waves emitted when they relax.

Proton spins precess at a frequency based on the magnetic field strength, referred to as the Larmour frequency [45]. If two proton spins are slightly different, they become out of phase with one another, referred to as dephasing. If enough dephasing accumulates over time, the recorded MRI signal magnitude is less. T1 or spin-lattice relaxation refers to longitudinal dephasing of spins from their interactions with the surrounding tissue or lattice [15, 45]. T2 or spin-spin relaxation refers to transverse dephasing of spins from their interactions with one another [15, 45]. A different cause of transverse relaxation, referred to as T2*, is from small magnetic field inhomogeneities affecting precession

frequencies which cause dephasing over time, and is the basis of the BOLD signal [15]. Transverse relaxation is shown in the diagram below.

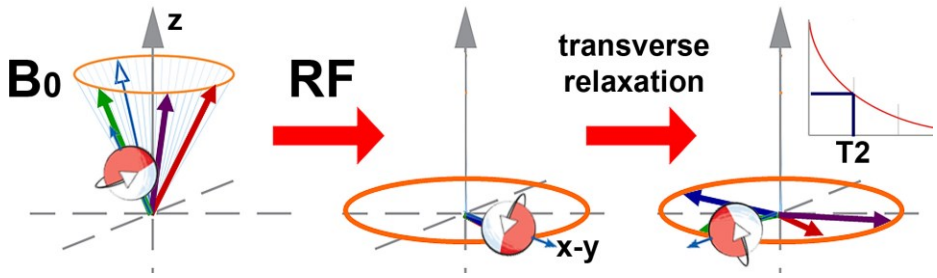

Figure 1.4: MRI transverse relaxation
A proton's magnetic moment (red is the + pole, white is the - pole) is oriented with the MRI scanner's magnetic field (of strength B_0) along the z-axis. An RF pulse is applied to knock the proton moment spin axes (depicted by vectors) into the transverse x-y plane. Over time due to perturbations in their precession frequencies, the spins become out of phase with one another in the x-y plane, referred to as dephasing or transverse relaxation. Dephasing from spin-spin interactions is referred to as T2 relaxation. The corresponding T2 signal decay over time is shown.

Figure 1.4 above depicts a proton's magnetic moment aligning along the z-axis with the scanner's magnetic field (B_0). The RF pulse is applied to knock the spin orientations into the transverse plane. The spins gradually become out of phase with one another, referred to as transverse relaxation, which causes the MRI signal to decay over time [45]. Similar to T2 relaxation, T2* relaxation is from magnetic field inhomogeneities causing the difference in precession frequency and hence phase shift accumulation over time [15, 45].

In BOLD-fMRI gradient echo pulse sequences are used to enhance the detected signal decay from T2* relaxation due to magnetic field inhomogeneities from dHb [14]. Like BOLD, LEI depends on dephasing in the transverse plane but the mechanism is different. In LEI transverse spin dephasing accumulates over time due to Lorentz-force

induced particle displacements along spatial magnetic field gradients [41]. Displacement causes the proton spins to change precession frequency as they move along the gradients which is an externally introduced a magnetic field inhomogeneity on the order of mT/m. Below is a diagram depicting the difference between transverse relaxation in LEI vs. BOLD-fMRI.

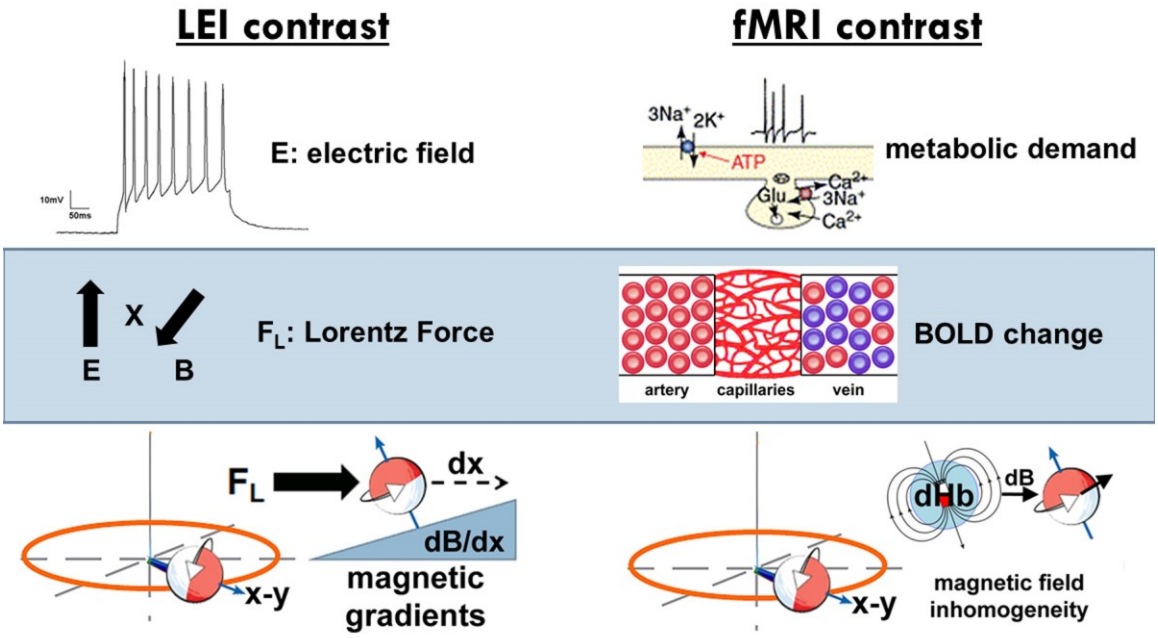

Figure 1.5: LEI vs. fMRI contrast based on transverse relaxation
LEI contrast (figure left) is a function of neuronal electric fields (**E**) occuring under the MRI scanners magnetic field (**B**) causing a Lorentz force ($\mathbf{F_L}$) which displaces protons (**dx**) along spatial magnetic gradients (dB/d**x**) that result in dephasing in the transverse plane. BOLD-fMRI contrast (figure right) is a function cellular metabolic demand causing blood oxygenation level (BOLD) changes that result in magnetic field inhomogeneities from paramagnetic deoxygenated hemoglobin (dHb) causing dephasing in the transverse plane. See Figure 1.4 for a diagram of transverse relaxation leading to MRI signal decay.

1.2.3. The LEI protocol

In fMRI, as described above, gradient echo is used to enhance T2* dephasing from magnetic field inhomogeneities. In LEI however, electrical activity matched gradient oscillation is used to amplify dephasing from the displacement of water protons due to the Lorentz force. Figure 1.6 below depicts a typical LEI protocol synchronized to detect square wave electrical current pulses applied to a model phantom. The LEI pulse sequence is a gradient echo sequence [46] with oscillating magnetic field gradients between excitation and data acquisition, synchronized to the electrical current activity.

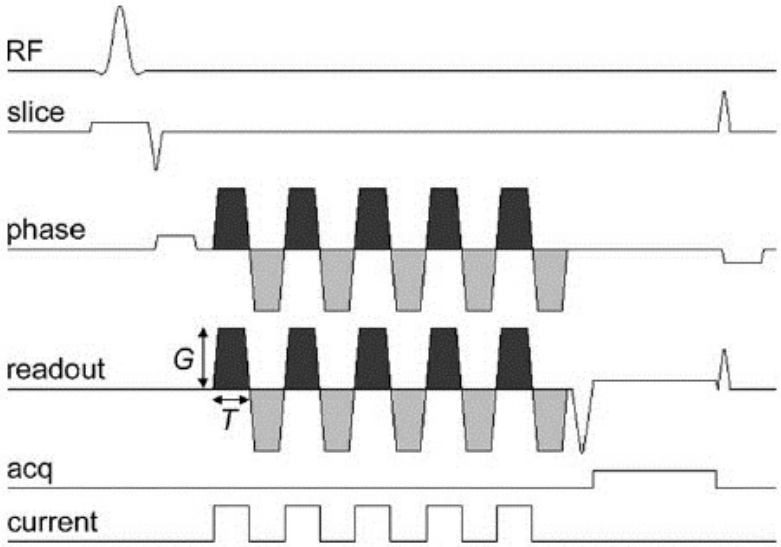

Figure 1.6: Lorentz effect imaging pulse sequence diagram
From Truong, Wilbur, and Song 2006 [41]. Gradient echo sequence with *n* cycles (5 in this case) of oscillating magnetic field gradients, with positive and negative lobes of amplitude *G* and duration *T*, shown in dark and light gray, respectively, applied in the readout and phase encoding directions between radiofrequency (RF) excitation and data acquisition. The applied current pulses in this case are synchronized with the positive gradient lobes.

Ideally, *in vivo*, the oscillating gradients would be synchronized to the frequency of the neuronal currents of interest such that the electrical activity causing the incoherent

water displacement occurs during the positive gradient lobes, but not during the negative gradient lobes (or inversely). For particles experiencing displacement between the opposing gradient lobes, such oscillating gradients enhance the incoherent spin phase shift accumulation from the spatially incoherent water displacement occurring, resulting in a maximal signal loss in the voxels of interest. Whereas, particles not experiencing displacement would be dephased during the positive lobes and equally rephased during the negative lobes, thereby achieving a phase shift of zero and no signal change.

The LEI technique has successfully been used to detect electrical activity in various phantoms [40-42] and in the human median nerve *in vivo* [16] , which represents a promising step towards its application for detecting neuronal activity in the brain.

1.3. LEI progress in experiments

LEI was first introduced by Song and Takahashi in 2001 in a study of electrical current pulses applied to a copper wire embedded in a cylindrical gel phantom. Using opposing gradient lobes, an encoding gradient applied before the current pulse and a decoding gradient applied after the pulse, they detected an area of signal loss surrounding the wire that could be widened by applying higher currents, with the direction of widening in the direction of the Lorentz force [40] (Figure 1.7 and Figure 1.8 below). The phantom was 3 cm in diameter and 5 cm in length with a soft stranded 1.5 mm diameter copper wire inserted horizontally across the phantom, externally connected to a square wave pulse generator. The LEI experiment was performed using a 7 T small bore magnet

with x-axis encoding and decoding gradients with strength of G_x = 50 mT/m and lobe duration of T = 2 msecs.

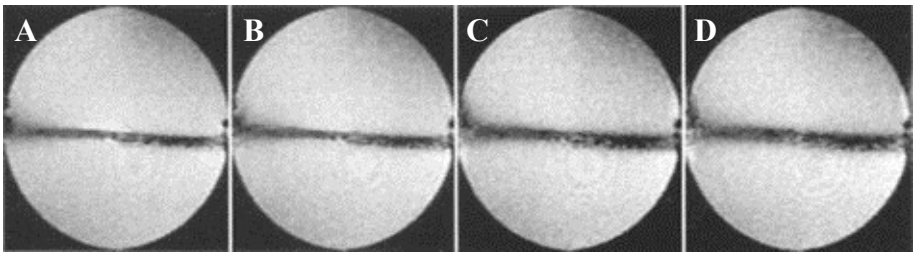

Figure 1.7: First results of LEI in a gel and copper wire phantom
From Song and Takahashi 2001 [40]. Axial LEI images of a 3 cm diameter 5 cm length cylindrical gel phantom with an inserted 1.5 mm diameter stranded copper wire connected to a square pulse generator. The four images shown from left to right are with applied currents of **A**. 0 μA, **B**. 100 μA, **C**. 200 μA, and **D**. 500 μA. The signal loss along the central axis of A is due to the presence of the wire, with a gradual widening of the central gap in B-D caused by the increasing intra-voxel dephasing from the Lorentz force-induced spatial displacement.

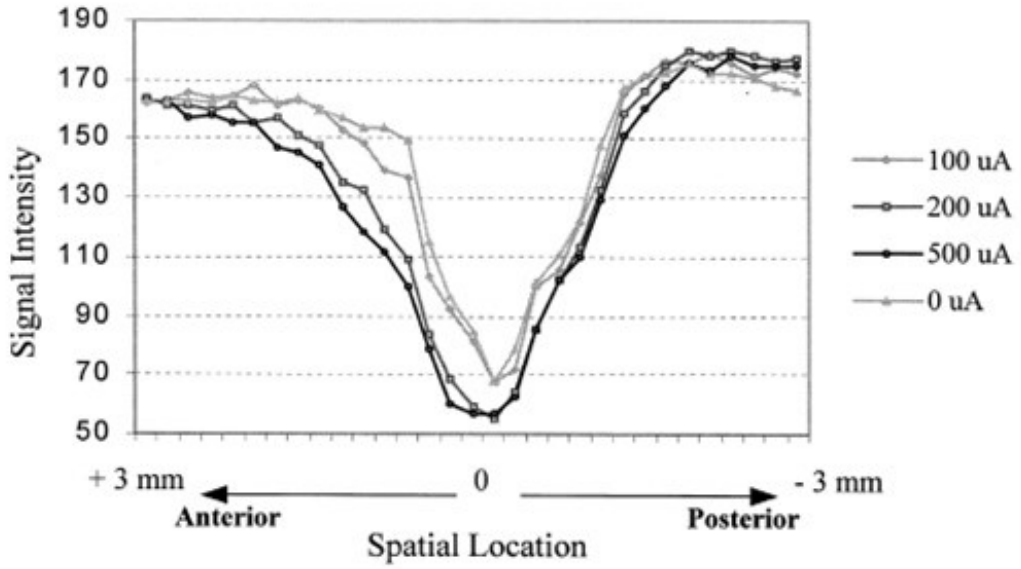

Figure 1.8: LEI signal profiles from the gel and copper wire phantom
From Song and Takahashi 2001 [40]. Collapsed signal profiles of the LEI images from Figure 1.7 showing a central dip with gradual widening due to stronger Lorentz effects as the current was increased from 0 – 500 μA, with the direction of widening toward the anterior part of the phantom, indicating the direction of the Lorentz force.

In 2005, Basford et al. studied Lorentz force induced motion in conductive physiologic media under an MRI magnetic field [47] using a magnetic resonance elastography (MRE) protocol. MRE is an MRI technique that uses motion-sensitized time-gated phase contrast to image mechanically induced cyclic displacements as small as 0.1 μm [48-51]. The MRE protocol shown below is similar to the LEI protocol in Figure 1.6, with oscillating gradient pulses synchronized to trigger pulses, except that in MRE the trigger pulses control a pulse wave generator used to create mechanical motion via an actuator coil versus in the LEI protocol current pulses are applied directly to the subject to create a Lorentz force.

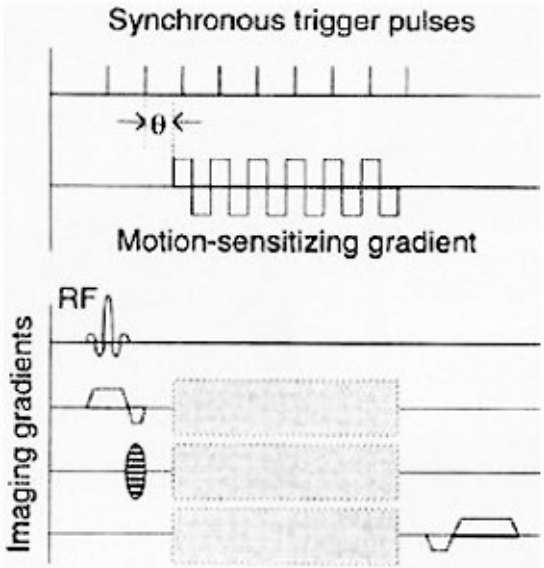

Figure 1.9: MRE protocol used to detect displacements as small as 0.1 µm
From Muthupillai et al. 1996 [48]. In this magnetic resonance elastography (MRE) protocol motion-sensitizing oscillating magnetic gradients are applied between radiofrequency (RF) excitation and acquisition, and are synchronized to triggering of an actuator inducing motion in the imaged gel. Gel displacements as small as 0.1 µm were imaged using this technique.

In 2005, using an MRE protocol in a 1.5 T scanner, Basford et al. acquired images of Lorentz force induced motion in homogenous (25% NaCl 2% agar and 25% NaCl 18% bovine gelatin) and nonhomogeneous (layering of 0%-0.9%-0% NaCl 2% agar slabs) gels assembled in a 12.75x10.25x4 cm acrylic mold [47]. The Lorentz force was introduced by applying alternating sinusoidal currents (50 V, 100 Hz) via gold leaf electrodes across the gels under the scanner's magnetic field. In all cases, an alternating pattern of conductive gel displacement was observed, 65-75 µm in amplitude, perpendicular to the plane of the sample when the current was applied perpendicular to the magnetic field, while a random motion pattern was observed when the current flow was absent or parallel to the magnetic field [47]. This study showed that electrical currents in a physiologic

conductive media under an MRI magnetic field created displacements that were consistent with the direction of the Lorentz force (**J** x **B)** and on a scale (65-75 μm) that was detectable using MRI.

Displacements in MRE may be calculated by rearranging the equation describing the observed phase shift in the MRI signal [48]:

$$d = \pi\phi / \left[2\gamma nTG \cos\left(\mathbf{kx} + \theta \right) \right] \tag{1.1}$$

In this equation, d is the maximum displacement, $\mathbf{x}(t)$ is the position vector, $\mathbf{k}$ is the wave number, θ is an initial phase offset, γ is the gyromagnetic ratio (42.57×10^6 Hz/T), n is the number of gradient cycles, T is the period of mechanical excitation ($T = 2\pi/\omega$ secs), ω is the frequency of mechanical excitation (Hz), G is the gradient strength (T/m), and ϕ is the experimentally measured phase shift [48].

In 2006, Truong and Song showed LEI *in vivo* in the human median nerve. They applied a series of sub motor threshold (1.8 – 2.7 mA) current pulses at the wrist of a human volunteer in a 4 T whole body scanner using a LEI pulse sequence with gradient oscillations of strength G = 36 mT/m and lobe duration T = 5 msecs [16]. In this study, square current pulses of 1 msec duration were matched to the beginning of each of the negative lobes of three oscillating gradients during the stimulator on periods, alternated with the same conditions and the stimulator off. They were able to detect a relative signal loss of ~4% for the stimulator on versus off periods and showed an activation map that corresponded to the anatomic location of the median nerve [16] (Figure 1.10 below).

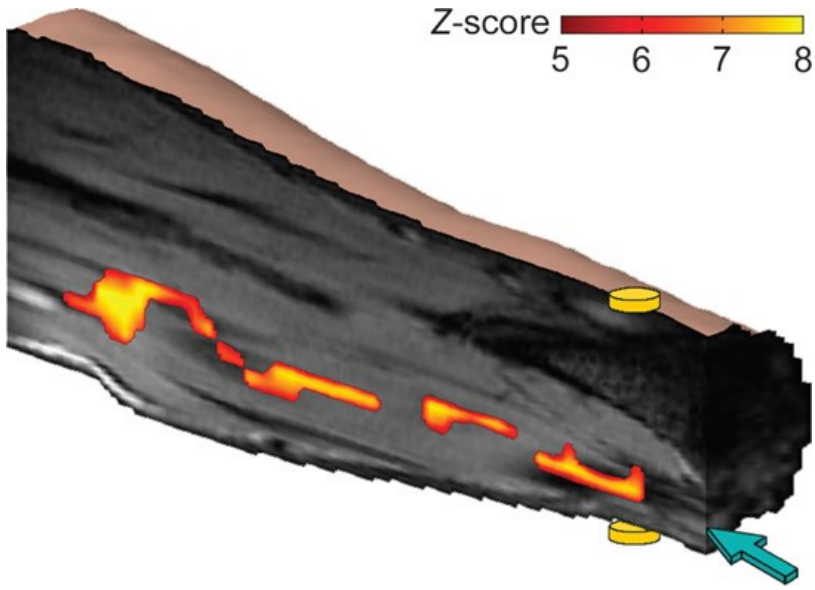

Figure 1.10: LEI activation map showing neuroelectric activity *in vivo* along the human median nerve
From Truong and Song 2006 [16]. The activation map was obtained using three cycles of oscillating gradients (G = 36 mT/m, T = 5 msecs) and sub motor threshold electrical pulses applied at the wrist synchronized with each of the negative gradient lobes. Map is overlaid on co-registered anatomical images. The discs represent the electrodes placed on the dorsal (top) and ventral (bottom) sides of the wrist. The arrow points to the median nerve.

The *in vivo* activity map above from LEI is superior to the BOLD-fMRI map based on the timescale of the signal response to the underlying stimulus period as shown in the figure below.

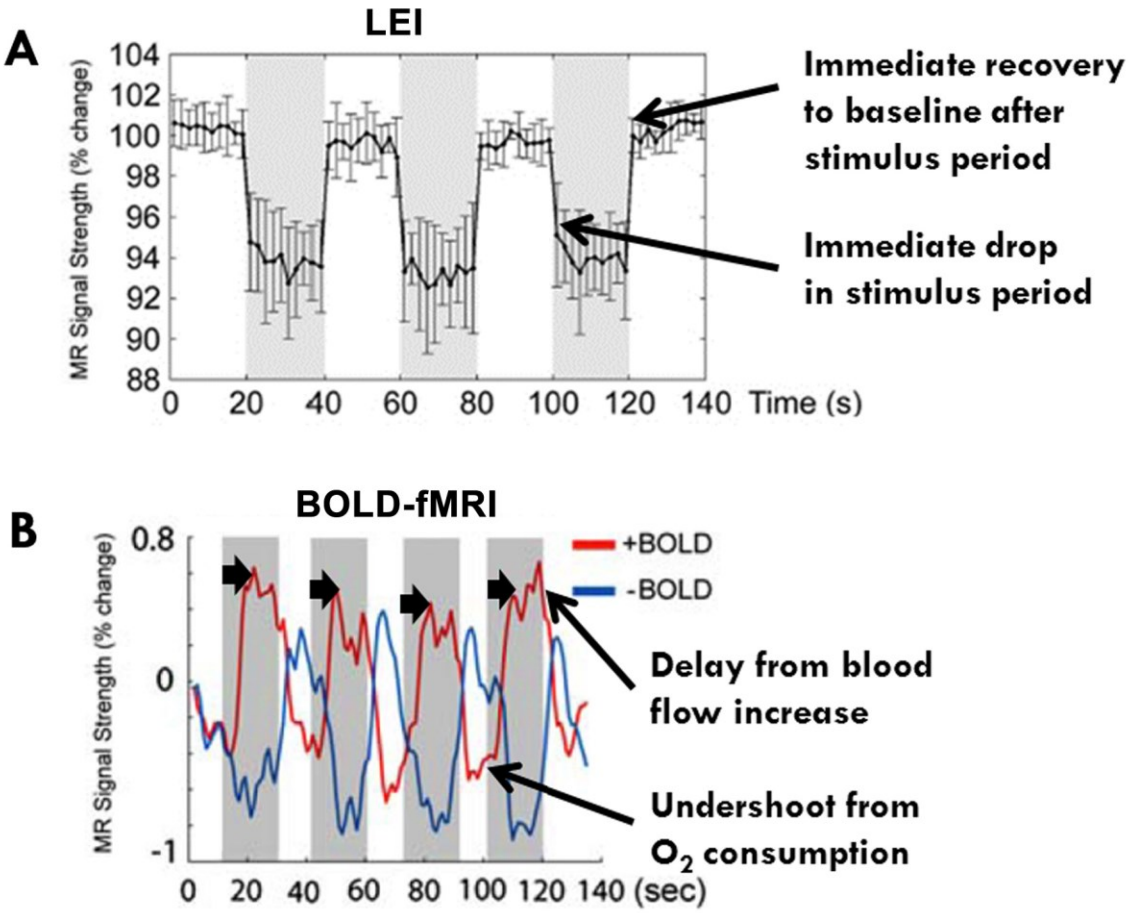

Figure 1.11: MRI signal time response of the LEI vs. BOLD-fMRI
A. From Truong and Song 2006 [16]. Time response of the spatially averaged LEI signal (shown in Figure 1.10) from sub-motor threshold stimulation of the median nerve. Stimulus periods are outlined in grey. LEI signal drops almost immediately with onset of the stimulus period, and recovers to baseline immediately after the end of the stimulus period. **B**. From Whittingstall et al. 2008 [11]. BOLD-fMRI signal averaged over a region of interest within the contralateral visual cortex after a visual stimulus if displayed. Stimulus presentation periods are outlined in grey. Black arrows point to the 5-6 second delay between the onset of the stimulus period and the peak of the BOLD signal due to time required to increase blood flow. There is also an undershoot after the end of the stimulus period due to oxygen consumption increasing venous dHb.

In Figure 1.11A above, the LEI signal shows an immediate change in relative signal of about 6% followed by an immediate return to baseline at the end of the stimulus period, whereas the BOLD-fMRI signal time response in Figure 1.11B shows a relative

signal change of about 1% that is delayed by 5-6 seconds in peak onset after the start of the stimulus period and has an undershoot before returning to baseline at the end of the stimulus period. Therefore there is less delay and better correlation with the underlying on/off activity of the neural response in the LEI signal compared to the BOLD-fMRI signal. Although the signal strength cannot be compared between the LEI signal which was acquired from an the response of a peripheral nerve due to an applied current and the BOLD-fMRI signal which was acquired from a region of interest in the brain due to a visual stimulus, the differing time response is significant and indicates the relative benefit of LEI over fMRI.

The demonstrated success of LEI *in vivo* in the human median nerve made the study of LEI promising. However, further study using more simplified models was warranted to understand the underlying LEI contrast mechanism and help optimize LEI protocols for future use based on the contrast mechanism.

In 2006, Truong, Wilbur, and Song performed a proof of concept study to evaluate the sensitivity of LEI for straight and randomly oriented currents conducted through carbon wires in a 10 cm diameter spherical gelatin phantom. The carbon wires helped reduce detection of the wire themselves seen in previous experiments [40]. Using a 4 T whole-body MRI scanner and a shielded quadrature birdcage head coil and an LEI pulse sequence (similar to that depicted in Figure 1.6) with n = 15, G = 40 mT/m, T = 2 msecs, square current pulses were applied to the wires connected in parallel. With this setup, mean signal losses up to 23% were detected for the randomly oriented electrical currents on the order of microamperes with a temporal resolution on the order of

milliseconds [41]. They concluded that the Lorentz force from the current in the wires caused an incoherent displacement of the water molecules in the surrounding gel, resulting in the observed signal loss [41].

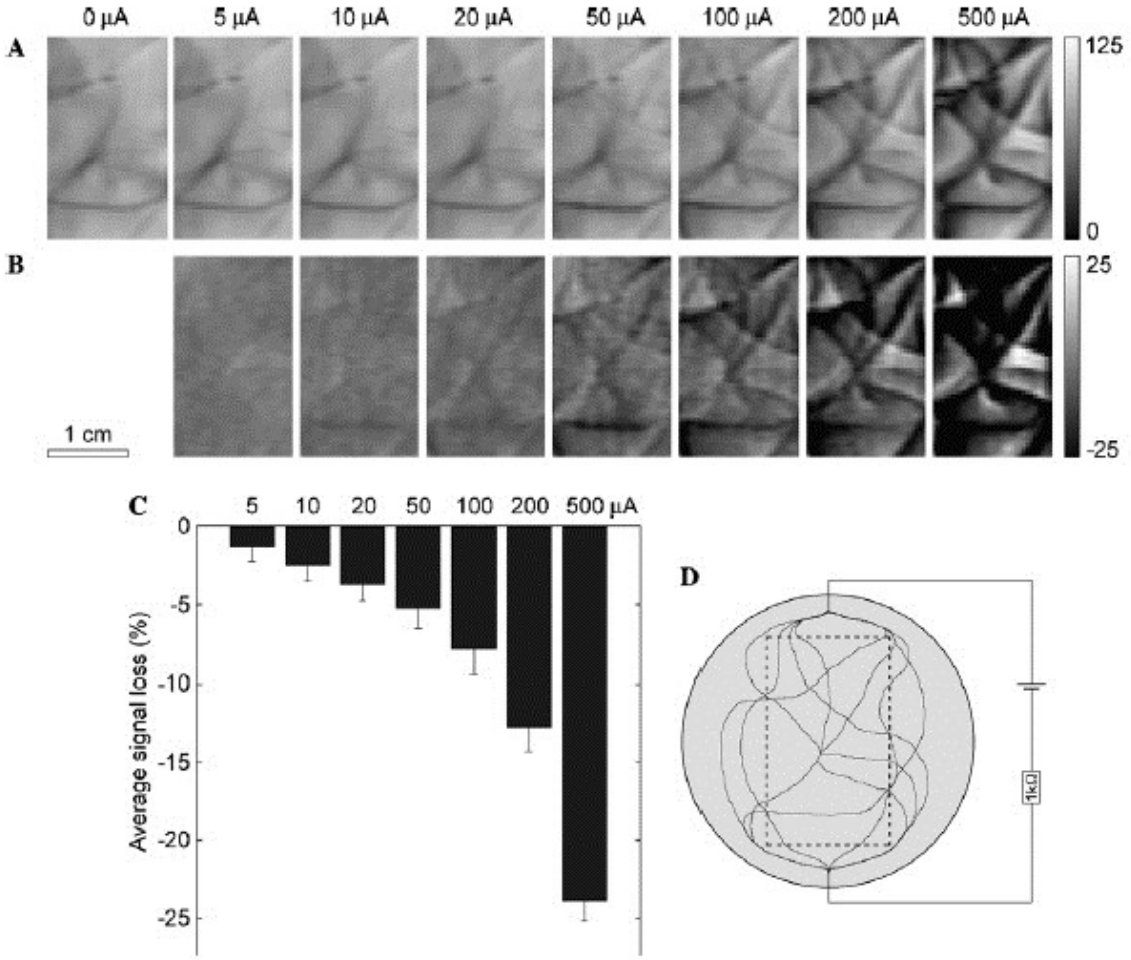

Figure 1.12: LEI of a gel phantom with randomly oriented carbon wires
From Truong, Wilbur, and Song 2006 [41]. LEI signal loss dependence on current density for randomly oriented currents. **A.** Selected region of signal images acquired for different current strengths in the dotted region of the phantom outlined in D. **B.** Difference images between that of A and those acquired with zero current. **C.** Signal loss averaged over the region shown in B. **D.** Schematic of the 10 cm diameter spherical gelatin phantom with randomly oriented carbon wires connected in parallel to a square pulse wave generator.

The LEI contrast mechanism in their study was described theoretically [41] using a cylindrical current-carrying conductor oriented along the y axis, placed in a magnetic field oriented along the z axis, surrounded by a homogeneous, isotropic, and linear elastic medium. They described that the resulting Lorentz force, oriented along the x axis and proportional to the current and the magnetic field, induces a displacement of the conductor, leading to a spatially incoherent displacement of the surrounding elastic medium in the same direction. Based on the elasticity problem using the Lorentz force as a body force in a cylinder that deforms the surrounding water molecules, they derived a mathematical expression for the ratio of signal intensity with and without the Lorentz effect. Using their calculations they showed that the phase shift (creating signal loss) is directly proportional to the Lorentz-force induced displacement [41].

In 2008, Roth and Basser created a mechanical model of neural tissue displacement to theoretical solve the elasticity problem for a nerve carrying an action current [52]. They wanted to study the *in vivo* median nerve results of Truong and Song using the proposed contrast mechanism involving the elasticity from their phantom model paper [16]. They approximated that the Lorentz-force induced nerve displacement in the *in vivo* median nerve experiments could only generate phase shifts of up to 0.1%, which is too small and diffuse to be measured using MRI [52]. In addition, they argued that this displacement spreads throughout the entire tissue, which dephases spins throughout the arm and not just near the nerve, therefore making localization of the nerve difficult [52].

In studying LEI contrast, gel and wire phantoms using metal or carbon wires carrying electron currents do not have the same properties as neurons with ionic currents

and therefore a better model was needed for further study. In 2008 Truong, Avram, and Song created a spherical electrolyte solution-filled phantom model with ionic currents as opposed to currents through a wire to study the underlying LEI contrast [42]. They applied square current pulses to wires that were placed just inside the phantom instead of all the way through, and showed that the Lorentz force from an electromagnetic field could also generate a force on ionic currents in the solution [42]. A diagram of the experimental phantom model of Truong et al. is shown below.

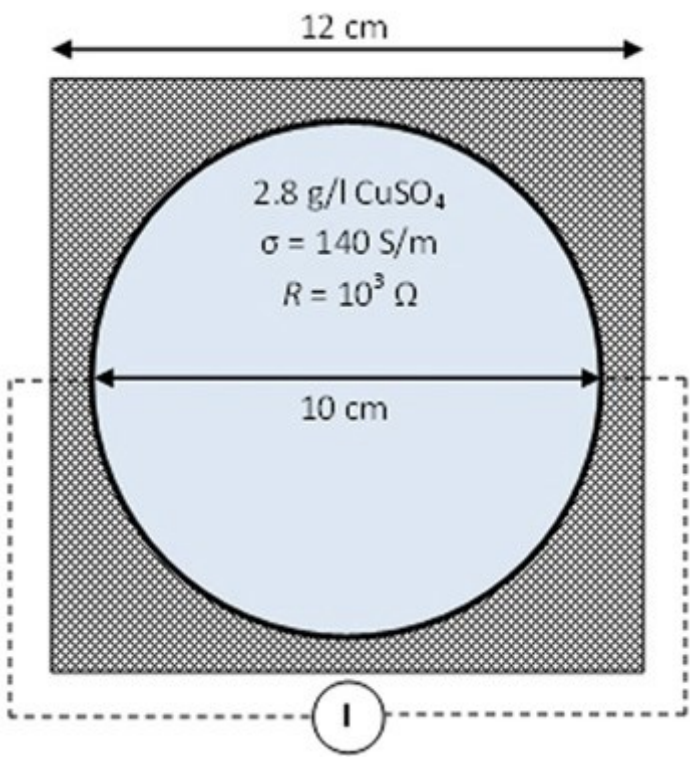

Figure 1.13: Electrolyte phantom imaged in LEI experiments
Diagram of the central slice of a 10 cm diameter spherical electrolyte phantom filled with 2.8 g/l $CuSO_4$ solution within a 12 x 12 cm MRI viewing domain. Wires were inserted into the left and right ends, with a current I applied by a square wave current pulse generator Phantom properties include inter-electrode resistance $R = 10^3\ \Omega$, homogeneous isotropic conductivity $\sigma = 140$ S/m, and magnetic permeability $\mu_m = -9*10^{-6}$ H/m.

The theoretical explanation included in this study simulated ion trajectories using experimentally derived mobility values and showed the trajectories for a series of ions moving through an area of the phantom that matched the area of signal loss in the experiments.

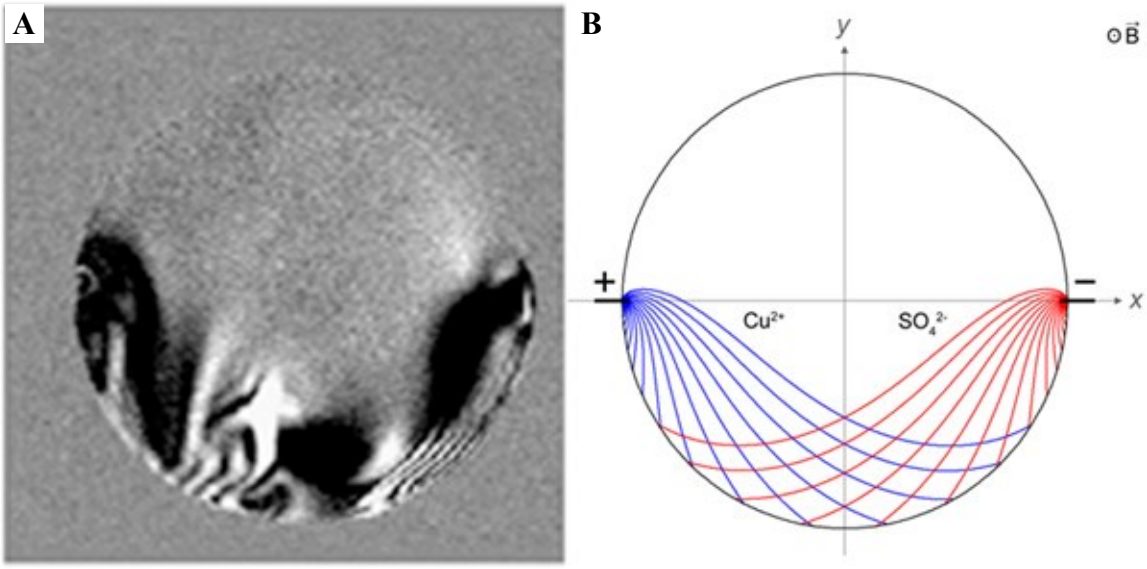

Figure 1.14: LEI of ionic currents in $CuSO_4$ solution
From Truong, Avram, and Song 2008 [42]. LEI of a $CuSO_4$ filled phantom with wires inserted into each end applied to a square wave current pulse generator (see Figure 1.13). **A**. Experimental signal difference image using an LEI pulse sequence with 5 mA current pulses matched with three cycles of oscillating gradients with strength of 9 mT/m and lobe duration of 10 msecs. **B**. Simulated trajectories of a series of Cu^{2+} and SO_4^{2-} ions in solution subjected to the LEI experiment current pulses.

The theoretical simulation in Figure 1.14B only showed ion trajectories and did not describe the relationship between the ions and water displacement. Also, in 2010, Wijesinghe and Roth argued that their simulations used high ion mobility values, which when corrected to standard values led to undetectable displacements and a diffusion pattern that did not match the experimental results [34]. It was suggested that a different

mechanism, magnetohydrodynamically induced flow, could be significantly affecting the MR signal in this problem, therefore warranting further theoretical investigation [34].

2. Modeling LEI contrast

To understand LEI contrast, we theoretically and computationally explored several Lorentz force mechanisms. As an experimental comparator for our models, we used the results of the electrolyte-filled phantom experiments of Truong et al. [42]. These experiments were selected for the initial study of LEI contrast because they were performed in a controlled environment that was relatively easier to model with fewer confounding factors than the *in vivo* experiments [16], and produced two-dimensional images with available signal data that was more readily comparable and, if needed, repeatable. In addition, it was determined that neurons with ionic currents behaved differently than electron current-carrying wires and could not displace mechanically enough to produce a phase shift detectable by LEI [52]. To understand LEI feasibility in the context of ncMRI, it is may be more appropriate to look at the results of the electrolyte phantom rather than those from electron currents through a wire, or currents applied along a peripheral nerve.

2.1. Computational model of an electrolyte phantom

For all the computational models we used to explore LEI, we created a two-dimensional finite difference model of an electrolyte phantom based on the experiments (Figure 1.13). In the LEI experiments, the central MRI slice of a 10 cm diameter spherical phantom was imaged within a 12 cm x 12 cm square viewing domain (MRI slice thickness of 5 mm) [42]. The phantom has two opposing electrodes at the left and

right ends, modeled as point sources which generated an electrical potential distribution within the phantom. The viewing domain outside of the phantom was air, insulated from the electrical field within the phantom, with no magnetic properties.

2.1.1. Model assumptions

To compute electrical potentials and fluid dynamics within our computational model of the phantom we used numerical methods based on a geometrical approximation and an electrode approximation. A geometrical approximation of the central MRI slice of the spherical phantom was made using the central slice of a cubical phantom.

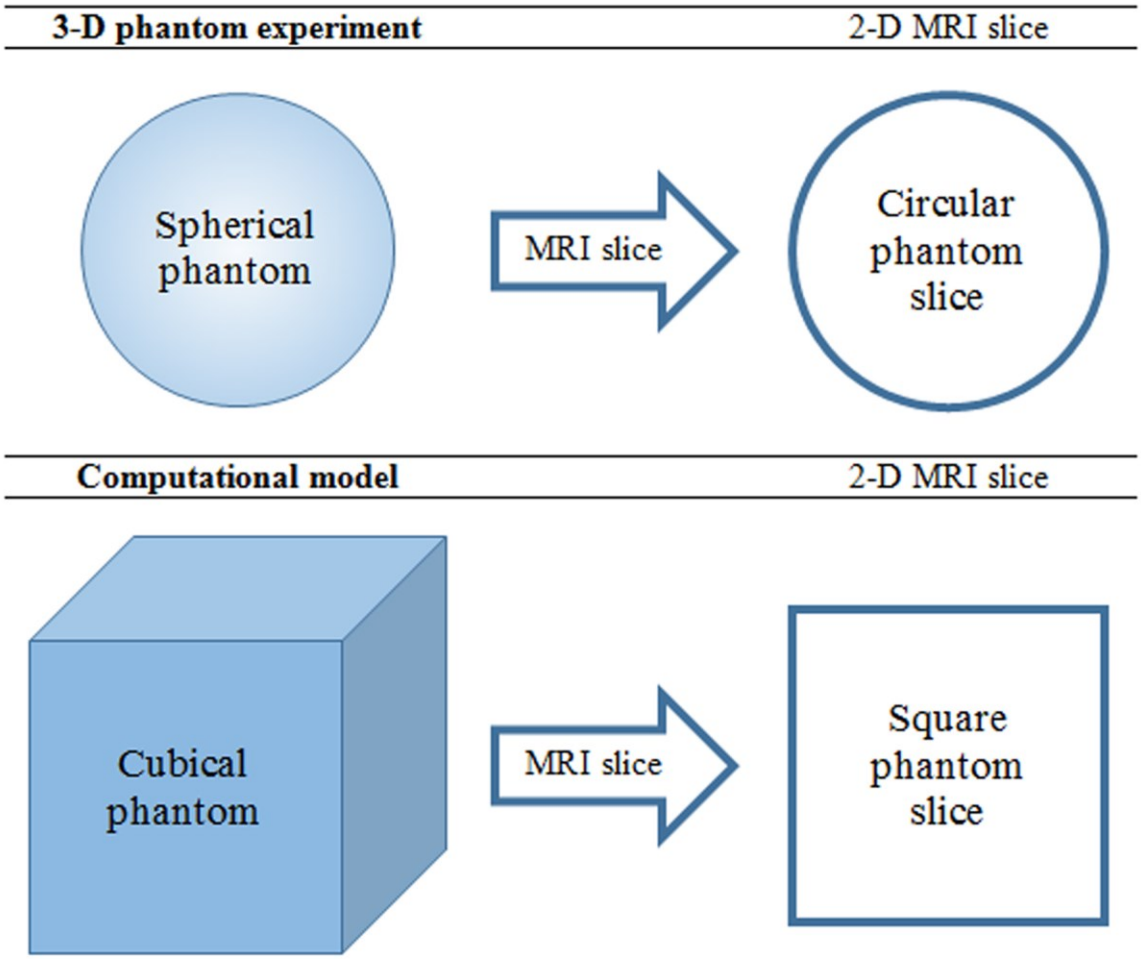

Figure 2.1: Formation of the computational model phantom domain
A 10 cm spherical phantom and its circular central MRI slice were simplified to a 10 cm cubical phantom with a square central slice. Computational model results outside of the central 10 cm circle were cropped before image display to match the experimental results display.

Representing the phantom as a square simplified the solver method in most cases. Compared to a round phantom domain, computing within a square changes the spatial distribution of signal loss, especially near the corners, but the overall scale of signal loss should not be greatly affected by this approximation.

An electrode approximation was also made based on the design of the experimental apparatus electrodes to mimic point sources. Realistically the electrodes

were stripped copper wires 2 mm in diameter that extend 4 mm in length into the phantom, inserted through small holes that were sealed with non-conducting glue. In the computational model however, we designated true point sources at the left and right ends of the phantom and computed electric potentials and the electric field at points within a finite difference grid (see figure below).

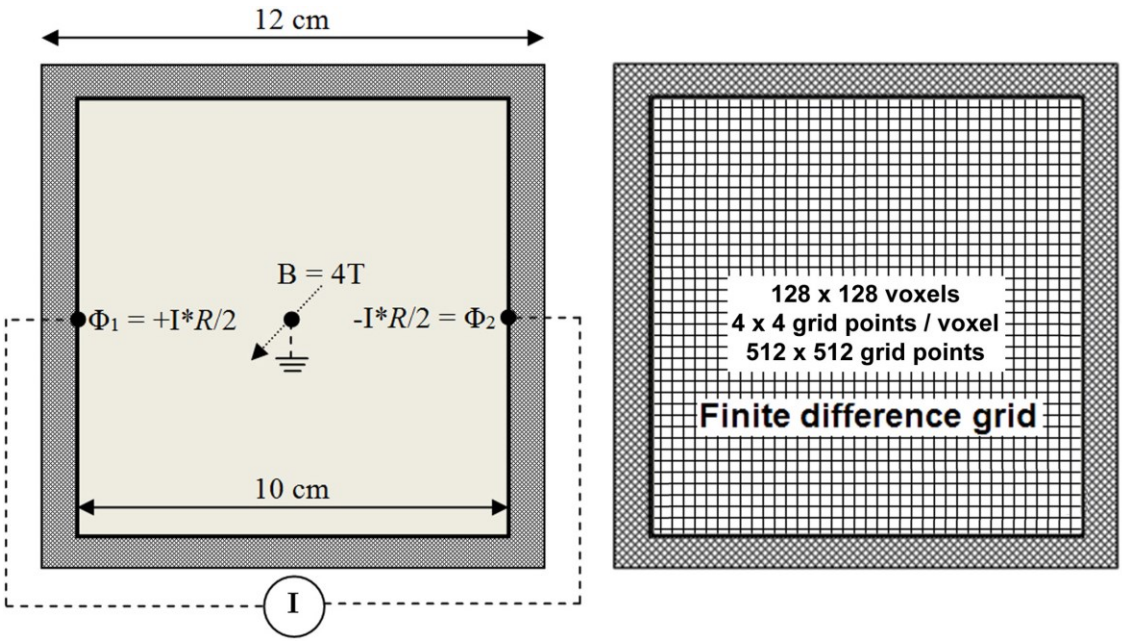

Figure 2.2: Computational model representation of a square electrolyte phantom
Square cross-section of the central slice (5 mm thickness) of a 10 x 10 x 10 cm cubical phantom placed within a 12 x 12 cm field of view of an MRI acquired 2-D image. The phantom domain is a 10 x 10 cm central square (lighter shade) with inter-electrode resistance *R* based on the corresponding experiments (see Figure 1.13). The remainder of the viewing domain (darker shade) is modeled as air with no electrical or magnetic properties. Point source electrode potentials Φ_1 and Φ_2 are computed based on *R* and the applied current I, with a ground of zero potential placed at the center of the phantom. The magnetic field **B** is oriented out of the page with strength of 4 T. Electrical potentials and fluid dynamics variables for the inner 10 x 10 cm phantom domain are computed using a 512 x 512 finite difference grid.

Modeling the electrodes as point sources with no electrode electrolyte interface has an effect on the results that will be discussed after the results are shown in Chapter 4.

2.1.2. Computing the electric field

Based on the applied stimulus current strength (I) and the inter-electrode resistance (R), we compute electric potentials ($\Phi_{1,2}$) of the point sources and a reference ground potential ($\Phi_0 = 0$) is placed at the center point of the phantom domain (see Figure 2.2).

$$\Phi_1 = +I*R/2, \text{ and } \Phi_2 = -I*R/2$$

In this equation Φ_1 is the potential at the anode and Φ_2 is the potential at the cathode for the two electrodes (point sources) used to inject current across the phantom (direction of current flow is oriented left to right for positive current strengths). The three known grid point potentials (Φ_1, Φ_2, and Φ_0) are used as Dirichlet boundary conditions within the phantom numerical solver method.

Assuming a balanced electrolyte with uniform current density (net charge equal to zero) we apply Laplace's equation to solve for the distribution of electric potentials within the phantom slice at finite set of (512 x 512) grid points.

$$\sigma\nabla^2\Phi = 0$$

In constructing our numerical method, we use a connectivity matrix **M** to describe the Laplacian of the vector **Φ** of electric potential for all grid points within the computational model, where **0** denotes the zero vector.

$$\mathbf{M\Phi} = \mathbf{0}$$

We remove the three Dirichlet potentials from **Φ** to compute unknown potentials in the new vector **Φ'**. We compute the contribution of the Dirichlet potential points to the Laplacian of the unknown potential points, and add them to the zero vector to form a new

right hand side vector **B**. We also perform column and row elimination on the connectivity matrix to form the new connectivity matrix **M'** to derive the Poisson equation below.

$$\mathbf{M'\Phi'} = \mathbf{B}$$

This Poisson equation incorporates sources within the phantom and was used to compute electric potentials in **Φ'**, after which the known Dirichlet potentials were added back to reform the full vector **Φ** of electric potentials at every grid point in the computational model. We then calculated the electric field vector **E** at every grid point as the gradient of the scalar electric potential Φ.

$$\mathbf{E} = -\nabla\Phi$$

An alternate method of computing the electric field distribution is to compute the electric potentials from the injected current density in the phantom using the quasi-static approximation of Maxwell's equation describing the distribution of electric potentials Φ in the volume conductor Ω of conductivity σ, resulting from a primary current density J, described by the following Poisson equation.

$$\nabla\cdot(\sigma\nabla\Phi) = \nabla\cdot J \quad \text{in } \Omega$$

A Neumann boundary condition $\langle\sigma\nabla\Phi,n\rangle=0$ is typically paired with this solution describing that the current density directed normal to the boundary surface is zero. The experimental phantom was filled with a 2.8 g/l $CuSO_4$ solution with a homogeneous isotropic conductivity of σ = 140 S/m. Therefore, the current density and electric field within the phantom are proportional and can interchangeably be solved for based on the following equation.

$$\mathbf{J} = \sigma \mathbf{E}$$

In a phantom with anisotropic conductivity, a conductivity tensor must be used to compute the potentials in the Poisson equation. In a phantom with inhomogeneous conductivity that is spatially dependent, the boundary conditions must be modified to solve for the potential distributions separately within each boundary of the regions with differing conductivity, and the current density and electric field will no longer be proportional throughout the phantom.

Solving for electrical potentials or current density within a spherical or circular space will alternative require different boundary conditions (and spherical coordinates) in our numerical solver. It will also preclude our use of the finite difference method due to the error from using square grid spacing with a stepped circular boundary that is compounded over the duration of the LEI protocol and causes an artifact of signal loss uniformly around the boundary of the phantom (not shown). This artifact can likely be prevented using triangular mesh elements and a finite element solver method. However, the Navier-Stokes numerical method we use is based on finite differencing and therefore computing electrical potentials using the square domain and cropping method we outlined is preferred to prevent the boundary artifact.

The electrical potentials computed using our methods within the phantom are shown in the figure below.

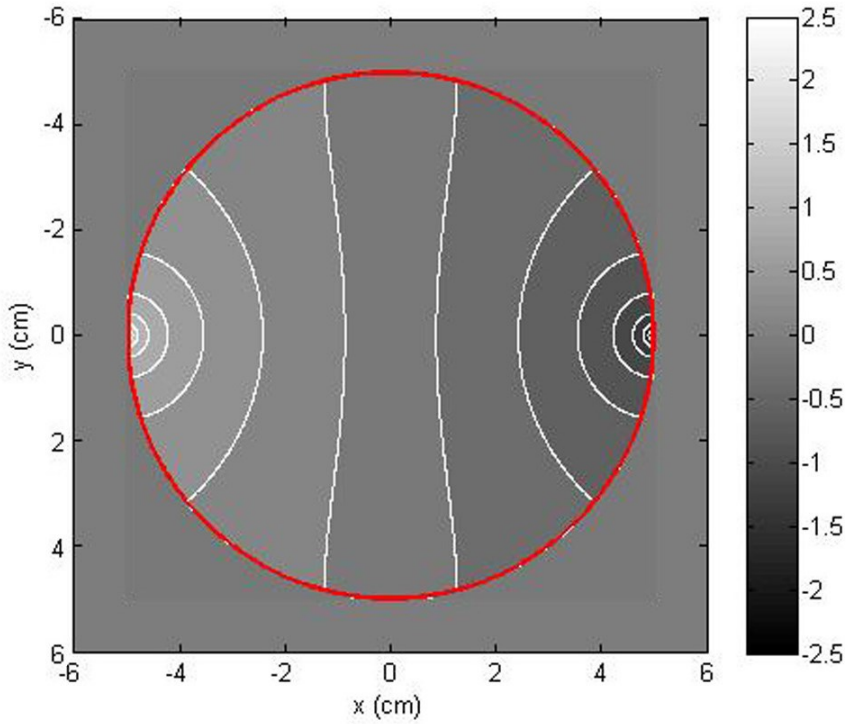

Figure 2.3: Electrical potentials within the computational phantom model for current strength of 5 mA
Contour plot of the electric potential with the current stimulus on, showing a range of potentials from +2.5 V to -2.5 V for an applied current strength of I = 5 mA using the model geometry in Figure 2.2. Electric potential with the current stimulus off was uniformly zero.

The electrical potential distribution within the phantom is subsequently used to compute the electrical field and Lorentz force in our computational models.

2.2. The Lorentz effect in electrolyte solutions

To comprehensively explore potential LEI contrast mechanisms in electrolyte solutions or physiologic tissues with ionic currents, i.e. neuronal tissue, we defined primary ways in which the Lorentz force could generate forces in the electrolyte phantom

with applied current under a magnetic field. First, the Lorentz force acts on charged or polarized particles in the presence of an electromagnetic field and can be defined as follows:

$$\mathbf{F_L} = \mathbf{F_E} + \mathbf{F_B} \tag{2.1}$$

where the Lorentz force, $\mathbf{F_L}$, is the combination of an electric force $\mathbf{F_E}$ and a magnetic force $\mathbf{F_B}$ due to the presence of the electrical and magnetic field, respectively. Secondly, the Lorentz force can generate particle motion based on the nature of the particle being studied. The LEI contrast mechanisms we explored were defined as follows, with regard to potential Lorentz force interactions in an electrolyte solution under an electromagnetic field.

Table 2.1: Potential Lorentz force interactions within the electrolyte phantom

The Lorentz force interacts with:

1. Electrical currents = Hall effect

2. Charged ions in solution = Ion flow

3. Conductive fluids = Electromagnetohydrodynamics

2.2.1. Lorentz effect on electrical currents

Also known as the Hall effect [53-55], the Lorentz force generated by a magnetic field perpendicular to a current stream in a volume conductor will exert a force on the current paths, thereby distorting their shape.

$$\mathbf{F_L} \propto \mathbf{I} \times \mathbf{B} \tag{2.2}$$

The Lorentz force, $\mathbf{F_L}$, is proportional to the strength of current **I** and the magnetic field **B**, acting in the direction of the cross product of those two vectors. Distortion of the volume current distribution in turn creates a potential difference or electric field within the conductor that is perpendicular to both the current streams and the magnetic field. In ordinary conductance experiments, anions and cations move in opposing directions whereas the Hall current comes from a flow of cations and anions in the same direction along the mutually perpendicular axis [53].

Based on Eq 2.2, the pattern of current distortion would be in the up and down direction in our phantom model, and therefore consistent with the orientation of the Lorentz force explaining the observed experimental results [42]. However, the Hall effect is only easily observed in solid materials where the electric charge carriers have relatively high mobility, such as electrons or holes passing through silicon. Since ionic mobilities in electrolyte solutions and related substances are relatively small, the Hall currents are assumed to be negligible [54, 55]. Similar arguments have been made in experiments using NMR to measure non-uniform current density in ionic solutions [38].

2.2.2. Lorentz effect on ions

The Lorentz force generated on each charged ions in an electrolyte solution is defined as follows:

$$\mathbf{F_L} = \mathbf{F_E} + \mathbf{F_B} = q\mathbf{E} + q\left(\mathbf{v} \times \mathbf{B}\right) \tag{2.3}$$

In this equation, $\mathbf{F_E}$ and $\mathbf{F_B}$ are the electric and magnetic forces (in Newtons, N), respectively, q is the electric charge (in Coulombs, C) of the ion, **E** is the electric field (in Volts/meter, V/m), **v** is the ion velocity (in meters/second, m/s), and **B** is the magnetic field (in Tesla, T).

For the ionic currents described by Truong et al. [42] to explain their results, an assumption must be made about the relationship between the fluid motion and ion motion since MRI measures the hydrogen spins of water. Their model shows ion trajectories based on the Lorentz force but does not describe a relationship between the ions and water molecules. Solute-solvent interactions may be described by the solvation shell and coordination numbers for the ions [56]. To determine the maximal signal loss generated by ion flow we overestimated the ion-water interactions by assuming the ion-associated water molecule displacement is equal to that of the ion, without adding mass or reducing the Lorentz force induced acceleration on the ion. Based on the solvation numbers of the simulated Cu^{2+} and SO_4^{2-} ions [57], we used a range of 4-24 water molecules per simulated ion.

2.2.3. Lorentz effect on conductive fluids

Also known as electromagnetohydrodynamics (EMHD), the Lorentz effect on conductive fluids assumes that all particles within a conducting fluid are acted on by a Lorentz body force ($\mathbf{f}^{EM}$, in N/m^3). This force is the result of an electric field crossed with a magnetic field and is in the direction of **E** x **B** with magnitude **J** x **B**, based on the Lorentz force equation [58]:

$$\mathbf{f}^{EM} = \mathbf{J} \times \mathbf{B}, \text{ where } \mathbf{J} = \sigma(\mathbf{E} + \mathbf{v} \times \mathbf{B}) \tag{2.4}$$

In this equation, **J** is the current density (in A/m^2) and σ is the conductivity (in S/m). We explored two methods of computing particle flow from this form of the Lorentz body force: particle drift and EMHD.

2.2.3.1. Particle drift

A simple approach to approximating the direction and magnitude of EMHD flow was introduced by Wijesinghe and Roth in 2010, in the context of electrolyte phantoms under electromagnetic fields [34]. Based on accepted EMHD theory [58-60], this method assumes that all particles are moving in a free space and that the Lorentz force from Eq. 2.4 pushes the particles toward a terminal drift velocity. Using these principles, we computed displacements from a force balance inherent in the equation for the electromagnetic drift velocity ($\mathbf{v}_D$) of charged particles in free space [58, 60].

$$\mathbf{v}_D = \mathbf{E} \times \mathbf{B} / |B|^2 \tag{2.5}$$

In this equation, B is the magnetic field strength. To compute displacement, we first computed the magnetic damping time, T_M [58, 59].

$$T_M = \rho / \sigma B^2 \tag{2.6}$$

In this equation, ρ is the fluid density (10^3 kg/m^3), σ is the fluid conductivity (140 S/m), and B is the magnetic field strength (4 T) based on the phantom experiments [42]. Thus, in all particle drift simulations, $T_M = 0.45$ sec.

Next, the approximation further assumed that drift velocity is achieved by the end of the magnetic damping time [34]. Thus, each particle velocity **v** achieved by the end of a current pulse is based on the ratio between the current pulse period T_P and T_M:

$$\mathbf{v} = \mathbf{v}_D T_P / T_M \tag{2.7}$$

In our simulations, using a forward Euler method, we update each particle's velocity $\mathbf{v} = (v_x, v_y)$ at every time step in two dimensions as follows:

$$\begin{aligned} v_x(t_{k+1}) &= v_x(t_k) + \Delta t \frac{E_y(t_k)}{B_z T_M} \\ v_y(t_{k+1}) &= v_y(t_k) - \Delta t \frac{E_x(t_k)}{B_z T_M} \end{aligned} \tag{2.8}$$

In the particle drift model, using the finite difference method at every grid point within the phantom, we: (1) computed the electric field and drift velocity from Eq. 2.5; (2) then computed the particle velocity using Eq. 2.8; and (3) finally computed the particle displacement and signal loss using the particle tracking method described below in section 2.3.1.1.

2.2.3.2. Electromagnetohydrodynamics

We developed a gold standard computational model for studying EMHD by using the Lorentz force as a body force, $\mathbf{f}^{EM}$ (N/m^3) from Eq. 2.4, within the incompressible Navier-Stokes equations to solve for the velocity field of a conductive fluid under the influence of an electromagnetic field. Unlike the particle drift model, this method

accounts for a pressure gradient (∇p), a convective acceleration ($\mathbf{v} \cdot \nabla\mathbf{v}$), and a viscous force ($\mu\nabla^2\mathbf{v}$), and assumes that the fluid is incompressible ($\nabla \cdot \mathbf{v} = 0$) as follows:

$$\begin{cases} \rho\left(\dfrac{d\mathbf{v}}{dt} + \mathbf{v}\cdot\nabla\mathbf{v}\right) = -\nabla p + \mu\nabla^2\mathbf{v} + \mathbf{f}^{\mathrm{EM}} \\ \nabla\cdot\mathbf{v} = 0 \end{cases} \tag{2.9}$$

In this equation, ρ is the fluid density (10^3 kg/m^3 for water), p is the pressure (in Pascals, Pa), and μ is the dynamic viscosity (10^{-3} Pa $\cdot$ s for water at 20°C). This model assumes that all particles within a conducting fluid are acted upon by a Lorentz body force with dynamics described by the Navier-Stokes equations; that temperature, fluid density, and charge density are constant throughout the phantom domain over the MRI experiment; that there is no magnetization of the fluid; that polarization forces are insignificant compared to the main component of the Lorentz force; and that there is no background flow.

2.3. Computing phase shift and signal loss

In MRI, the pulse sequence is used to initially excite magnetic dipoles, mainly protons of water molecules within the body, and then the subsequent spins are detected to produce an image [61]. The subject is first introduced into a high magnetic field of strength B_0 after which ensembles of protons align themselves with the main field, which can be regarded as magnetization vectors rotating with a frequency proportional to the strength of the local magnetic field, known as the Larmor frequency [61]. Changes in the magnetic field from gradients lead to deviations in the particle magnetization vector's

precession frequency. In turn, a change in frequency results in accumulation of a phase shift for that particle's spin once the main magnetic field is restored and precession frequency returns to that of the baseline Larmour frequency. Ultimately, a sum of incoherent phase shifts for a collection of particles in a particular voxel results in a reduction in the detected signal magnitude for that voxel relative to the signal detected if there were no gradient oscillations or particle displacements.

The Lorentz effects above ultimately give rise to particle displacement. For the spatially incoherent displacement of water, LEI is designed to generate incoherent phase shift among the hydrogen spins, which is detected as a signal loss [40]. In the ion flow models, we assumed a subset of water molecules moving in conjunction with each ion, whereas in the EMHD models we assumed bulk fluid flow where all fluid particles, both ions and water molecules, moved together with constant charge and mass density throughout the experiment.

In a typical LEI protocol (Figure 1.6), oscillating magnetic field gradients are synchronized to the frequency of the applied current such that the incoherent water displacement caused by the electrical activity is maximized during the positive lobes and minimized during the negative lobes, thereby enhancing the phase shift accumulation of each particle spin, p, over the total oscillating gradient period. To compute the relative LEI signal change from Lorentz effect induced particle displacement, we must determine: (1) the phase shift accumulated per particle based on displacement along the oscillating gradients; (2) the signal contribution per particle based on the phase shift accumulated at detection; (3) the total voxel signal from all particle signal contributions in each MRI

voxel; and lastly (4) the relative signal per voxel based on the signal in a reference case with no applied current (I = 0).

2.3.1. Phase shift accumulation from displacement

In order to compute each particle's spin phase shift at detection, we must take into account particle displacements along the oscillating magnetic gradients and determine the resulting change in the precession frequency of the particle's spin. Using two different interpretations of particle displacement we developed a particle tracking method based on the Lagrangian interpretation of particle motion to compute displacement and phase shift, while a Reynold transport method was developed based on the Eulerian interpretation of particle motion to directly compute phase shift.

2.3.1.1. Particle tracking method

From a Lagrangian interpretation of the fluid particle displacement we represent all water molecule hydrogen spins in the model using a finite set of tracer particles, p, superimposed over the fluid dynamics finite difference grid and compute the time-progression of travel for each p as follows.

$$\mathbf{x}(t) = \int_0^t \mathbf{v} dt + \mathbf{x}_o \tag{2.10}$$

$\mathbf{x}_o$ denotes the initial position of each p at $t = 0$ (initially uniformly spaced) and v is the particle velocity, interpolated from the fluid dynamics grid based on the particle's position assuming **v** changes linearly with **x** within each grid element. The accuracy of

this method should increase as the FD and tracer grids are refined. We will initially place at least one water molecule (n = 0) at the center of each finite difference grid element and increase that number by 4^n (*i.e.* 1x1, 2x2, 4x4, 8x8, 16x16, 32x32, 64x64, 128x128, etc.). We determine an optimal tracer grid resolution when the overall mean fluid displacement computed at the end of the first set of gradients changes <10% with the next increase in *n*.

Using a small Δt, a modified Euler method (2nd order accurate) is used to update the position of p at time $t_k = k\Delta t$ by assuming that particle velocity changes linearly with t during each time period Δt.

In MRI, after excitation, applying magnetic gradient fields will cause the magnetization vectors in different regions of the slice to precess with a spectrum of frequencies determined by their spatial positions along the gradients [62, 63]. A time varying gradient **G**(t) applied after excitation causes transverse magnetization vectors to dephase so that the total phase shift accumulation of each p at time t $\phi(t)$ is defined by the time integral of its spin frequency ω [62]:

$$\phi(t) = \int_0^t \omega(\tau)\, d\tau \tag{2.11}$$

In this equation, ω is a function of the magnetic field of strength B, experienced by p based on the Larmour equation [45, 62]:

$$\omega(t) = \gamma B(t) \tag{2.12}$$

In this equation, γ is the gyromagnetic ratio ($2\pi*42.58*10^6$ rad/s/T for hydrogen [46]). We compute the particle spin phase shift and the resulting signal loss based on fluid particle displacements along the oscillating gradients of strength **G** = (G_x, G_y).

Without gradients, the magnetic field experienced by p is constant and equal to that of the main field of the scanner, B_0, so the central frequency ω_0 determining phase shift is as follows:

$$\omega_0 = \gamma B_0 \tag{2.13}$$

Applying linear gradients creates an inhomogeneous B-field that will change ω from ω_0 by ω_R based on the location $\mathbf{x} = (x, y)$ for each p [62]:

$$\omega_R = \gamma \mathbf{G}(t) \cdot \mathbf{x}(t) \tag{2.14}$$

$$\omega(t) = \omega_0 + \omega_R(t) = \gamma B_0 + \gamma \mathbf{G}(t) \cdot \mathbf{x}(t) \tag{2.15}$$

Substituting the expression above into Eq. 2.11, the equation to compute ϕ for each p under a set of magnetic gradients becomes an integral of the gradient dot product with the particle displacement [48, 62]:

$$\phi(t) = \gamma \int_0^t B_0 + \mathbf{G}(\tau) \cdot \mathbf{x}(\tau) d\tau \tag{2.16}$$

To compute the relative phase shift, each $\phi(t)$ can be represented as the sum of a relative phase shift $\phi_R(t)$ (time dependent due to gradients) and a reference phase shift ϕ_0 (constant, based on ω_0) [64]:

$$\phi(t) = \phi_0 + \phi_R(t) \tag{2.17}$$

$$\phi_0(t) = \int_0^t \omega_0 dt = \gamma \int_0^t B_0 dt = \gamma B_0 t \tag{2.18}$$

$$\phi_R(t) = \int_0^t \omega_R(\tau) d\tau = \gamma \int_0^t \mathbf{G}(\tau) \cdot \mathbf{x}(\tau) d\tau \tag{2.19}$$

We evaluate the integral in Eq. 2.19 using a modified Euler method to incrementally update ϕ_R for each p accumulated over Δt using $\mathbf{v}$ from the Navier-Stokes solutions at every t_k (from $k = 0{:}n$) as follows:

$$\phi_R(t_{k+1}) = \phi_R(t_k) + \Delta t \gamma \mathbf{G} \cdot \left(\mathbf{x}(t_{k+1}) + \mathbf{x}(t_k)\right)/2 \tag{2.20}$$

This is the particle tracking method used to incrementally compute ϕ_R based on updates in displacement, $\mathbf{x}(t_k+1)$. To derive an expression for ϕ_R based on updates in velocity, $\mathbf{v}(t_k+1)$, we use the equations of motion and velocities from the Navier Stokes grid. For each p, its position is based on its velocity vector $\mathbf{v} = (v_x, v_y)$ over a known period of time t, where $\mathbf{x}_o$ denotes its initial position at time $t = 0$.

$$\mathbf{x}(t) = \mathbf{v}t + \mathbf{x}_o \tag{2.21}$$

Substituting Eq. 2.21 into Eq. 2.19, we have the following expression for ϕ_R computation that includes particle velocity and initial position [64].

$$\phi_R(t) = \int_0^t \omega_R(\tau)\, d\tau = \gamma \int_0^t \mathbf{G}(\tau) \cdot \mathbf{v}(\tau)\tau + \mathbf{x}_0 d\tau \tag{2.22}$$

To compute the incremental position vector values for p at each discrete time step t_k (for $k = 0{:}n$) of length Δt, we use sufficiently small Δt to assume that incremental velocity has a linear dependence on time and compute the incremental position vector components for p as follows.

$$\mathbf{x}(t_{k+1}) = \Delta t\left(\mathbf{v}(t_{k+1}) + \mathbf{v}(t_k)\right)/2 + \mathbf{x}(t_k) \tag{2.23}$$

Using Eq. 2.23, the incremental computation of ϕ_R using the particle tracking method with velocity updates in the form of Eq 2.21 is below. This form allows us to

update ϕ_R directly using the particle's current position and velocity update from the Navier Stokes solution.

$$\phi_R(t_{k+1}) = \phi_R(t_k) + \gamma \mathbf{G} \cdot \left[\frac{\mathbf{v}(t_{k+1}) + \mathbf{v}(t_k)}{2} \frac{\Delta t^2}{2} + \mathbf{x}(t_k)\Delta t \right] \tag{2.24}$$

2.3.1.2. Reynolds transport method

Reynolds transport theorem is used to approximate ϕ_R directly from fluid velocity updates at a specified grid position without having to track particles by using an Eulerian interpretation of fluid particle displacement along gradients of strength $\mathbf{G} = (G_x, G_y)$. For a p detected on MRI at position $\mathbf{x}$, ω and ϕ_R are defined in Eq. 2.14 and 2.18. Computing the time derivative of Eq. 2.18 we have another definition for ω as the change in ϕ_R over time.

$$\frac{d\phi_R}{dt} = \omega_R(t) \tag{2.25}$$

Using Reynolds transport theorem, for all p passing through a region $A(t)$ bounded by a set of grid points with fixed position $\mathbf{x}_0 = (x_0, y_0)$, the following is true:

$$\frac{d}{dt} \iint_{A(t)} \phi_R dxdy = \iint_{A(t)} \frac{d\phi_R}{dt} + \nabla \phi_R \cdot \mathbf{v} + \phi_R \nabla \cdot \mathbf{v} dxdy \tag{2.26}$$

Accounting for incompressible flow $(\nabla \cdot \mathbf{v} = 0)$ in Eq. 2.25, we have the following expression.

$$\frac{d}{dt} \iint_{A(t)} \phi_R dxdy = \iint_{A(t)} \omega_R + \nabla \phi_R \cdot \mathbf{v} dxdy \tag{2.27}$$

Hence, for ϕ_R at each grid point, the following expression is true.

$$\frac{d\phi_R}{dt} = \omega_R(t) + \nabla\phi_R(t)\cdot\mathbf{v}(t) \tag{2.28}$$

We set the coordinates and velocities for these grid points to be the same as those for the Navier Stokes finite difference grid. Using small Δt and the forward Euler method on Eq. 2.28, ϕ_R is updated at each time step as follows.

$$\phi_R(t_{k+1}) = \phi_R(t_k) + \Delta t\gamma\mathbf{G}\cdot\mathbf{x}_0 + \nabla\phi_R(t_k)\cdot\mathbf{v}(t_{k+1})\Delta t \tag{2.29}$$

Comparing this Eulerian form in Eq. 2.29 to the Lagrangian form in Eq. 2.24, we note that the $\mathbf{x}_0$ here are independent of time based on fixed grid points, whereas in the Lagrangian form, $\mathbf{x}(t_k)$ vary over time as they track each p. In both forms the values of $\mathbf{v}$ change over time based on updates from the fluid dynamics equations. In the Eulerian form, the positions at which $\mathbf{v}$ updates are fixed with values from the finite difference grid, while in the Lagrangian form the positions at which $\mathbf{v}$ are updated vary with p and have values interpolated from the finite difference grid based on their location. To further compare the particle tracking and Reynolds transport methods analytically, we substitute a new time-dependent distance parameter $\bar{\mathbf{x}}$ into Eq. 2.20 as follows.

$$\bar{\mathbf{x}}(t_{k+1}) = \left(\mathbf{x}(t_{k+1}) + \mathbf{x}(t_k)\right)/2 - \mathbf{x}_0 \tag{2.30}$$

$$\phi_R(t_{k+1}) = \phi_R(t_k) + \Delta t\gamma\mathbf{G}\cdot\mathbf{x}_0 + \Delta t\gamma\mathbf{G}\cdot\bar{\mathbf{x}}(t_{k+1}) \tag{2.31}$$

The time-dependent position $\bar{\mathbf{x}}$ in the particle tracking method Eq. 2.31 is accounted for in the Reynolds transport method Eq. 2.29 by the product of the gradient of ϕ_R and a time-dependent distance parameter, $\mathbf{v}(t_{k+1})\,\Delta t$.

The final Reynolds transport method used to update ϕ_R from Eq. 2.29 in two dimensions is as follows.

$$\begin{aligned}\phi_R(t_{k+1}) &= \phi_R(t_k) + \Delta t\gamma\left(G_x x_0 + G_y y_0\right) \\ &+ \Delta t\left(\frac{\partial \phi_R(t_k)}{\partial x} v_x(t_{k+1}) + \frac{\partial \phi_R(t_k)}{\partial y} v_y(t_{k+1})\right)\end{aligned} \tag{2.32}$$

2.3.2. Signal contribution from phase shift

In MRI, the signal contribution, s for each p detected at $t = n\Delta t$ is based on the relative phase shift (ϕ_R) of that particle's spin (p) and a time dependent weighting m, as follows.

$$s(t) = m(t)e^{-i\phi(t)} = m(t)e^{-i\phi_0(t)}e^{-i\phi_R(t)} \tag{2.33}$$

In this equation, $m(t)$ is the relative signal coefficient for p, dependent upon global signal losses over time. We compute the total signal strength S for each voxel at detection time t as the integral of the signal contribution from Eq. 2.33 for all p within the x-y bounds of the voxel.

$$S(t) = \int_x \int_y m(t)e^{-i\phi_0(t)}e^{-i\phi_R(t)}dxdy \tag{2.34}$$

In evaluating S we assume that signal losses over time outside of the Lorentz effect for each p are the same in the case with or without gradients, making $m(t)$ the same for every p detected. We also discretize the time integral in Eq. 2.34 to evaluate ϕ_R for each p and compute the spatial integral in x and y over the voxel by summing every s

detected in the voxel, where N is the total particles per voxel, n is the total simulation time steps between excitation and detection, and t_k is the current time step.

$$S(t) = m(t)e^{-i\gamma B_0 t}\sum_{\mathrm{p}=1}^{\mathrm{N}}\exp\left[-i\sum_{k=0}^{n}\phi_R\left(t_k\right)\right] \tag{2.35}$$

2.3.3. Relative signal strength

In the absence of gradients, we assume a homogeneous static main field B_0 making ω_0 constant for the reference voxel signal S_0, which is computed as follows.

$$S_0(t) = \int_x\int_y m(t)e^{-i\phi_0(t)}dxdy \tag{2.36}$$

$$S_0(t) = \mathrm{N}m(t)e^{-i\gamma B_0 t} \tag{2.37}$$

With such a large main B_0-field, we assume that the distribution of N particles per voxel is not affected by the presence of gradients and display each MRI image voxel's relative signal S_R as the percent change in the magnitude of S relative to S_0.

$$S_R = \left\|\frac{S(t)-S_0}{S_0}\right\| = \frac{1}{\mathrm{N}}\left\|\sum_{\mathrm{p}=1}^{\mathrm{N}}\exp\left[-i\sum_{k=0}^{n}\phi_R\left(t_k\right)\right]\right\| - 1 \tag{2.38}$$

In this equation, n is the number of time steps of length $\Delta t = t/n$ until detection at time t.

3. EMHD and particle drift

To better understand LEI contrast, we performed preliminary studies of the particle drift and EMHD images and fluid dynamics described in the previous chapter. Both models are a representation of the Lorentz effect on a conducting fluid, but in the particle drift model particles are assumed to move in a free space and fluid dynamics forces are ignored, whereas in EMHD a full account of the fluid dynamics are incorporated. The initial results will be used to compare the accuracy of particle drift in estimating the particle velocity, displacement, and LEI signal strength compared to the EMHD model. Also, the EMHD model will be explored in detail to determine the relative contribution of each component of the fluid dynamics equation (ignored in the particle drift model) on the overall flow fields and understand the EMHD effect.

3.1. Inter-model comparison methods

Implementation of the solver methods and data analysis was performed in MATLAB v7.11. The implemented computational phantom model was based on the central MRI slice of a 10x10x10 cm cubical phantom within a 12x12 cm square viewing domain with slice thickness of 5 mm as shown in Figure 2.2 and explained in section 2.1. For all simulations, an MRI image matrix of 128x128 voxels was used.

Representing the phantom slice as a square instead of a circle simplified the use of a finite difference method for computing the fluid dynamics. Based on initial simulations, compared to a circle, the square domain changed the velocity profiles primarily near the

corners, which – when clipped – resulted in less than 1% mean difference in velocity and displacement magnitudes in the phantom domain. Thus, for our simulations, a square phantom domain was used while ignoring results outside of the central 10 cm diameter circle to allow for a better comparison with the experimental results. Figure 3.1 below is a representation of the modified circular phantom, a contour plot of the electrical potential distribution in the phantom, and the LEI pulse sequence used for all EMHD model simulations.

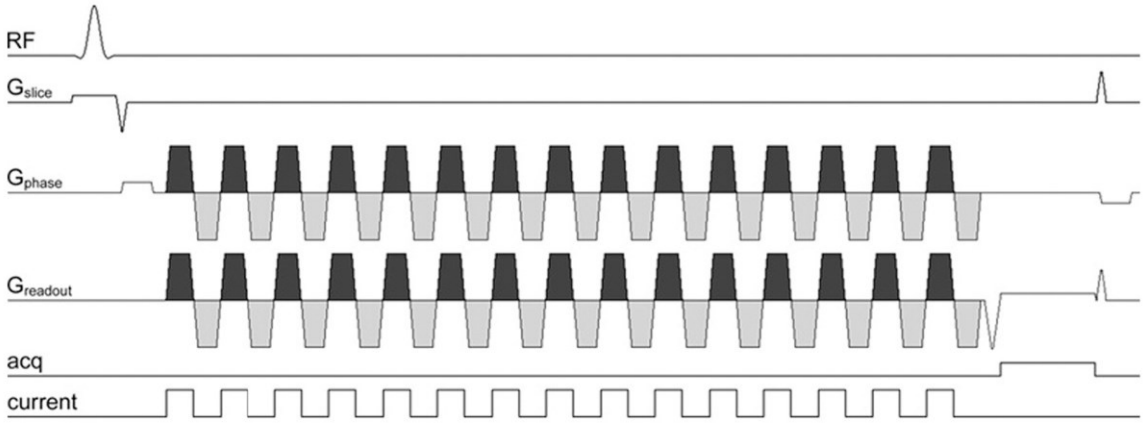

Figure 3.1: LEI protocol used in the computational models
Pulse sequence diagram adapted from the corresponding LEI experiment [42]. Applied current pulses were synchronized to the positive lobe of fifteen gradient oscillations. Computational model gradient lobes were rectangular rather than trapezoidal. Gradient strengths of G_x (G_{phase}) = G_y ($G_{readout}$) = 36 mT/m were used.

The modeled phantom domain (Figure 3.1A) has two electrodes at the left and right poles with opposite polarities, which are modeled as point sources using Dirichlet boundary conditions. A no-flux boundary condition is imposed at all other points along the phantom domain boundary. The phantom, filled with a 2.8 g/l $CuSO_4$ solution, has a homogeneous conductivity of σ = 140 S/m, an inter-electrode resistance of $R = 10^3\ \Omega$,

and a magnetic permeability of μ_m = -9*10^{-6} H/m. Based on the applied stimulus current (I = 5 mA), the inter-electrode resistance is used to compute the electric potentials ($\Phi_{1,2}$ = ± I*R/2) of the point sources, and a ground (Φ = 0) is placed as a reference potential at the center point of the phantom domain (see Figure 3.1B for a distribution of electrical potentials for a 5 mA stimulus current). The viewing domain outside of the phantom is considered to be air, insulated from the electrical field within the phantom, with no magnetic properties, and given a reference signal strength of S = 0.

An LEI protocol from the phantom experiments (Figure 3.1C) was used for our model simulations, with n = 15 cycles of oscillating gradients with lobe durations of T = 2 msec and amplitudes of **G** = 36 mT/m, applied with the positive gradient lobes synchronized to the current-on periods. Model gradient lobes during the simulations are rectangular rather than trapezoidal for simplification.

Implementation of the EMHD solver method to compute fluid velocity is adapted from MATLAB code for solving the incompressible Navier-Stokes equations, developed by Seibold and published by Strang [65]. This method uses finite differencing on a staggered grid with implicit diffusion and a Chorin projection method for updating pressure, where velocity is serially updated for each term at every time step. The solver method is modified from use of the non-dimensional Navier-Stokes equations to the dimensional form shown in Eq. 2.8 using SI units with density ρ and viscosity μ instead of a non-dimensional Reynolds number. In addition, the Lorentz force, $\mathbf{f}^{\mathbf{EM}}$ from Eq. 2.4, is added as an electromotive body force in the velocity update at each time step, thereby

completing the EMHD force balance. Rewriting Eq. 2.8, the equation used in our computational solver method to update fluid velocity at each time step is:

$$\frac{\Delta \mathbf{v}}{\Delta t} = \frac{1}{\rho}\mathbf{f}^{\mathrm{EM}} - \mathbf{v}\cdot\nabla\mathbf{v} + \frac{\mu}{\rho}\nabla^2\mathbf{v} - \frac{1}{\rho}\nabla p \tag{3.1}$$

Our solver method described above computes velocity changes over each time step using a series of updates from each term on the right hand side of Eq. 2.38. The time step used for all simulations is Δt = 0.002 sec, which is 1000x smaller than the current pulse period and produced results that were convergent and relatively unchanged for a 10x smaller time step (< 1% mean relative change in velocity and displacement for Δt = 0.0002 sec).

3.2. Study of EMHD flow results

To understand EMHD flow, we first studied electromagnetic drift theory to approximate the direction of Lorentz force induced flow for the circular phantom based on the drift velocity in Eq. 2.5.

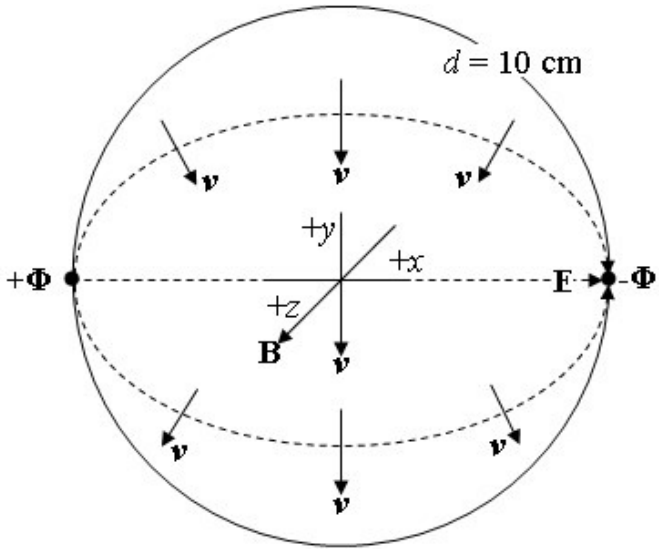

Figure 3.2: Lorentz force induced flow velocity from electromagnetic drift
Coordinate axes directions are indicated by +x, +y, and +z. The magnetic field, **B**, is in the +z direction. The electric field, **E**, is depicted using dotted lines and trends in the +x direction. The direction of Lorentz force follows the cross product of **E** x **B**, which is the same as the electromagnetic drift flow velocity, ***v***, which trends in the –y direction.

In Figure 3.2 above, the Lorentz force induced flow trends downward and is relatively perpendicular to the phantom boundaries. In the particle drift model, which lacks adequate boundary conditions or other forces, it is difficult to predict the actual particles' movement and where the particles will generate signal loss. To explore this boundary effect and the magnitude of velocity, displacement, and signal loss from the above depicted Lorentz induced flow, we use the particle drift model with Reynolds transport method based on the phantom and LEI protocol parameters depicted in Figure 3.1 and report the results in Table 3.1 below.

Table 3.1: Particle drift model mean and maximal velocity, displacement, and relative signal change for 5 mA current pulses

	Mean	Max
Velocity at the end of the final current pulse	0.30 m/s	20 m/s
Displacement at the end of the final negative gradient lobe	0.92 cm	62 cm
Relative signal change at detection	-23%	-100%

Compared to the Reynolds transport method results above, using the particle tracking method in the particle drift model achieves similar flow velocity values from the fluid dynamics finite difference grid (mean of 0.12 m/s, maximum of 20 m/s) but with mean and maximal particle displacements approximately 10x lower (mean of 0.024 cm, maximum of 7.4 cm). The mean and maximal relative signal changes with the particle tracking method (mean of -18%, maximum of -96%) are similar to those of the Reynolds transport method (Table 3.1).

For comparison, an estimate of the particle drift velocity was previously made for this experiment by approximating a uniform 50 V/m electric field perpendicular to a 4 T magnetic field, which produced a drift velocity of 12 m/s [34]. Using Eq. 2.5 and Eq. 2.7, the particle velocity after one pulse of the 50 V/m uniform field can be estimated at 0.054 m/s. After 15 pulses the estimated final particle velocity is 0.81 m/s.

In the particle drift model simulations using Reynolds transport method, the electric field was non-uniform with magnitude at grid points within the phantom having a mean of 17.66 V/m and maximum of 1197 V/m, generating a mean final velocity of 0.30

m/s, and maximal final velocity of 20 m/s (Table 3.1) among all voxels within the phantom.

These represent a range of velocities approximately one order of magnitude above and below the electromagnetic drift estimate from the uniform 50 V/m field. Final displacement in the phantom from the particle drift model has a mean of 0.92 cm and a maximum of 62 cm, while the signal change achieved has a mean of 23% loss and a maximum of 100% loss among all voxels within the phantom. Thus we expect the electromagnetic drift estimates using a uniform field would be associated with a displacement and signal loss within these ranges.

To determine the effect of the oscillating gradients on velocity and displacement, we explored the dynamics of mean flow velocity and displacement over the full simulation time using the particle drift model with Reynolds transport method and four particles per voxel.

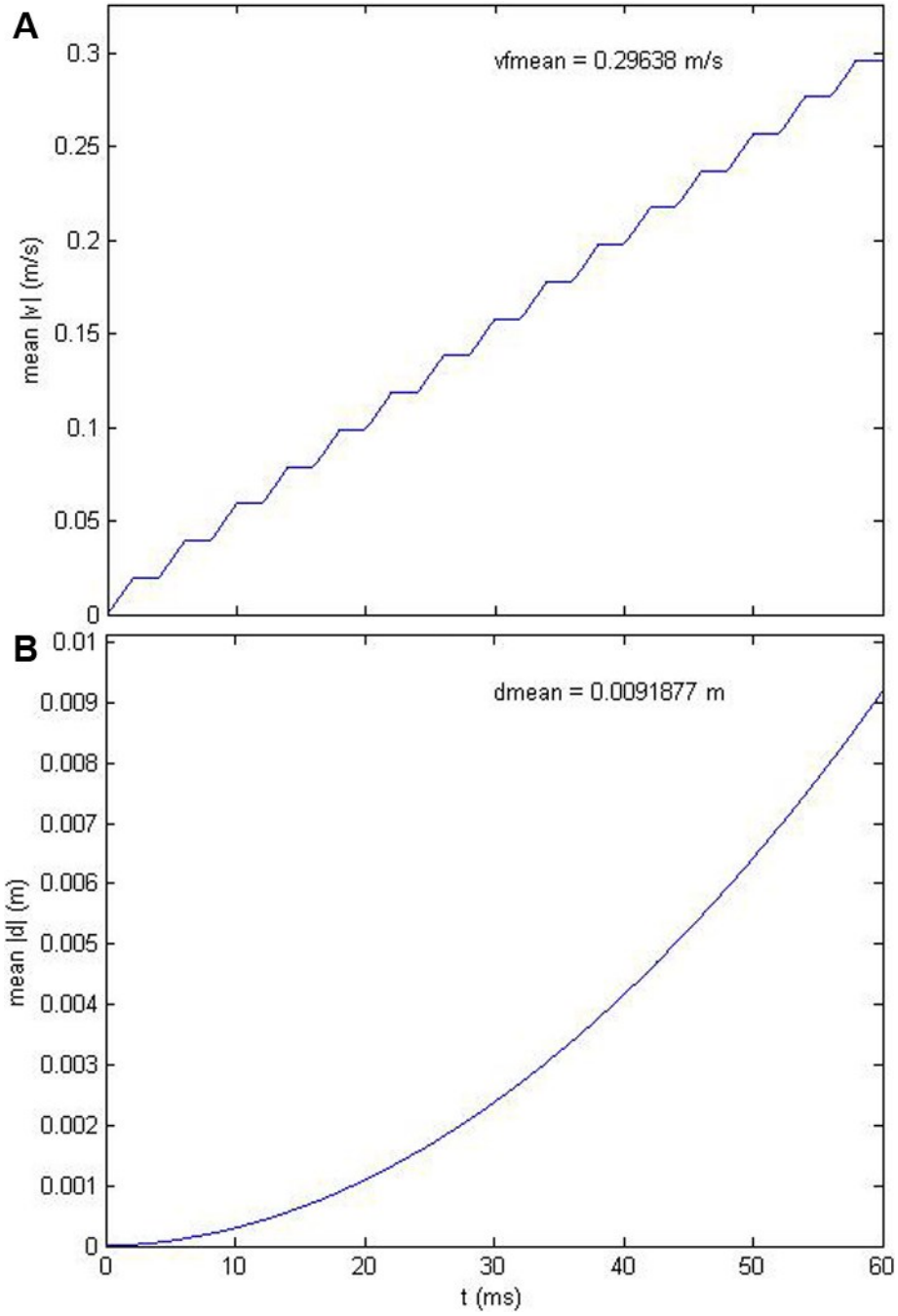

Figure 3.3: Particle drift model mean velocity and displacement over time
Mean velocity and displacement computed among voxels within the simulated phantom for the LEI protocol in Figure 3.1 using the particle drift model shows: **A**. mean velocity linearly increasing over the current-on periods, while remaining flat during current-off periods and **B**. mean displacement increasing quadratically over the entire simulation.

In the particle drift model, the mean flow velocity within the phantom linearly increases during the current-on periods and remains relatively flat during current-off periods (Figure 3.3A) consistent with electromagnetic drift theory [58], while the mean particle displacement within the phantom increases quadratically over the course of the entire simulation time (Figure 3.3B). From Table 3.1, there ultimately is a detectable signal loss in the phantom (threshold for detectable signal loss for all simulations is set at relative signal change < -1).

We also explored the dynamics of mean flow velocity and displacement over the full simulation time for the EMHD model with Reynolds transport method and four particles per voxel and will compare them to the results of the particle drift model.

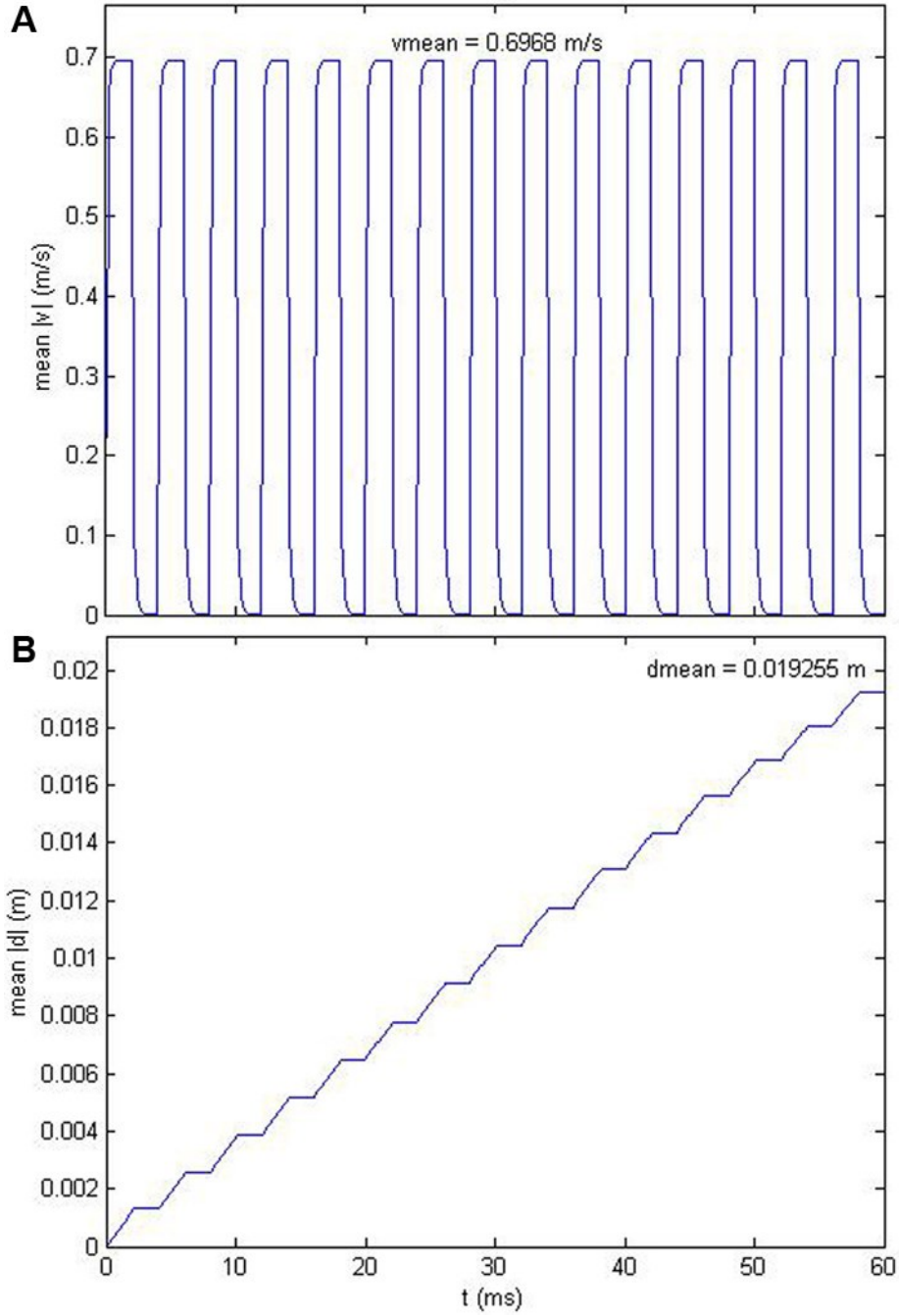

Figure 3.4: EMHD model mean velocity and displacement over time
Mean velocity and displacement computed among voxels within the simulated phantom for the LEI protocol in Figure 3.1 using the EMHD model shows: **A**. mean velocity rapidly increasing to a steady state value over the current-on periods then rapidly decreasing back to zero during current-off periods and **B**. mean displacement increasing linearly over the current on periods and remaining flat during the current off periods.

In the EMHD model, the mean flow velocity within the phantom increases rapidly toward a steady state value during the current-on periods and remains relatively flat, then rapidly decreases to zero during current-off periods (Figure 3.3A). The mean particle displacement within the phantom increases linearly during the current-on periods and then remains flat during current-off periods (Figure 3.3B). In the next chapter we will explore how these dynamics contribute to relative signal changes in the EMHD model.

To better understand the full distribution of velocity, displacement, and signal change within the phantom beyond the mean and maximum values, we evaluate the simulation images. In this chapter we will assess the results of the particle drift model with Reynolds transport method.

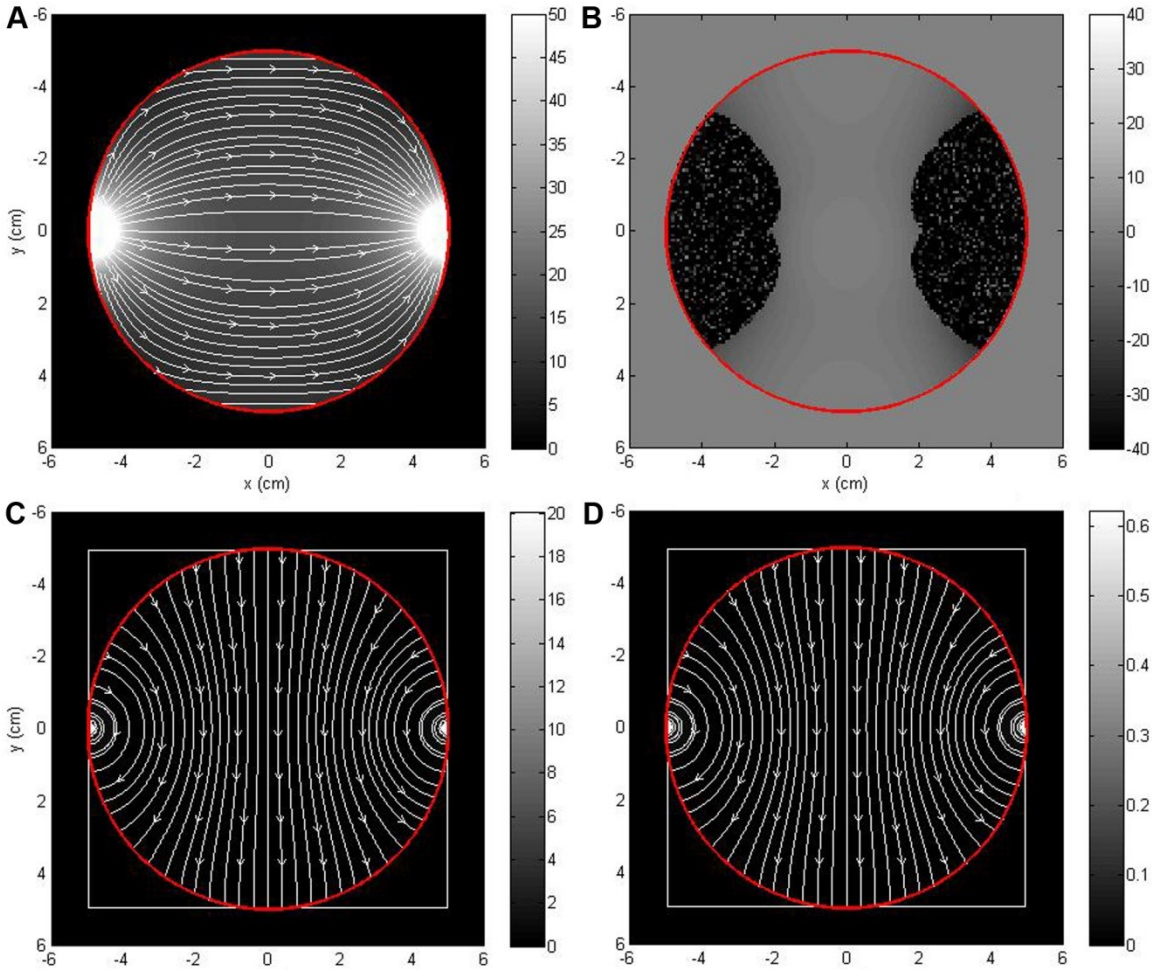

Figure 3.5: Particle drift model maps of the electric field, relative signal change, velocity, and displacement for a 5 mA current pulse
A. Contour plot of the electric field magnitude (V/m) with streamlines showing a left to right direction. Mean and maximal electric field magnitude is reported in Table 3.1. **B**. Relative signal change (%) detected in the particle drift model simulation, showing areas of signal loss expanding out from the electrode locations. **C**. Contour plot of the velocity magnitude (m/s) with streamlines and arrows indicating flow directions trending downward. Mean and maximal velocity magnitude is reported in Table 3.1. **D**. Contour plot of particle displacement (m) with streamlines and arrows trending downward. Mean and maximal displacement is reported in Table 3.1.

We see a symmetric result for the electric field (Figure 3.5 A), velocity map (Figure 3.5 C), and displacement map (Figure 3.5 D). Notably, we also observe a symmetric relative signal change from the particle drift simulations (Figure 3.5 B), which

has a similar mean and maximal order of magnitude (Table 3.1), but does not match the distribution of the experimental results [42].

For an explanation, we compare these result images with those of the EMHD model shown next, and assess the relative effect of each component of the EMHD model in Eq. 2.39 on flow compared to the particle drift model approximation of flow in Eq. 2.8 which ignores these other effects. Using the phantom and current stimulus parameters depicted in Figure 3.1, we compute the phantom velocity field, and mean and maximal velocity magnitude after each update step (order depicted in Table 3.2 below) for the first simulation time step using the Reynolds transport method and Δt = 0.002 msec.

Table 3.2: Fluid velocity updates for each term in the EMHD model
Order of computing velocity updates from each EMHD model term in Eq. 2.39 and the resulting mean and maximal velocity in the phantom after one time step (0.002 msec)

Order updated at each Δt	Term used to update velocity	Definition of EMHD component contributing to flow velocity	Mean and max velocity magnitude in the phantom after each update (m/s)
1	$+\frac{1}{\rho}\mathbf{f}^{\mathrm{EM}}$	Lorentz force	mean: 0.39 max: 20
2	$-\mathbf{v}\cdot\nabla\mathbf{v}$	Convective acceleration	mean: 0.41 max: 150
3	$+\frac{\mu}{\rho}\nabla^2\mathbf{v}$	Viscous force	mean: 0.21 max: 0.31
4	$-\frac{1}{\rho}\nabla p$	Pressure gradient	mean: 0.052 max: 0.37

Compared to the results of the particle drift model simulations, we study the change in the distribution of velocity, displacement, and pressure in the EMHD model phantom after each of these term updates for one time step (t = 0.002 msec), shown in Figure 3.6 below.

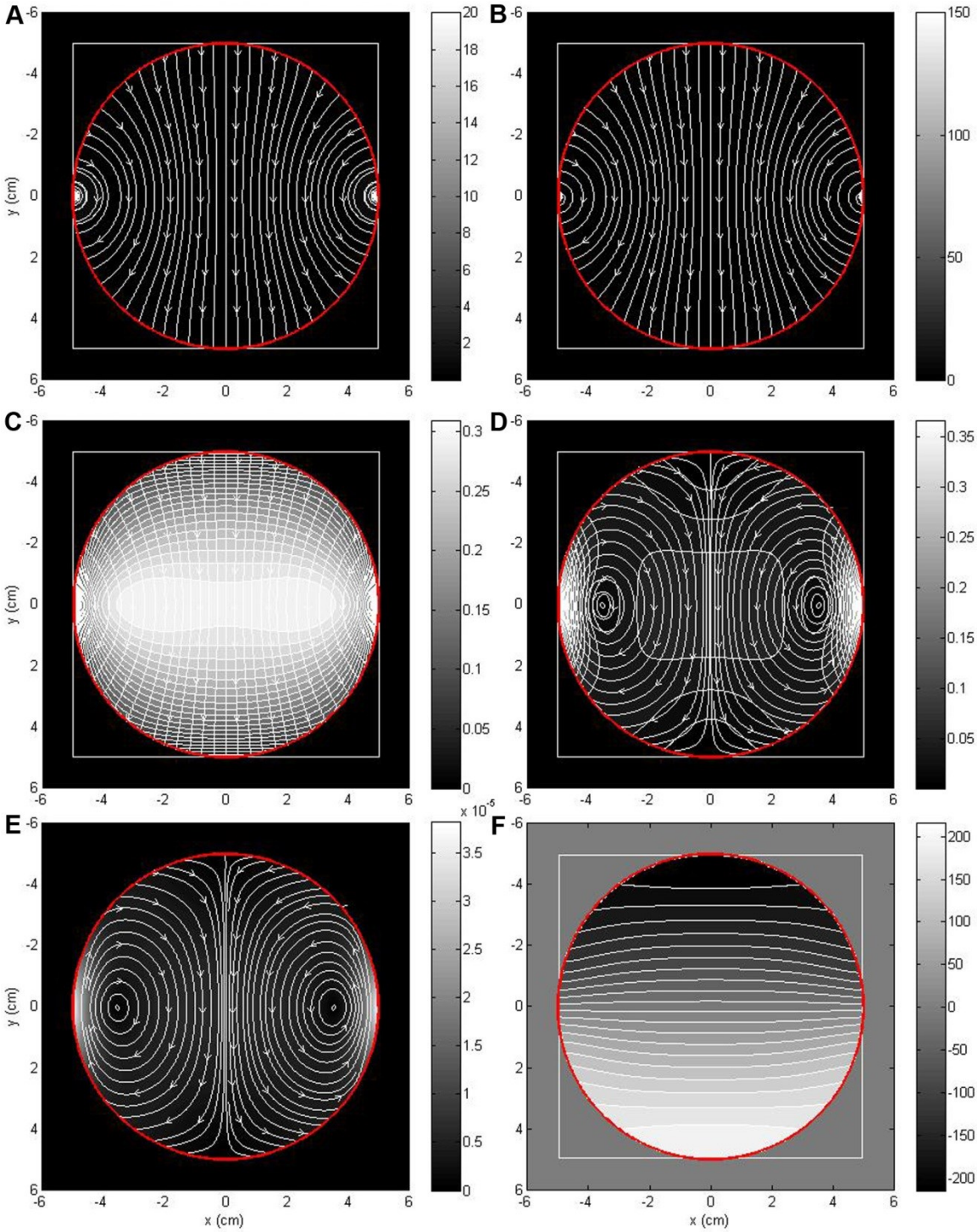

Figure 3.6: Direction and distribution of flow velocity, displacement, and pressure after updates from each component of the EMHD model for a single time step

Mean and maximal velocity magnitudes after each update step are reported in Table 3.2. **A**. Contour plot of the velocity magnitude (m/s) with streamlines and arrows indicating flow directions due to the Lorentz force update. Largest velocity contour regions are around the two electrodes. Of note, flow direction trends downward and relatively perpendicular to the phantom boundaries. **B**. Velocity plot after update for convection shows an increase in overall velocity magnitude but not in direction relative to A. **C**. Velocity plot after update for viscosity shows a significant decrease in maximal velocity magnitude relative to A and B, with the high velocity contour regions around the electrodes and the center of the phantom. Streamline directions are grossly unchanged from A and B. **D**. Velocity plot after update for pressure shows increase in maximal velocity magnitude with similar high velocity contour regions around the electrodes and in the center of the phantom relative to C, but with new low velocity contour regions at the top and bottom. Of note, there is a shift in streamline directions trending more parallel to the phantom boundaries relative to A, B, and C. **E**. Plot of displacement magnitude (m) with streamlines after update for pressure shows highest displacement in regions around the electrodes, with streamline trends similar to D. **F**. Contour plot of pressure showing a pressure gradient from bottom to top opposing the general flow direction in C, corresponding to the low flow contour regions in D.

The Lorentz force induced particle flow velocity in the EMHD model in the first time step (Figure 3.6A) generally trends downward as from electromagnetic drift theory (Figure 3.2), and has the same velocity magnitude distribution and flow direction as the particle drift model results (Figure 3.5C). Additionally, the velocity magnitude for the EMHD model (mean of 0.39 m/s, max of 20 m/s) and particle drift model (mean of 0.30 m/s, max of 20 m/s) are similar and both are highest in a small region immediately around each electrode (Figure 3.6A and Figure 3.5C). After updates from other terms in the EMHD model, the Lorentz force induced EMHD flow (Figure 3.6A) changes in magnitude (Table 3.2) and direction (Figure 3.6).

After convective acceleration, the flow velocity maintains the same direction (Figure 3.6B) but increases in magnitude (mean of 0.41 m/s, max of 150 m/s). After updating for viscosity, the velocity maintains direction but changes in the distribution of high flow areas, from being limited near the electrodes to, instead, including a large

central area (Figure 3.6C), and decreasing the velocity magnitude mean ~2x and the maximum ~500x (mean of 0.21 m/s, max of 0.31 m/s). After updating for the pressure gradient, the direction of flow velocity (Figure 3.6D) and displacement (Figure 3.6E) shifts to a more circular flow pattern parallel to the phantom boundaries, with the majority of the phantom particles experiencing downward flow but at a ~4x lower mean and slightly higher maximal magnitude (mean of 0.052 m/s, max of 0.37 m/s). The areas of greatest change in flow velocity occur in the top and bottom of the phantom where the pressure magnitude is highest (Figure 3.6F).

3.3. Discussion of the EMHD flow effect and particle drift

An initial estimate of electromagnetic drift velocity in the LEI experiments by Wijesinghe and Roth showed magnetohydrodynamics' promise as a potential contrast mechanism for LEI [34]. Their estimate, on the order of 1 m/s, was based on a uniform 50 V/m electric field. Our particle drift model represented the electric field more accurate to the experimental setup, showing a non-uniform electric field (magnitude at grid points had a minimum of 0.98 V/m, mean of 13.96 V/m, and maximum of 1911 V/m). Our model predicted range of velocities (minimum of 0 m/s, mean of 0.12 m/s, and maximum of 20 m/s) including the electromagnetic drift velocity estimate, was consistent with accepted electromagnetic theory [58, 59].

The mean and maximal particle displacements predicted using the Reynolds transport method in the particle drift model were approximately 10x higher than those

using the particle tracking method. This is an overestimation of particle displacements likely because the displacements were computed at fixed grid points without accounting for particle motion that would result in lower Lorentz-induced velocities for each particle as it moved farther away from the electrodes where the electric field forces are smaller. Overestimation of the particle displacement using the Reynolds transport method was apparent since the maximal displacement using that method was 62 cm, longer than the dimensions of the phantom (10 cm diameter). However, since the Reynolds transport method computation for ϕ_R accounted for particle motion, the relative signal changes for that method (mean of -23% and maximum of -100%) are higher but similar in order of magnitude to those of the Reynolds transport method (mean of -18% and maximum of -96%).

The downward trend in flow velocity direction of the EMHD model (Figure 3.6A) and particle drift model (Figure 3.5C) is also supported by electromagnetic drift theory (Figure 3.2): with the magnetic field pointing in the +z direction and the electric field pointing in the -x direction (for a positive current pulse), the drift velocity trends in the **E** x **B** direction, *i.e.*, the -y direction. In the EMHD model, the simulated pressure gradient (Figure 3.6F) opposes the downward direction of the Lorentz force induced velocity, with higher pressures near the lower boundary where particle collisions are greatest, which is supported by accepted EMHD theory [58].

In Figure 3.3A the mean particle drift velocity within the phantom linearly increases during the current-on periods due to the Lorentz force, while it remains flat during current-off periods due to the lack of resistive forces. Hence, the effect of the

oscillating gradients in this model incrementally ramps up velocity during each pulse, with a velocity stacking effect driving the particle displacements. Thus, the mean particle displacement continually increases quadratically (Figure 3.3B) both during current -on and -off periods of the LEI pulse sequence (Figure 3.1C). The LEI principle states that optimal contrast is achieved with all motion occurring during one gradient lobe while no motion occurs during the opposing gradient lobe [42]. Even with a continual increase in displacement during both lobes, there is still a detectable signal loss due to the quadratic increase creating a difference in dephasing and rephrasing between each pulse (Table 3.1). A linear increase in particle displacement would instead cause a rephasing equal to the dephasing and ultimately zero signal change.

With resistive forces in the full EMHD model, flow velocity rapidly increases to a steady-state value after achieving a force balance, and then rapidly slows to zero during the current-off periods when the Lorentz driving force is zero (Figure 3.4A), as opposed to the incremental ramping up of velocity in the particle drift model (Figure 3.3A). The EMHD model dynamics therefore create a greater difference in particle displacement rate during the current -on vs. -off periods. Hence, despite the lower displacement magnitudes in the EMHD model, the relative difference between displacements in the current on vs off periods may still add enough ϕ_R to create a detectable relative signal change which we will explore in the next chapter.

The distribution of relative signal loss from the particle drift model results (Figure 3.5B) does not correlate well with the experimental images of Truong et al. [42]. This is likely in part due to the boundary conditions and the velocity field of this model causing

particles to stay at the phantom boundaries rather than circulate around parallel to them, which may affect the signal distribution. Also, the lack of resistive forces causes the particles to distribute symmetrically in the upper and lower hemispheres of the phantom and experience higher displacements causing higher signal losses, especially near the electrodes. The EMHD model on the other hand, with forces other than particle drift, may non-uniformly shift particle direction which could cause the resulting relative signal change to adopt a more asymmetric appearance as in the experimental images.

The difference in the experimental LEI images and the particle drift simulation images was studied further by accounting for these other forces in the EMHD model. The mean and maximal magnitude (Table 3.2) and direction (Figure 3.6) of velocity and displacement in the phantom generated by the Lorentz force in the first time step is significantly changed after updating velocity for several other terms in the EMHD model. Convective acceleration generally increases velocity magnitude without changing direction. The viscosity globally decreases velocity magnitude, especially for particles outside of the central region of the phantom, without changing direction. A pressure gradient develops due to the top to bottom direction of Lorentz-force induced flow, causing flow velocity direction to change significantly with flow lines ending up more parallel to the phantom boundary with a further decrease in mean velocity.

Overall, the difference between the particle drift model flow and the EMHD model flow is that the other EMHD forces slow the flow speeds and shift flow direction from being relatively perpendicular to the boundaries to more circular flow which is relatively parallel to the phantom boundaries, while maintaining the bulk of particle flow

trending downward. Their overall effect after one time step appeared to be symmetric, but the overall effect of these forces over the entire course of the LEI protocol on the relative signal change cannot be determined without full time course simulation images from the EMHD model. Therefore, in the next chapter we will compare model images at the end of the entire LEI protocol with the results from an electrolyte phantom experiment and determine the accumulated effect on the velocity, displacement, pressure, and relative signal change.

Since the LEI experiments provide information on the signal change per voxel, it may be useful in the future to perform further verification of our computational models using other results, such as displacement. For a 50 V alternating current applied at 100 Hz (10 msec pulse width) to conductive gels under a 1.5 T MRI scanner, displacement amplitudes on the order of 65-75 μm were measured [47], which are much lower than the mean displacements in the particle drift (0.92 cm) and EMHD (1.9 cm) model. However, these displacements were measured in an elastic gel with higher viscosity than water. In addition, because of the alternating current, the gels were displaced in an oscillatory manner which, over the course of the entire pulse sequence may correspond to total particle motion orders of magnitude higher. It may also be possible in future experiments to verify our computational model results based on velocity measurements using a technique referred to as magnetic resonance velocimetry (MRV), which is capable of measuring velocities ranging from ~10 m/s to 1 cm/day [64].

4. Model and experiment LEI image comparison

The computational models described in Chapter 2 were developed to simulate the electrolyte-filled phantom experiments of Truong et al. [42]. After comparing the results of the particle drift and EMHD models in the previous chapter, we now compare images obtained from each of the three computational models with images from three cases of the LEI experiment. The models explored are: ion flow based on the study by Truong et al. [42], particle drift based on the estimates by Wijesinghe and Roth [34], and EMHD of a conducting fluid. Our modeling assumptions and analysis reflect our primary interest in the overall scale of the LEI signal loss in comparing the model results to those of the experiments. Therefore, an in-depth analysis of the implications of the spatial distribution of signal loss or other output parameter values was not performed.

4.1. Model and experiment image generation

A full explanation of the phantom model parameters, LEI protocol, and computational methods used can be found in Chapter 2. For our computational methods we ignored the magnetic field changes from the gradients, which allowed us to compute the electric field generated by the electrical activity independently of the magnetic field effects and fluid motion. Thus, for each model we implemented a two-part method to: 1) compute the electric and magnetic field effects on fluid velocity and displacement, then 2) compute the induced signal loss based on fluid displacement along the applied magnetic field gradients.

All model simulations, result analysis, and display were performed in MATLAB v7.11. The primary numerical results computed for all models were velocity, displacement, and signal loss. Maps of the velocity were displayed using a grayscale contour plot of the velocity magnitudes overlaid with streamlines of the velocity trajectories and arrows indicating flow direction. Mean and maximal velocity and displacement within the phantom were computed at the end of the last current pulse and at detection, respectively. In addition, maps of the electrical potential and pressure within the phantom were displayed using grayscale contour plots at all Navier-Stokes finite difference grid points. Lastly, maps of the relative signal change were displayed for each voxel simulated using a grayscale map with bounds set at -40% and 40% to match the experimental results [42]. Mean and maximal relative signal differences in the phantom were also reported.

For model versus experiment image comparison we obtained raw signal images from the experiments of Truong et al. [42] and reprocessed them to display only the central 10 cm region of the image to match the region used for our model results display. The images were displayed as the relative percent signal change S_R: difference in the detected signal in the case with an applied current (S) and the case with zero applied current (S_0), divided by S_0.

4.2. Computational model and experimental phantom LEI image comparison

Using a 5 mA current stimulus and the standard mobility value for copper μ = 5.4×10^{-8} (m/s)/(V/m) [34] and 24 water molecules moving with each ion, the first model (ion flow) resulted in a maximal displacement and signal loss of only 5×10^{-5} cm and 2.2×10^{-5}%, respectively. Using the higher mobility value of μ = 0.128 (m/s)/(V/m) from [42], the maximal displacement was unrealistically higher at 13 cm, beyond the bounds of the 10-cm phantom due to the lack of a boundary condition, and the maximal signal loss was only 0.027%. With either mobility value, there were no appreciable areas of signal loss in the simulated image despite overestimating the ion-water interactions in this model.

For the same 5 mA current stimulus, the second model (particle drift) approximation using the Reynolds transport method and grid resolution of four particles per voxel resulted in a mean - maximal velocity, displacement, and signal loss of 0.30 - 20 m/s, 0.92 - 62 cm, and 23% - 100%, respectively, showing good agreement with previous analytical approximations of the magnetohydrodynamic effect [34] (see section 1.1). However, the simulated image (Figure 3.5B) has a symmetric pattern of relative signal loss, unlike the asymmetric pattern with more signal loss in the bottom half of the experimental image for the same LEI protocol [42].

For the same 5 mA current stimulus, the third model (EMHD) using the Reynold's transport method and a higher grid resolution of 16 particles per voxel, resulted in a mean - maximal velocity, displacement, and signal loss of 0.34 - 36 m/s, 1.9

- 9.2 cm, 17% - 100%, respectively (Table 4.1 below), similar in mean magnitudes to the particle drift results but with lower maximal displacement (9.2 cm vs. 62 cm). The EMHD simulated image (Figure 4.1A below) had three large areas of signal loss in the lower half of the phantom similar in location to that of the experiment (Figure 4.1B below). However the EMHD model image differed from that of the experiment by having no overlap between the signal loss regions and no areas of signal gain.

Table 4.1: EMHD model mean and maximal velocity, displacement, and signal loss for ±5 mA current pulses

	Mean	Max
Velocity at the end of the final current pulse	0.34 m/s	36 m/s
Displacement at the end of the final negative gradient lobe	1.9 cm	9.2 cm
Relative signal loss at detection	17%	100%

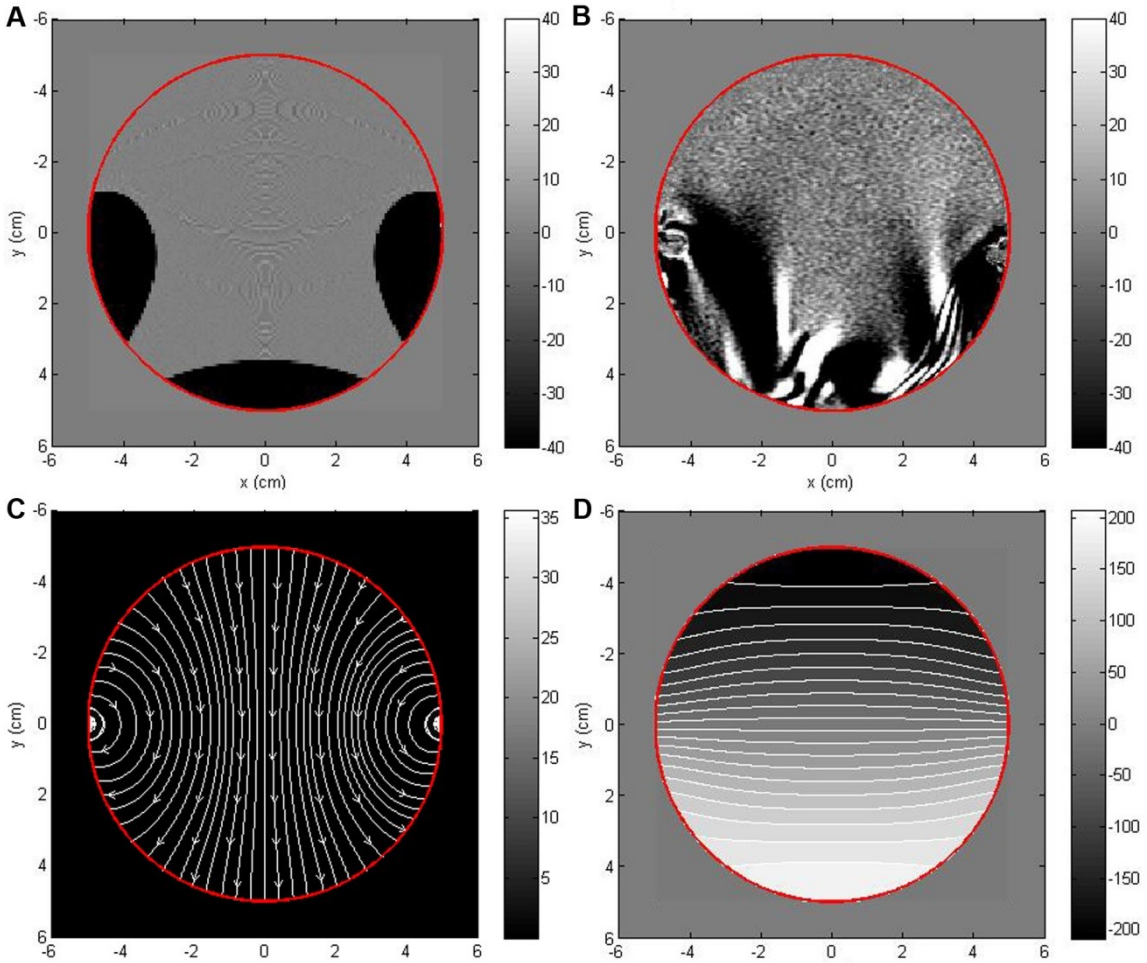

Figure 4.1: Experimental signal image and EMHD maps of signal, velocity, and pressure for a 5 mA current pulse

A. Image of the relative signal change from the EMHD model, showing three main regions of signal loss in the lower half of the phantom. The mean and maximal relative signal loss values are reported in Table 4.1. **B**. Corresponding image of the relative signal from the experiment showing three main areas of signal loss overlapping in the lower half of the phantom. Areas of signal gain were due to flow effects, which were ignored in the EMHD model. **C**. Contour plot of the velocity magnitude (m/s) with streamlines and arrows indicating flow directions at the end of the final current pulse. Mean and maximal velocity magnitudes are reported in Table 4.1. Of note, flow direction trends downward. **D**. Contour plot of pressure values (Pa) at the end of the final current pulse. Pressure values are minimal at the top and maximal at the bottom of the phantom, resulting in a pressure gradient that opposes the direction of flow velocity.

The electric potential contours in the EMHD model with the 5 mA current stimulus on show a range of potentials from +2.5 V to -2.5 V extending from the point sources at the left and right ends of the phantom, respectively (Figure 3.1B). When the current stimulus was turned off, the potential distribution was uniformly zero throughout. At the end of the positive gradient lobe, the resulting flow velocities computed on the Navier-Stokes finite differences grid were maximal and trended downward (Figure 4.1C). Areas of highest flow velocity were around the electrodes. Furthermore, the EMHD model was able to report pressure values in the phantom with a pressure gradient (Figure 4.1D) that opposes the general direction of velocity. Pressure was minimal at the top and maximal at the bottom of the phantom where fluid velocities trended toward.

For a current stimulus with an equal magnitude but opposite polarity (-5 mA), contours of the electric potential (L-R mirror image of Figure 3.1B), velocity (Figure 4.2C below), and pressure (Figure 4.2D below) were identical but opposite in direction as compared to the case with a positive current polarity (Figure 4.1B, C, D). In addition, the magnitude of mean and maximal velocity, displacement, and relative signal loss values were equal. Lastly, the areas of signal loss were similar but occurred in the top half of the phantom (Figure 4.2A below) as compared to the bottom (Figure 4.1A). These results show that the LEI contrast is reversible when changing the current polarity, which was also observed in the experiments (Figure 4.1B vs. Figure 4.2B below).

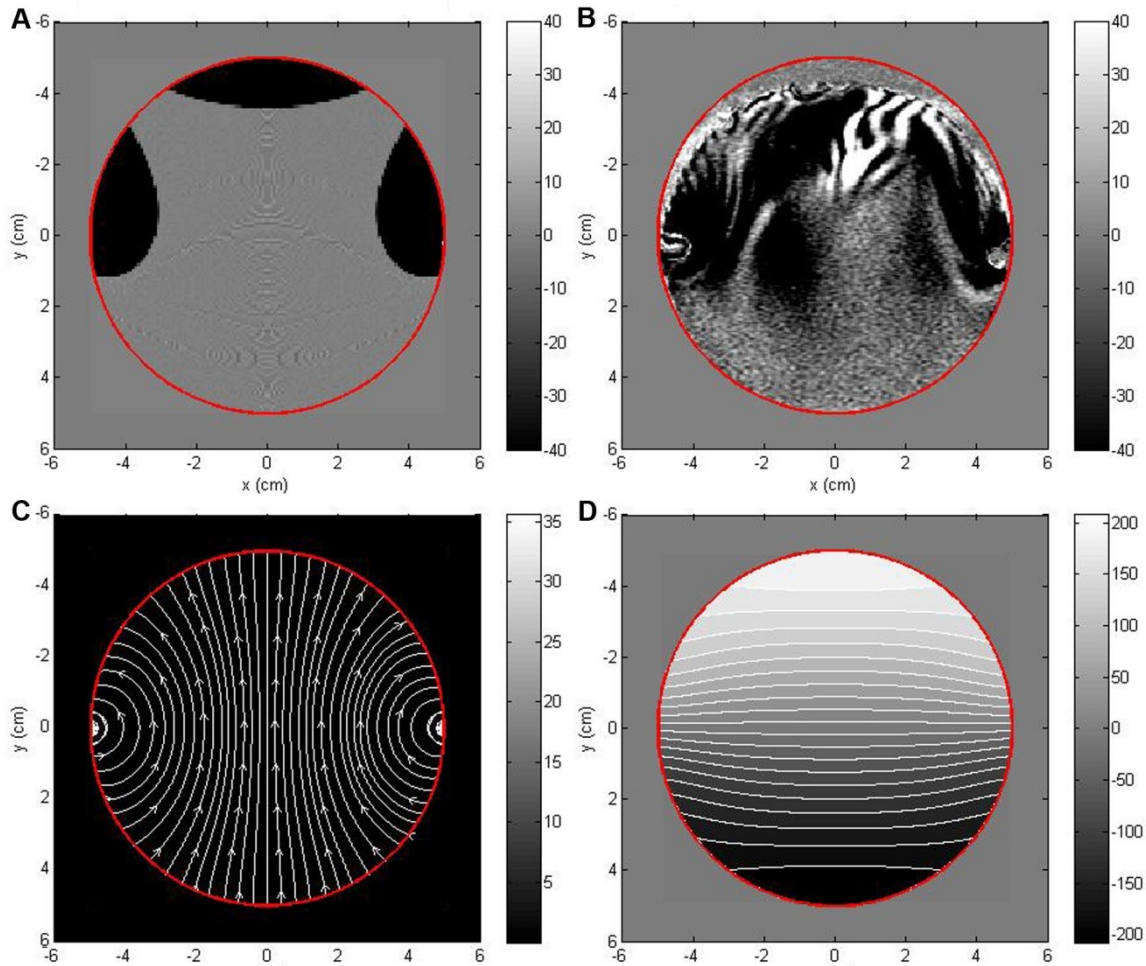

Figure 4.2: Experimental signal image and EMHD maps of signal, velocity, and pressure for a -5 mA current pulse

A. Image of the relative signal change from the EMHD model, showing three main areas of signal loss in the upper half of the phantom. The mean and maximal relative signal loss values are reported in Table 4.1. **B**. Corresponding image of the relative signal change from the experiment showing three main areas of signal loss overlapping in the upper half of the phantom. Areas of signal gain were due to flow effects, which were ignored in the computational model. **C**. Contour plot of the velocity magnitude (m/s) with streamlines and arrows indicating flow directions at the end of the final current pulse. Mean and maximal velocity magnitudes are reported in Table 4.1. Of note, flow direction trends upward. **D**. Contour plot of pressure values (Pa) at the end of the final current pulse. Pressure values are maximal at the top and minimal at the bottom of the phantom, resulting in a pressure gradient that opposes the direction of flow velocity.

We next used a smaller current to understand how the LEI contrast scales with current strength. For 0.5 mA pulses, the mean - maximal velocity, displacement, and signal loss were 0.034 – 3.6 m/s, 0.23 - 6.1 cm, 2.54% - 100%, respectively (Table 4.2 below).

Table 4.2: EMHD model mean and maximal velocity, displacement and signal loss for 0.5 mA current pulses

	Mean	Max
Velocity at the end of the final current pulse	0.034 m/s	3.6 m/s
Displacement at the end of the final negative gradient lobe	0.23 cm	6.1 cm
Relative signal loss at detection	2.54%	100%

The simulated image shows regions of greatest signal loss around the electrodes and a thin region of signal loss at the bottom (Figure 4.3A below). However, the signal loss seen in the experimental image (Figure 4.3B below) was focused mainly around the electrodes, extending inward with no obvious signal loss at the bottom.

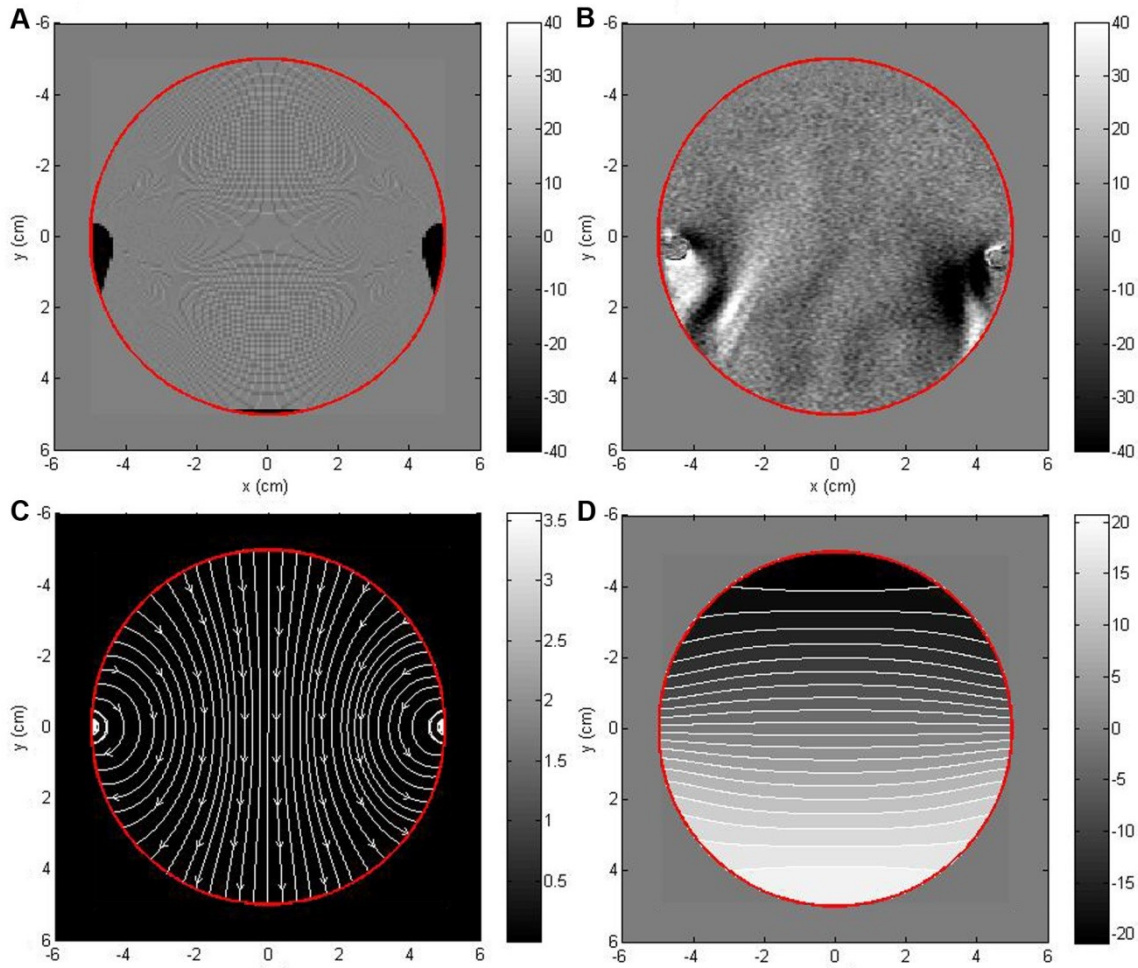

Figure 4.3: Experimental signal image and EMHD maps of signal, velocity, and pressure for a 0.5 mA current pulse

A. Image of the relative signal change from the EMHD model, showing regions of greatest signal loss focused around the electrodes. Mean and maximal relative signal loss values are reported in Table 4.2. **B**. Corresponding image of the relative signal change from the experiments, showing regions of greatest signal loss focused around the electrodes. **C**. Contour plot of the velocity magnitude (m/s) with streamlines and arrows indicating flow directions at the end of the final current pulse. Mean and maximal velocity magnitudes are reported in Table 4.2. Of note, flow direction trends are similar to Figure 4.1C. **D**. Contour plot of pressure values (Pa) at the end of the final current pulse. Pressure values are maximal at the top and minimal at the bottom of the phantom, resulting in a pressure gradient that opposes the direction of flow velocity.

4.3. Discussion of computational LEI models

To gain a better understanding of the LEI contrast mechanisms proposed in previous studies [34, 42], three different models of the Lorentz effect were developed and the simulated images were compared with those obtained in the phantom experiments of Truong et al. [42]. In the first model, the Lorentz effect on ion flow was explored and found to be incapable of explaining appreciable signal losses, as it resulted in only << 1% maximal signal loss regardless of the mobility value selected. The lack of LEI signal loss in the ion flow model was likely due to the limited amount of water molecules associated with each travelling ion. These results show that the Lorentz effect on ions is not a principal mechanism explaining the signal losses observed in the LEI experiments [42], regardless of the mobility value.

Particle drift and EMHD on the other hand, were able to demonstrate detectable LEI signal losses. In addition, the directionality, reversibility, and scalability of the velocity, pressure, and signal loss patterns based on current polarity and amplitude were demonstrated with EMHD. From initial results, flow velocity trends in the particle drift model and EMHD model were qualitatively explained and compared based on electromagnetic drift theory and EMHD theory in section 1.1.

Comparing the quantitative results of particle drift vs. EMHD for a 5 mA stimulus, there was a similar mean (0.30 vs. 0.34 m/s) and lower maximal (20 m/s vs. 36 m/s) velocity, lower mean (0.92 vs. 1.9 cm) and higher maximal (62 cm vs. 9.2 cm) displacement, a higher mean (23% vs. 17%) and similar maximal (100% vs. 100%) signal loss, as well as patterns of signal loss that did not match the experiments as well as the

EMHD model results did. The overall flow velocity direction, and mean velocity, displacement, and signal loss magnitudes in the particle drift model approximate those of the EMHD model. However, the viscosity forces, convective acceleration, and pressure gradients in the fluid space of the EMHD model, especially near the boundaries, are needed to accurately predict the maximal velocity, maximal displacement, and distribution of signal loss in the phantom.

Comparing the EMHD model vs. experimental results, quantitatively, mean signal loss in the field of view was higher for the two stimulus strengths tested (17% vs. 9.06% for 5 mA and 2.54% vs. 1.68% for 0.5 mA), likely due to signal gain in the experimental images from flow effects [42] reducing the mean loss. EMHD model simulations at more current strengths could help explain these differences as a general trend or due to other effects not considered in the model, and will be explored in the next chapter. Also, the space outside of the phantom is of a different composition than inside the phantom with different magnetic properties (air instead of electrolyte solution) and the relative signal outside of the phantom bounds in the experiment images (clipped for comparison and not shown in Figure 4.1B, Figure 4.2B, and Figure 4.3B) are not uniformly zero, likely due to noise or artifact. Therefore in future simulations it may be possible to improve comparison between the experiment and model results by computing and reporting mean values only accounting for voxels within the phantom and not the field of view as a whole. If a general trend is seen, a method to normalize and account for signal gain in the experimental images may allow for better quantitative predictions of experimental results based on the EMHD model results.

Comparing the results qualitatively, the main regions of signal loss were in similar locations. As a general trend, for low current amplitudes (from 0 to 0.5 mA) the main areas of signal loss were near the electrodes and began to include a thin region of signal loss near the lower boundary of the phantom as the current was increased. For high positive current amplitudes (+1 to +5 mA) signal loss expanded from near the electrodes to a region along the lower boundary of the phantom. For high negative current amplitudes (-1 to -5 mA), signal loss areas flipped to the upper half of the phantom. In general, experimental signal loss regions differed from those of the model in that at lower currents signal loss around the electrodes extended more inward while at higher currents there was some overlap between the signal loss areas (Figs 2A, 2B). This distribution of signal loss was likely affected by the physical dimensions of the experimental electrodes which extended inward (2 mm diameter, 4 mm length) [42], while the electrodes were simulated as point sources in the EMHD model.

From our results, we can make some predictions regarding optimization of LEI in other settings. For example, our simulations generated higher signal losses with narrower current pulses and gradient oscillations (results not shown), hence allowing improved detection of rapidly alternating electrical activity. In addition, with a 10x smaller current strength, mean, and maximal velocity also scaled 10x less, but mean and maximal displacement scaled 8.3x and 1.5x less, and mean signal loss scaled 6.7x less while maximal signal loss remained at 100%. Because displacement and signal loss scales less quickly than velocity for lower current strengths, it may be possible to detect smaller

current strengths, but the exact limit of dipole strengths detectable using LEI have yet to be explored with our model.

Since the main objective of this study was to investigate whether EMHD can explain the LEI contrast observed in the experiments of Truong et al. [5], the simulations were performed with the same setup and parameters as those used in the experiments to compare the results. The only difference was rectangular gradients used in our models as compared to trapezoidal gradients in the experiments, which was expected to be of minimal impact and not explored. Yet, further studies must be performed with different setups and parameters more relevant to *in vivo* applications to optimize the LEI technique and investigate its feasibility for imaging neuronal activity in the cerebral cortex.

First, simulations need to be performed with a large number of smaller dipoles oriented in multiple directions to simulate an active portion of cortex (with 10^5 pyramidal cells / mm^2 and 1000 synapses per neuron [39]) rather than the single dipole used in this study to simulate the phantom. Second, even though the current densities with an LEI signal detected in our study (64 - 640 nA/mm^2) are of similar order magnitude as current densities in activated cortex (100 - 250 nA/mm^2 [39]) and despite the fact that mean and maximal signal loss scales less than the reduction in current strength, simulations also need to be performed with 10^3x smaller currents similar to those generated by cortical axons and dendrites (1 - 10 nA vs. 0.5 - 5 mA simulated in this study) to better estimate the sensitivity of LEI for imaging neuronal currents in the cerebral cortex. Finally, further studies are needed to explore other aspects of the LEI protocol (e.g., the frequency of the

oscillating gradients, which must be synchronized to the neuronal currents of interest) to optimize its use for different patterns of neuronal activity.

In conclusion, LEI's demonstrated ability to depict signal loss in the presence of electrical activity in ionic solutions is a step toward its benefit as a potential ncMRI method. We have demonstrated that EMHD is a principal mechanism explaining the patterns and magnitudes of signal loss in the LEI phantom experiments of Truong et al. [5]. The EMHD model has the added benefit of providing information regarding velocity, displacement, pressure, and other parameters not readily available in an actual experiment. Thus, the EMHD model is a robust platform for studying the LEI contrast mechanism and optimizing LEI protocols to detect electrical activity in other settings. Through further study of the EMHD model and by developing model-optimized LEI experiments we can more readily validate LEI for use as an ncMRI method, which may find broad applications in basic and clinical neurosciences [1].

5. Measuring current strength and fluid dynamics with LEI based on EMHD

In the previous chapter we used a particular LEI protocol to qualitatively and quantitatively explore the EMHD model simulation images. The results showed magnitudes and patterns of signal loss similar to those in the electrolyte phantom experiments of Truong et al. [42] for a relatively large current (5 mA), a polar opposite current (-5 mA), and a smaller current (0.5 mA) applied to the phantom electrodes. The EMHD model's ability to reproduce the magnitude and distribution of the relative signal loss supports its applicability to further studies of LEI contrast.

LEI's demonstrated ability to depict signal loss in the presence of electrical activity is a promising step toward its use as a potential ncMRI method. To improve it as a method of directly mapping electrical activity we must determine the relationship between the LEI relative signal change and the underlying current strength over a range of current strengths. Also, evaluating the EMHD model's ability to predict similar trends in LEI signal change for varying current strengths will enhance its utility as a method to study and optimize LEI contrast. Therefore, in this chapter we will analyze and compare results from the phantom experiments and EMHD model simulations to determine LEI's ability to map changes in the underlying current strength using changes in the relative signal.

To better understand EMHD and LEI contrast, we will also analyze the current strength dependence of other parameters in the EMHD model not readily available from the experimental phantom, which underlie the LEI contrast mechanism. Studying the

underlying dynamics will be helpful in optimizing an LEI protocol to detect signal changes for a given electrical activity. Furthermore, we will discuss potential EMHD model simulations that will aid in studying and optimizing the utility of LEI as an ncMRI method for human brain mapping.

5.1. Measuring current strength using the LEI signal

To study the relationship between the LEI relative signal change and the underlying current strength we perform multiple EMHD model simulations of the LEI protocol for the electrolyte phantom (Figure 3.1) using the full range of currents strengths from the experiments (I = -5, -2, -1, -0.5, -0.2, -0.1, 0, 0.1, 0.2, 0.5, 1, 2, 5 mA). The model simulations use the Reynolds transport method and a finite difference grid of 16 points for each of the 128 x 128 MRI voxels (512 x 512 grid points) to explore the relative signal change dependence on current strength. We analyze results from the EMHD model simulations and the phantom experiments to determine the relationship between the LEI relative signal change and the underlying current strength, and compare the model and experiment trends to see if they are similar.

With the permission of Truong and Song, we obtained raw image files of the MRI signal from the phantom experiments depicted in Fig. 3 of their paper [42]. As discussed in section 4.3, magnetic properties of the phantom contents vary with that of the air around it. Hence, instead of computing the relative signal changes based on the mean signal within the *full field of view* of the phantom with zero current, we reprocessed the

images to compute the relative signal change S_R based on the mean signal with zero current *only using voxels within the central 10-cm diameter circular phantom region* based on the equation below.

$$S_R = \frac{S - S_0}{S_m} \tag{5.1}$$

In the above equation, S_R is computed for each voxel within the phantom based on S, the total signal strength in that voxel in the current-on image S_0, the total signal strength in the same voxel in the current-off image and S_m, the mean signal strength of all voxels within the central 10-cm diameter phantom area in the current-off image. For all experiments, S, S_0, and S_m are non-negative ranging in values from 0 to 200 [42]. Instead of reporting signal loss as in the previous chapter, S_R can indicate a signal loss or gain where $S_R > 0$ indicates relative signal gain and $S_R < 0$ indicates relative signal loss.

We report minimum, mean, and maximum S_R using only voxels within the phantom. Ignoring voxels outside the phantom increased the computed mean compared to using the entire field of view, which has relatively little signal change in the space outside the phantom. In addition we computed the percentage of voxels within the phantom with SR < t (SRLT, where the threshold t = - 40%). The minimum, maximum, and mean values of S_R and SRLT in the phantom for the range of current strengths tested are shown in Figure 5.1 below.

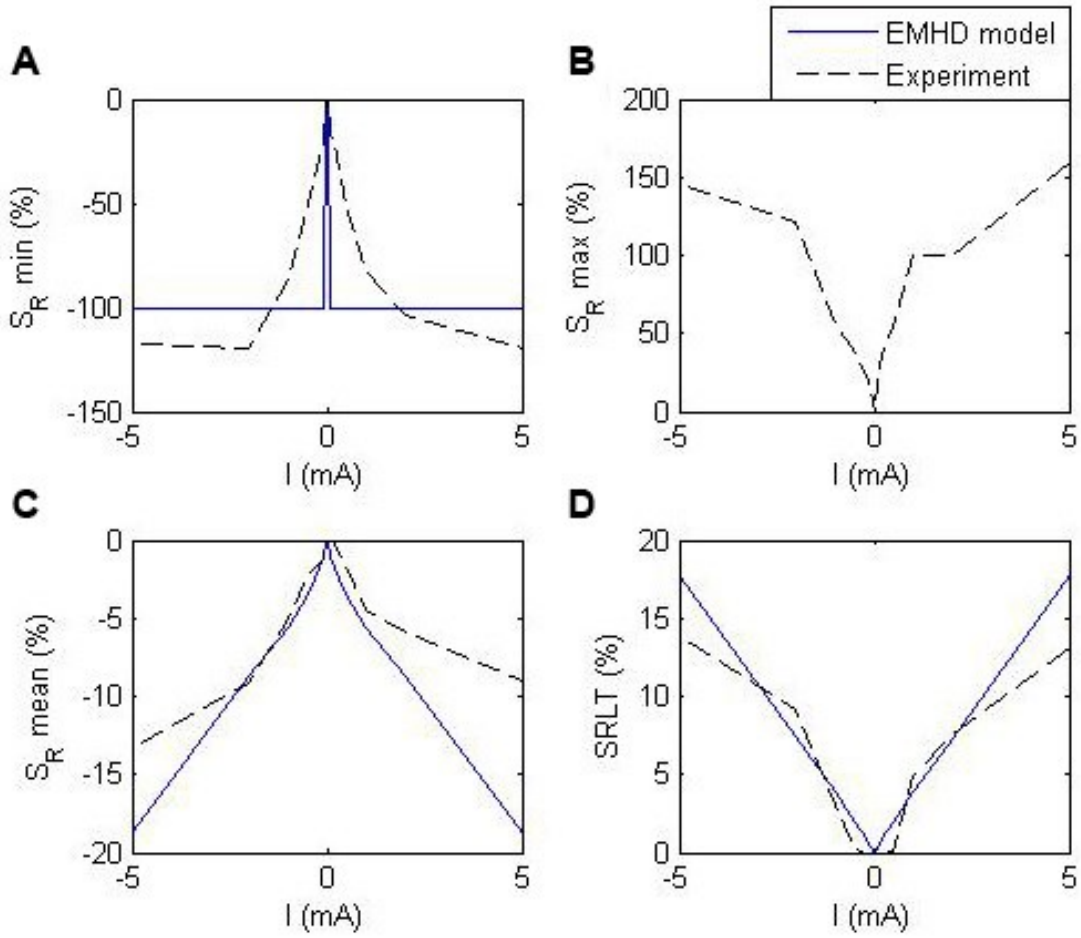

Figure 5.1: EMHD model and experiment relative signal change in the phantom over a range of current strengths

Current strengths I = -5, -2, -1, -0.5, -0.2, -0.1, 0, 0.1, 0.2, 0.5, 1, 2, 5 were used in the LEI experiments of the electrolyte phantom and corresponding EMHD model simulations (Figure 3.1). Model results (solid line) are compared to experiment results (dashed line). **A**. Relative signal change (S_R) minimum predicted by the EMHD model is consistently -100% except for I = 0, whereas experiment S_R minimum is below -100% for higher current strengths |I| > 1 mA and higher than 100% for lower current strengths |I| ≤ 1 mA. **B**. Model predicted S_R maximum is 0% for all current strengths except for I = 0, whereas experiment S_R maximum is above 0% due to flow effects that were ignored in the EMHD model. **C**. Model predicted S_R mean closely matches that of the experiment for lower current strengths |I| ≤ 1 mA. Experiment S_R mean is greater for higher current strengths |I| > 1 mA. **D**. The percent of voxels in the phantom with S_R < -40% (SRLT) in the model and experiment are similar for larger currents strengths |I| = ≥ 1 mA since experiment SRLT is zero (sub-threshold) for |I| < 1 mA.

In Figure 5.1A, the relative signal change minimum corresponds to the maximum relative signal loss. The results from the experiment in this figure show increasingly large maximum signal losses for higher current strengths, with signal losses greater than 100% for higher currents $|I| > 1$ mA. The EMHD model results on the other hand, show maximum signal losses of 100% (relative signal change of -100%) in all cases with an applied current. In Figure 5.1B, the experimental results show greater relative signal gains for increasing current strengths, whereas the EMHD model results have no signal gain at any current strength tested. In Figure 5.1C, the mean signal loss in the phantom increases as a function of current in both the experiment and EMHD model, showing good correlation for lower current strengths $|I| \leq 1$ mA. The EMHD model shows a linear relationship between the current strength and the mean signal change, whereas in the experiment, especially for higher currents $|I| > 1$ mA, the mean relative signal change decreases at an increasingly slower rate. In Figure 5.1D, SRLT was found to increase linearly with increasing $|I|$, and shows better correlation with the experiment than the results of Figure 5.1C.

To explore the distribution of relative signal change within the phantom, we study symmetry of the LEI contrast mechanism for the same range of current strengths. Dividing the phantom space into quadrants, we sum the total relative signal change in each quadrant and compute, using different pairs of quadrants, the proportion of total relative signal change (SRP) in the top, bottom, left, and right halves of the phantom, shown in Figure 5.2 below.

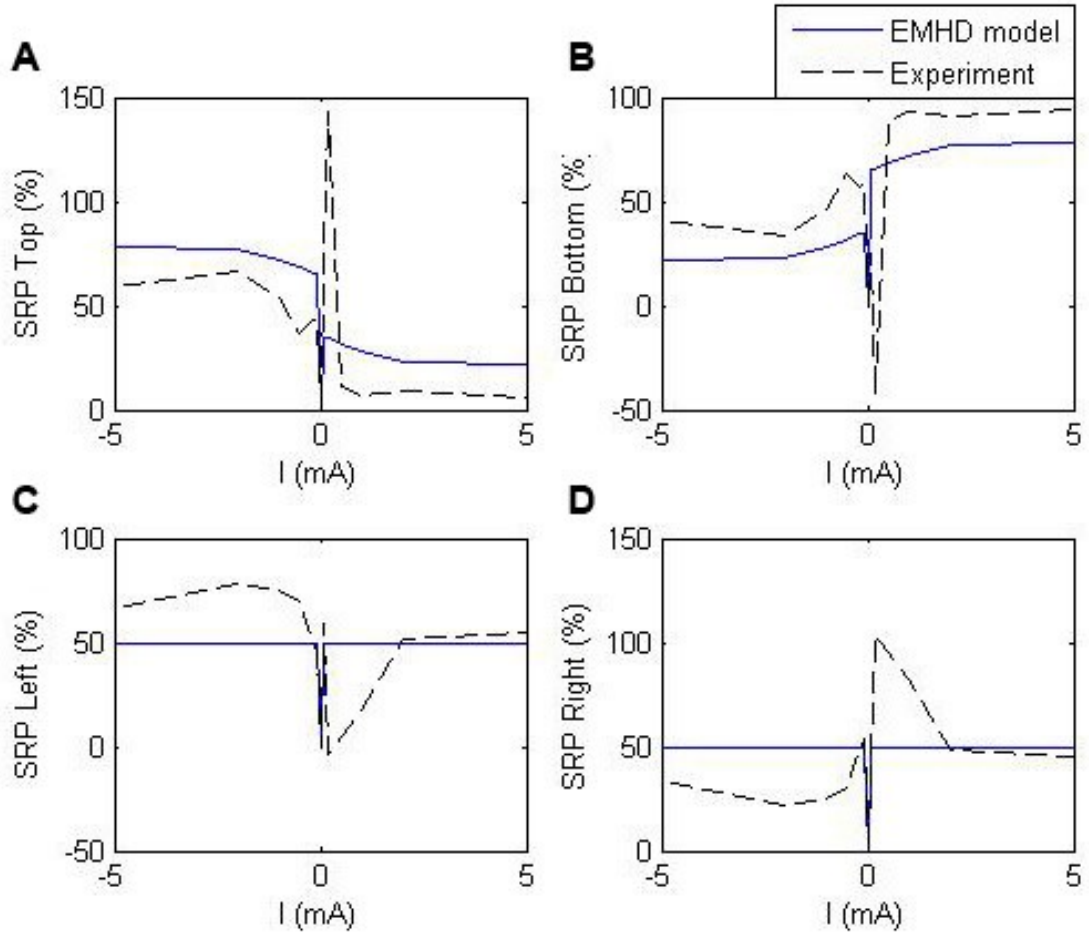

Figure 5.2: EMHD model and experiment proportion of the total relative signal change in different regions of the phantom over a range of current strengths
Current strengths I = -5, -2, -1, -0.5, -0.2, -0.1, 0, 0.1, 0.2, 0.5, 1, 2, 5 were used in the LEI experiments of the electrolyte phantom and corresponding EMHD model simulations (Figure 3.1). Model results (solid line) are compared to experiment results (dashed line). Relative signal change is summed and reported for each region as a percent of the total sum for all voxels in the phantom (SRP). **A**. SRP in the top half of the phantom predicted by the EMHD model is consistently ~20% higher than that of the experiment higher except for I = 0.1 and 0.2. **B**. SRP in the bottom half of the phantom predicted by the EMHD model is consistently ~20% lower than that of the experiment higher except for I = 0.1 and 0.2. **C**. SRP in the left half of the phantom is consistently 50% in the model, but varies for the experiment; generally higher for negative currents and lower for positive currents. **D**. SRP in the right half of the phantom is consistently 50% in the model but varies for the experiment; generally lower for negative currents and higher for positive currents.

In Figure 5.2A, SRP in the top half of the EMHD model phantom increases asymptotically for increasingly negative current strengths, corresponding with more signal loss in the upper half of the phantom as seen in Figure 4.2A for a negative current. Conversely, SRP in the top half of the EMHD model phantom decreases asymptotically for increasingly positive current strengths, corresponding with less signal loss in the upper half of the phantom as seen in Figure 4.1A for a positive current. In Figure 5.2B, the reverse trend is true for SRP in the bottom half of the EMHD model phantom. Compared to the EMHD model results, the same trends are generally true in the top and bottom halves of the experimental phantom except that SRP is consistently lower in the top half and higher in the bottom half of the phantom than in the EMHD model, and the SRP results for I = 0.1 mA in the top and bottom half of the experimental phantom are inconsistent with the general trend.

In Figure 5.2C and Figure 5.2D, SRP in the left and right halves of the EMHD model phantom are consistently 50% at all applied current strengths $|I| > 0$. The experimental results however, show higher SRP in the left vs. the right half for negative current strengths, and higher SRP in the right vs. the left half of the phantom for positive current strengths, with the increase in SRP toward either side being highest at $|I| \sim 1$ mA.

We also explore the number of voxels with relative signal change below a -40% threshold in the top, bottom, left, and right halves of the phantom, reported as a percentage of the total number of voxels in the phantom (SRLT), shown in Figure 5.3 below.

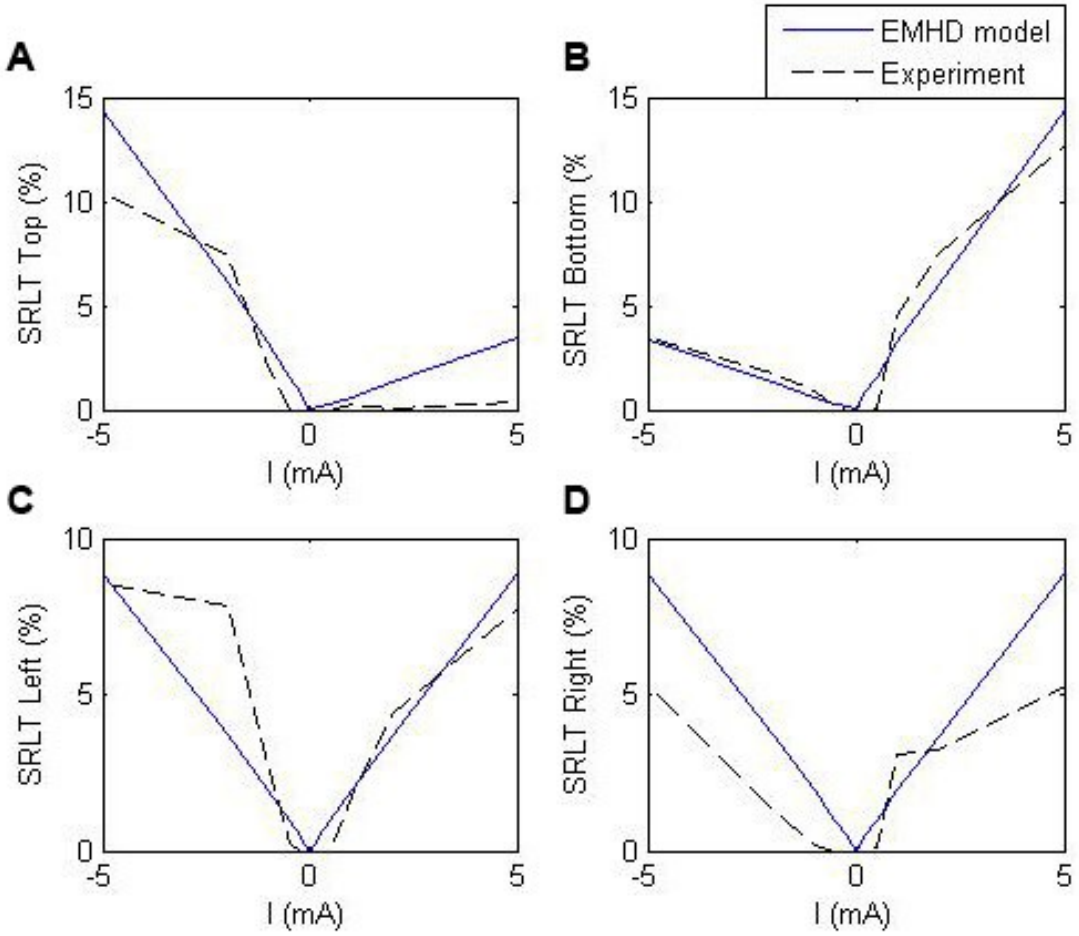

Figure 5.3: EMHD model and experiment percentage of voxels with relative signal change below a -40% threshold in different regions of the phantom over a range of current strengths

Current strengths I = -5, -2, -1, -0.5, -0.2, -0.1, 0, 0.1, 0.2, 0.5, 1, 2, 5 were used in the LEI experiments of the electrolyte phantom and corresponding EMHD model simulations (Figure 3.1). Model results (solid line) are compared to experiment results (dashed line). Voxels with relative signal change below the -40% threshold are given a value of one, summed and reported for each region as a percent of the total number of voxels in the phantom (SRLT). **A**. SRLT in the top half predicted by the EMHD model shows a similar relationship to current strengths as in the experiment. **B**. SRLT in the top half predicted by the EMHD model shows a similar relationship to current strengths as in the experiment. **C**. SRLT in the left half of the phantom is consistently 50% in the model, but varies for the experiment; generally higher for negative currents and lower for positive currents. **D**. SRLT in the right half of the phantom is consistently 50% in the model but varies for the experiment; generally lower for negative currents and higher for positive currents.

As shown in Figure 5.3A there is a linear relationship between the current strength and SRLT in the top half of the phantom. Additionally, the rate of increase of SRLT for increasingly negative current strengths is greater than the rate of increase of SRLT for increasingly positive current strengths. In Figure 5.3B there is a similar but mirror imaged linear relationship between SRLT in the bottom half of the phantom and the current strength, with a greater rate of increase for increasingly positive current strengths than the rate of increase of SRLT for increasingly negative current strengths. Furthermore, the EMHD model trends in Figure 5.3A and Figure 5.3B show improved correlation with those from the experiment, than the EMHD model and experiment trends in Figure 5.2A and Figure 5.2B.

In Figure 5.3C and Figure 5.3D a linear relationship exists between SRLT in the left and right halves of the EMHD model phantom and the current strength, with the same rate of increase in SRLT for increasingly negative and positive current strengths in both halves. Furthermore, the EMHD model trends in Figure 5.3C and Figure 5.3D show improved correlation with those from the experiment, than do the EMHD model and experiment trends in Figure 5.2A and Figure 5.2B.

Based on the EMHD model SRLT results in Figure 5.1D, the mean slope of the relationship between SRLT and the applied current strength I was computed. The mean slope was then used as a multiplier to compute the experiment predicted current strength I_E from SRLT measured in the experimental images for all current strengths tested. The comparison between the EMHD model and experiment predicted results are shown in the figure below.

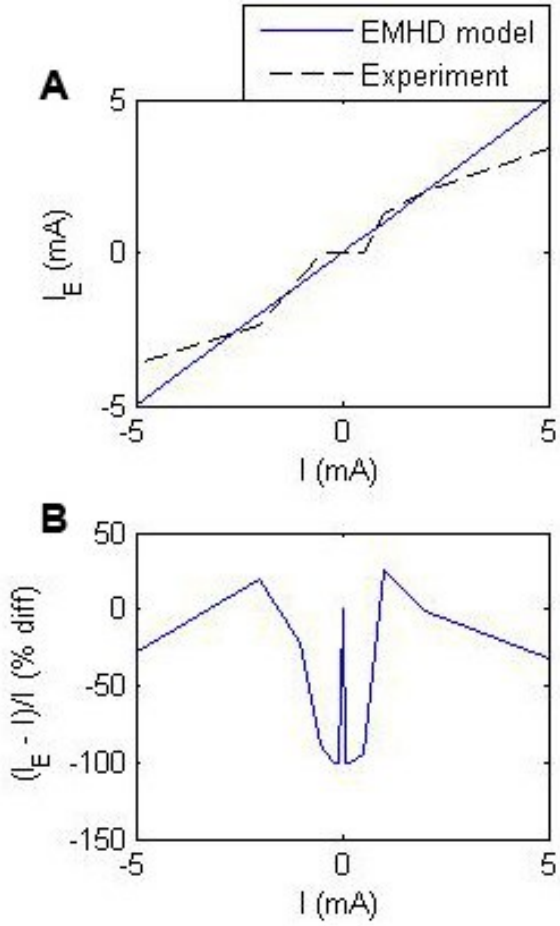

Figure 5.4: Measured current strength from LEI experiment images using SRLT and comparison with EMHD model results
Current strengths I = -5, -2, -1, -0.5, -0.2, -0.1, 0, 0.1, 0.2, 0.5, 1, 2, 5 were used in the LEI experiments of the electrolyte phantom and corresponding EMHD model simulations (Figure 3.1). Experiment and EMHD model images were used to compute SRLT as shown in Figure 5.1D, where the mean slope of the EMHD model trend was used to predict the experimental current strength (I_E) from experimental SRLT. **A**. EMHD model predicted I_E is linear and matches the applied current strength I, and the experiment predicted IE follows a similar trend. **B**. Experiment and model predicted I_E is on the same order of magnitude, where the percent difference between experiment and EMHD model predicted I_E is ≤ 100% for all current strengths tested.

Using SRLT from the experimental images, we are able to derive a measure of the applied current strength I_E based on EMHD model results (Figure 5.4A), which showed a similar trend as the EMHD model predicted values. The experimentally predicted I_E was

on the same order of magnitude as the actual applied current strength (I) based on the percent difference between the experimental I_E and actual I being ≤ 100% for all current strengths tested (Figure 5.4B).

5.2. Estimating fluid dynamics from the LEI signal

To better understand EMHD and the LEI contrast mechanism, we also analyze the dependence of the EMHD model electric field, velocity, displacement, and pressure on the current strength. The EMHD fluid dynamics variables in particular are not directly measurable in the experimental phantom. Yet, studying these dynamics that underlie LEI contrast, will aid in optimizing an LEI protocol to detect signal changes for a given electrical activity and will also allow for discussion of how to correlate experimentally measurable relative signal changes with the underlying electric field strength and fluid dynamics. In addition, knowing the experimental displacement and SRLT will allow us to predict the minimum displacement needed to generate a desired threshold of signal loss.

The EMHD variables were predicted from the experimental results over the full range of current strengths tested by computing I_E from the experiment images and applying it in a corresponding EMHD model simulation to generate a full panel of results. Comparisons of the EMHD model and LEI experiment predicted fluid dynamics variables and electric field strength dependence on the actual current strength I are shown in the figure below.

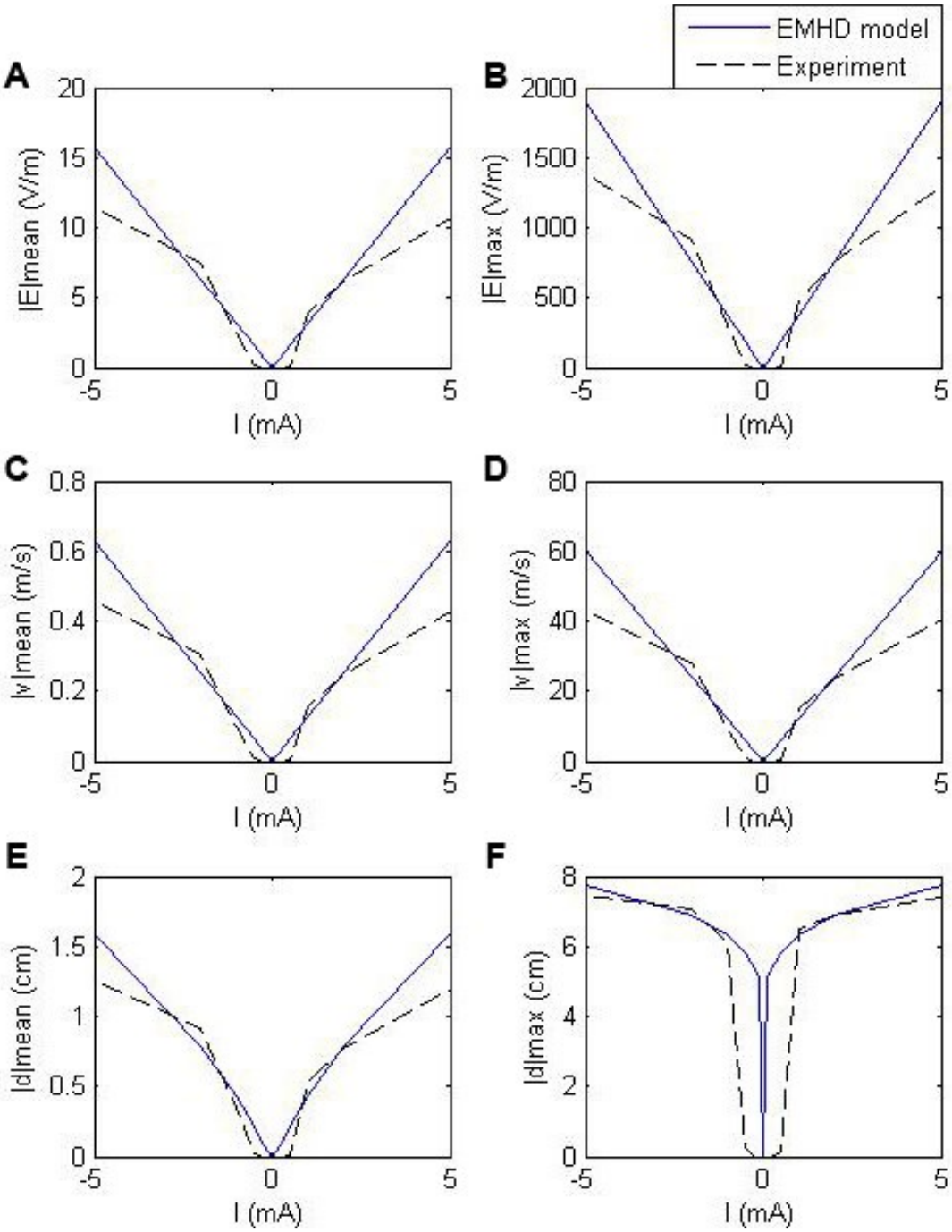

Figure 5.5: EMHD model and LEI experiment predicted electric field, velocity, and displacement magnitudes over a range of currents strengths

Current strengths I = -5, -2, -1, -0.5, -0.2, -0.1, 0, 0.1, 0.2, 0.5, 1, 2, 5 were used in the LEI experiments of the electrolyte phantom and corresponding EMHD model simulations (Figure 3.1). Experiment predicted values are from EMHD model simulations using SRLT inferred |I| from experimental LEI images. Model electric field magnitude (V/m) (**A**) mean and (**B**) maximum and LEI induced flow velocity magnitude (m/s) (**C**) mean and (**D**) maximum are linearly related to the applied current strength. EMHD model displacement (cm) (**E**) mean and (**F**) maximum within the phantom are non-linearly related to current strength, with maximum displacement approaching 8 cm in the 10 cm phantom. EMHD model and experiment predicted values are similar for $|I| \geq 1$ mA.

In Figure 5.5A and Figure 5.5B, the EMHD model reports a linear relationship between the actual applied current strength I with mean and maximal electric field magnitudes for grid points within the phantom. Additionally, the Lorentz force induced velocity mean (Figure 5.5C) and maximum (Figure 5.5D) values also exhibit a linear relationship with the current strength. Mean displacement (Figure 5.5E) on the other hand shows a gradually decreasing rate of increase for higher current strengths, while the maximum displacement (Figure 5.5F) shows a much higher rate of increase for lower current strengths $|I| \leq 1$ mA that quickly decreases for higher current strengths $|I| > 1$ mA.

We also use the EMHD model to study the relationship between the current strength and maximum pressure values within the phantom for the same range of current strengths, shown in Figure 5.6 below.

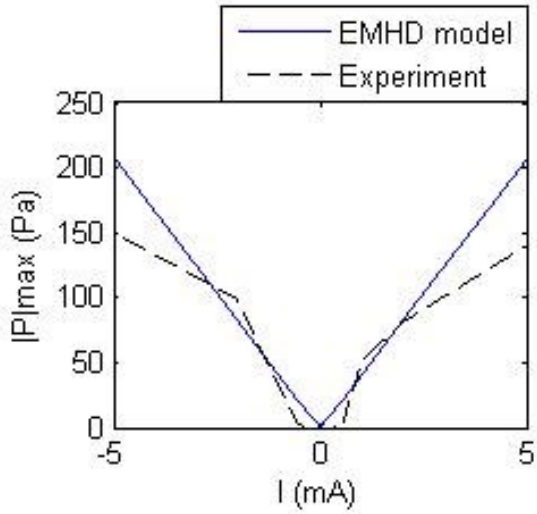

Figure 5.6: EMHD model and LEI experiment predicted pressure magnitude over a range of current strengths
Current strengths I = -5, -2, -1, -0.5, -0.2, -0.1, 0, 0.1, 0.2, 0.5, 1, 2, 5 were used in the LEI experiments of the electrolyte phantom and corresponding EMHD model simulations (Figure 3.1). Experiment predicted values are from EMHD model simulations using SRLT inferred |I| from experimental LEI images. Pressure (Pa) maximum value within the EMHD model phantom is linearly related to the current strength. EMHD model and experiment predicted values are similar for $|I| \geq 1$ mA.

In Figure 5.6 there is a linear relationship between the current strength and the maximum pressure magnitude within the phantom. The maximum pressure occurs in the bottom or top of the phantom for a positive (Figure 4.1D) or negative (Figure 4.2D) current polarity, respectively.

In Figure 5.1C and Figure 5.1D, it was shown that mean S_R was a useful indicator of current strength for low current magnitudes $|I| \leq 1$ mA whereas SRLT was a better indicator of current strength for higher current magnitudes $|I| > 1$ mA. To show the utility of SRLT, we plot the relationship of the electric field strength and fluid dynamics variables with SRLT over the range of current strengths tested and compare the EMHD model and LEI experiment predicted results in the figures below.

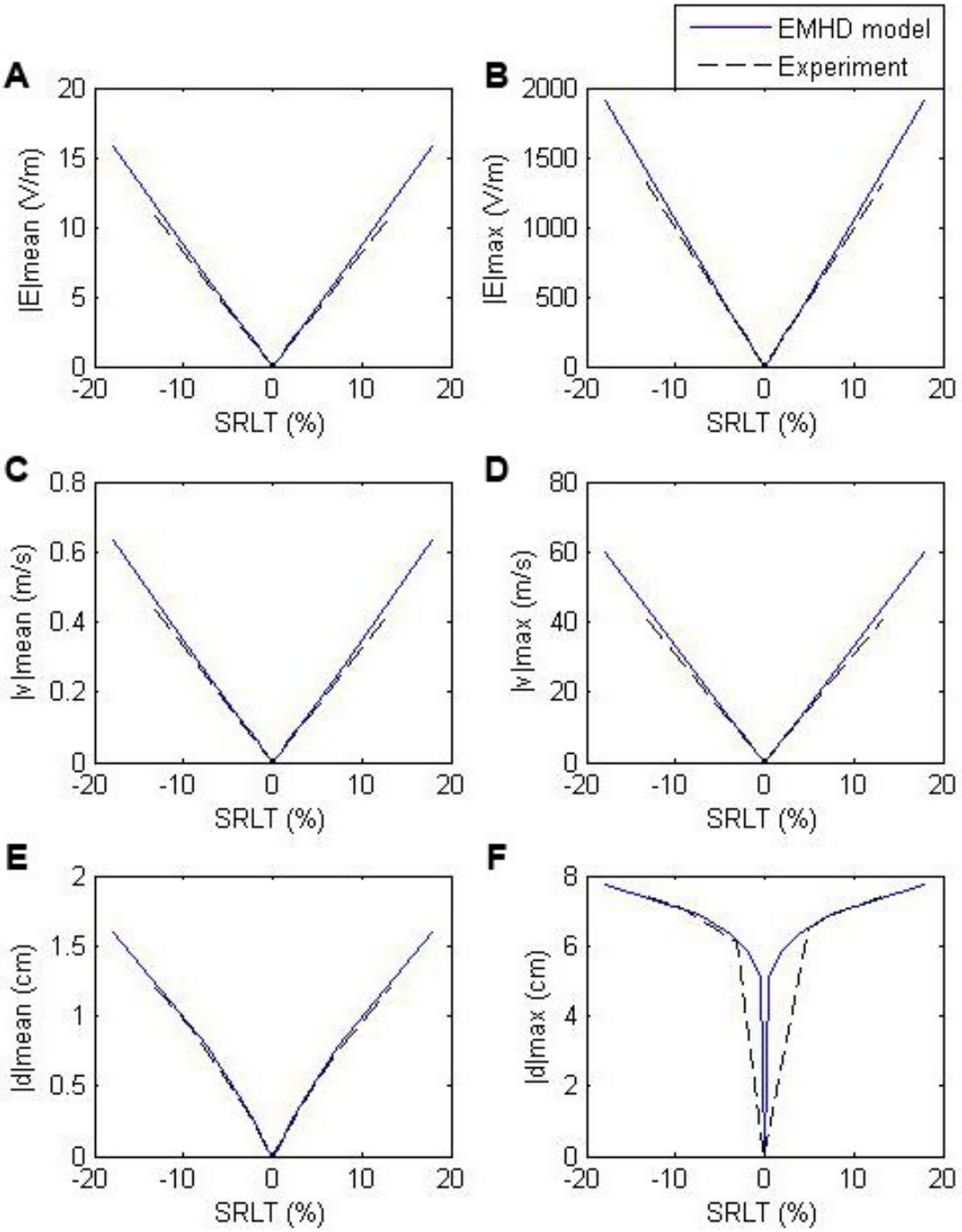

Figure 5.7: EMHD model and LEI experiment predicted electric field, velocity, and displacement magnitudes over a range of currents strengths

Current strengths I = -5, -2, -1, -0.5, -0.2, -0.1, 0, 0.1, 0.2, 0.5, 1, 2, 5 were used in the LEI experiments of the electrolyte phantom and corresponding EMHD model simulations (Figure 3.1) to obtain SRLT from the images. Experiment predicted values are from EMHD model simulations using SRLT inferred |I| from experimental LEI images. Electric field magnitude (V/m) (**A**) mean and (**B**) maximum and LEI induced flow velocity magnitude (m/s) (**C**) mean and (**D**) maximum are linearly related to SRLT. Displacement (cm) (**E**) mean and (**F**) maximum within the phantom are non-linearly related to SRLT, with maximum displacement approaching 8 cm in the 10 cm phantom. EMHD model and experiment predicted values are almost identical.

We similarly plot the relationship between maximum pressure and SRLT and compare the EMHD model and LEI experiment predicted results in the figure below.

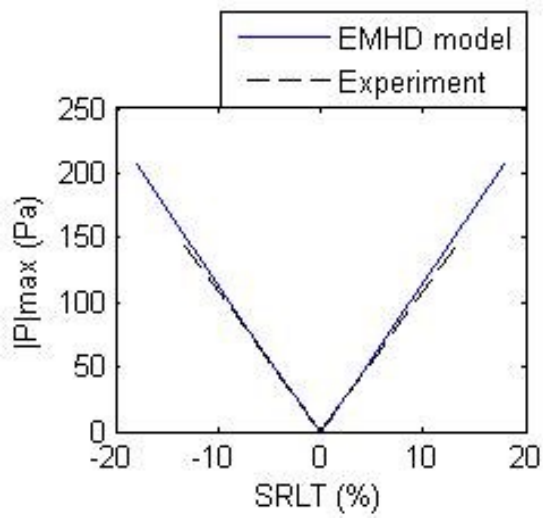

Figure 5.8: EMHD model and LEI experiment predicted pressure magnitude for a range of SRLT

Current strengths I = -5, -2, -1, -0.5, -0.2, -0.1, 0, 0.1, 0.2, 0.5, 1, 2, 5 were used in the LEI experiments of the electrolyte phantom and corresponding EMHD model simulations (Figure 3.1) to obtain SRLT from the images. Pressure (Pa) maximum value within the EMHD model phantom is linearly related to SRLT. EMHD model and experiment predicted values are almost identical.

5.3. Discussion

LEI's demonstrated ability to depict signal loss in the presence of electrical activity in electrolyte solutions is a promising step toward its use as an ncMRI method. In the previous chapter we demonstrated the EMHD model's ability to approximate the magnitude and distribution of the LEI relative signal loss, supporting its applicability as a means to further study LEI contrast. To optimize LEI's use in directly mapping electrical activity we explored the relationship between the relative signal change (S_R) in the images and the underlying current strength magnitude (|I|) in the electrolyte phantom using results from the experiment and EMHD model.

The results showed that the mean S_R (Figure 5.1C) and the percentage of voxels in the phantom with a signal loss below a pre-specified threshold (SRLT, for a threshold of -40%) (Figure 5.1D) in the EMHD model were proportional to |I| and the experiment results were similar except that the mean S_R in the experiment had a slower rate of increase for |I| > 1 mA than in the model. Therefore, SRLT from LEI images can be used as a measure of |I|, which is promising towards the use of LEI to map differences in current density (i.e. quantify the number of active currents in a different areas of the brain). Also, because the model SRLT are similar to those in the experiment we may use future EMHD model simulations to optimize the amount of detectable signal (SRLT) for a given current strength and frequency by varying the LEI protocol, which is promising towards the use of EMHD to determine an optimal LEI protocol for a given current activity (i.e. determine an optimal LEI protocol for ncMRI by using EMHD models of brain currents).

The maximum S_R (Figure 5.1B) in the experiment increased for higher |I|, which may be a source of the higher means in the experiment compared to the model results in Figure 5.1C and reporting only voxels with significant signal loss by computing SRLT, there was better correlation between the experiment and EMHD model results (Figure 5.1D). In the EMHD model, the maximum S_R was uniformly 0% as discussed in the previous chapter due to ignoring flow effects.

The minimum S_R (Figure 5.1A) in the EMHD model was -100% for all non-zero |I| tested, whereas in the experiment the values started above -40% for |I| = 0.1 mA and went below -100% for |I| ≥ 2 mA. The S_R values less than -100% in the experiment can be explained based on Eq. 4.1 used to compute S_R for the experimental difference images. For $S > S_0$, such as from flow effects in the experiment, S_R will be positive (showing a relative signal gain). For $S < S_0$, S_R will be negative (showing a relative signal loss). For S approaching zero, which is more likely to happen at higher |I|, and $S_0 > S_m$, S_R will be less than -100% as seen in the experiment results in Figure 5.1A.

Trends in the proportion of the total S_R distribution (SRP) in the top (Figure 5.2A) and bottom (Figure 5.2B) half of the phantom for varying |I| can be used to quantify the top-bottom asymmetry of S_R seen in the previous chapter. Based on SRP, the distribution of signal change was higher in the top half of the phantom for negative |I| and higher in the bottom half for positive |I|. These trends also follow the Lorentz effect as discussed in the previous chapter and can be seen depicted in the model (Figure 4.1A, Figure 4.2A) and experiment images (Figure 4.1B, Figure 4.2B) for |I| ≥ 0.5 mA (see [42] for experiment images over the full range of current strengths). There was some correlation

between SRP trends in top and bottom half of the model and experiment, and the trends themselves were not directly related to or useful predictors of |I|.

SRP computed in the left (Figure 5.2C) and right (Figure 5.2D) halves of the phantom for varying |I| was equal in the EMHD model, showing left-right symmetry. In the experiment however, SRP showed left-right asymmetry for all |I| > 0, which was not readily apparent in the experiment images (Figure 4.1B, Figure 4.2B, Figure 4.3B) before quantifying S_R. The distribution of S_R was higher in the left half of the phantom for negative |I| and higher in the right half of the phantom for positive |I|. As a trend across all |I|, this asymmetry can be from systematic error in the experimental or image analysis methods, or from another force not represented in the EMHD model.

One possible source of error in the experimental methods could be if the axis along the phantom electrodes was not aligned exactly perpendicular to the direction of the scanner's magnetic field. Misalignment would create a left-right component to the Lorentz force that reverses with the current polarity and could explain these results. Another possible source of error from image analysis could be if the phantom were not perfectly centered in the field of view the central 10-cm diameter circle used to extract the experiment images for analysis, which would shift the distribution of S_R. However, this error would be less likely than electrode misalignment to cause a trend that is reversible with current polarity. Lastly, it is possible that another force affecting particle motion or a source of signal that was unaccounted for in the EMHD model (i.e. flow effects) may affect the distribution of S_R in the left-right direction and reverse with

current polarity. Further study under different experimental conditions is required to determine the significance of these potential sources of error.

By performing quantification of S_R in each half of the phantom, SRLT showed a linear dependence on |I| for the top, bottom, left, and right halves of the EMHD model image (Figure 5.3). Similar to SRP, SRLT can quantify the vertical asymmetry but has a more linear relationship to the underlying current strength. In addition, SRLT can be used to predict |I| from the experiment images using a linear trend that is obtainable through EMHD model simulation. SRLT in the top and bottom halves of the experiment showed good correlation with the EMHD model trends, whereas there was some left-right asymmetry in the experiment SRLT at some of the |I| tested but less than the asymmetry observed using SRP (Figure 5.2).

To better understand EMHD and LEI contrast, we also analyzed the current strength dependence of other parameters in the EMHD model not readily available from the experimental phantom that underlie the LEI contrast mechanism. A linear trend existed for the mean (Figure 5.5A) and maximum (Figure 5.5B) magnitude of the electric field strength |E|, the mean (Figure 5.5C) and maximum (Figure 5.5D) magnitude of the Lorentz force induced flow velocity |*v*| (Figure 5.5), and the maximum magnitude of pressure P (Figure 5.6) in the phantom, allowing prediction of these parameters based on experimentally derived |I| (I_E). Therefore, in LEI experiments we can use the value of I_E predicted from measuring SRLT in the experiment image to directly infer the magnitude of the underlying |E|, |v|, and |P| in the phantom.

To infer the magnitude of mean (Figure 5.5E) and maximum (Figure 5.5F) displacement, a corresponding EMHD model simulation with an applied current strength of I_E from the experiment can be performed. Accuracy of the displacement magnitudes computed using the EMHD model can be verified experimentally by using the same electrolyte phantom in an MRI protocol setup to image the Lorentz force induced displacement [47], as described in section 1.3, which may be used to detect displacements on the order of 0.1 μm. However, incoherent displacement of water in the electrolyte solution differs from oscillatory motion in an elastic medium. Therefore, the applicability of MRE in measuring current-induced displacements under an MRI magnetic field in the electrolyte phantom or in the brain is still unknown.

In conclusion, computing SRLT from LEI images in experiments provides a means to quantify the underlying current strength. Therefore, in addition to detecting the presence of electrical activity, LEI can be used to quantify differences in current density. Thus, if an LEI protocol is developed that detects currents in the brain it may also be used to differentiate areas of high (more neuronal current density) and low (fewer neuronal current density) activity, which is useful for brain mapping. To determine an optimal LEI protocol for detecting a given current activity, future EMHD model simulations may be used to determine the optimal oscillating gradient parameters for maximizing SRLT. The EMHD model also provides additional information to better understand LEI, which is useful in determining the detectability of LEI in other settings. For example, if fluid displacement in the brain is limited to a certain range due to structural constraints,

approximating the scale of S_R for that range of displacement based on EMHD would help predict the feasibility of LEI in the brain.

The success of LEI in detecting current in phantoms [40-42] and the human median nerve *in vivo* [16] is promising toward its use as an ncMRI method. And the ability for EMHD and LEI experiment images to infer current and electric field strength, flow velocity, and pressure in the electrolyte phantom provides a better understanding of LEI in that setting. However, the cortex is vastly different from the electrolyte phantom due to smaller dipole lengths, higher current source density with lower strengths, and varying source firing rates. Further study using modifications in the EMHD model can be performed to determine the effect of these differences on the LEI signal detected, and how to best optimize LEI for use in cortex. There are also facets of the cortex that may be more difficult to represent in the EMHD model and require more careful consideration, which will be discussed in the next chapter.

6. Conclusions and future work

We described the benefit of using MRI to directly map neuroelectrical activity and achieve a higher correlation and temporal resolution than functional MRI, a field of study referred to as neuronal current MRI (ncMRI) [1]. Lorentz effect imaging (LEI) is an MRI technique that employs oscillating magnetic gradients synchronized to underlying current activity to achieve a signal loss corresponding to electrical activity. LEI has shown promise as a potential ncMRI method by successfully detecting electrical activity in various phantoms [40-42] and in the human median nerve *in vivo* [16], but its underlying contrast mechanism has not been well understood.

6.1. Summary of EMHD in LEI

To better understand LEI contrast, we compared various interpretations of the Lorentz force to explain the electrolyte phantom LEI experiment results by Truong et al. [42]. Based on each interpretation, we performed computational simulations of the electrolyte phantom and studied dynamics of the induced velocity, particle displacement, and relative signal changes that each model generated. It was shown that only electromagnetohydrodynamics (EMHD) successfully predicted the areas of signal loss seen in the experiments.

We also found that the EMHD model demonstrated the same distribution, reversibility, and scalability of LEI signal loss as in the experiment under the highest current strength (5 mA), the opposite polarity current (-5 mA), and a smaller current (0.5

mA) tested, respectively. The EMHD model also provided maps of the electric field, velocity, displacement, and pressure that were not readily available in the experiment, which aided in the understanding of the underlying fluid dynamics and the LEI contrast mechanism. A summary of the Lorentz effect and the EMHD model and experiment signal images for these three currents are shown in the figure below.

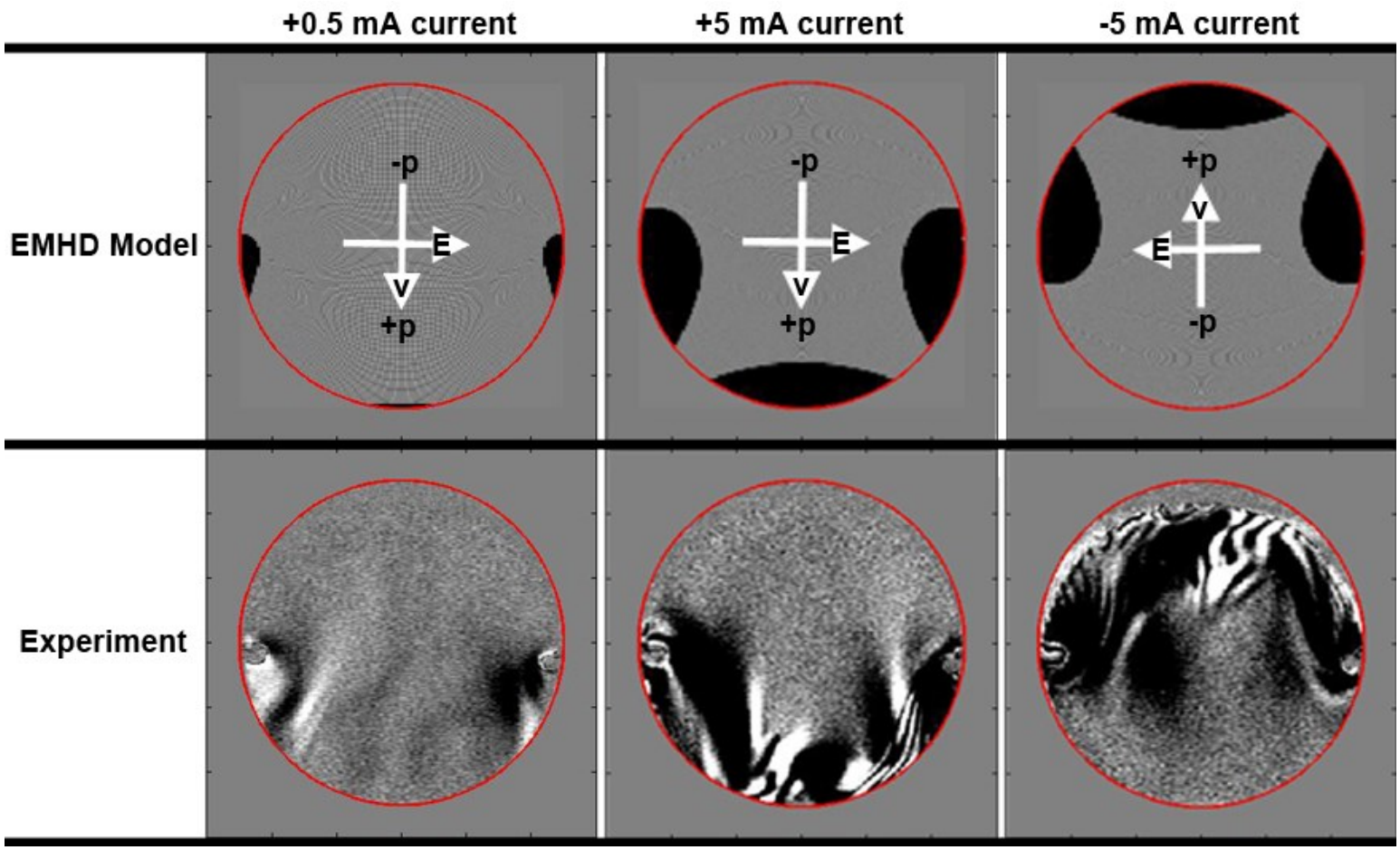

Figure 6.1: Summary of EMHD model and LEI experiment results in an electrolyte phantom
E = electric field direction, v = Lorentz-force-induced flow velocity, p = pressure.

We also studied the resulting LEI signal change magnitude (S_R) using the full range of current strengths |I| from the phantom experiments, and found that the percentage of voxels in the phantom with signal change below a prespecified threshold of -40% (SRLT) had a linear relationship with |I| and can therefore be used as a direct and accurate measure of |I| in LEI experiments. There was also a correlation between the linear trends of SRLT with |I| in the model and experiment for the phantom as a whole and the top, bottom, left, and right halves of the phantom, making SRLT and appropriate quantifiable measure to compare future model and experiment results. These trends allow for the EMHD model to predict the magnitude and asymmetry of S_R in an LEI phantom experiment based on a given current strength and polarity and vice versa, they allow for an LEI experiment to measure the underlying current strength and polarity based on the magnitude and asymmetry of SRLT. Additionally, the magnitude of the underlying electric field, flow velocity, displacement, and pressure can be inferred from the LEI experiment images by computing |I| from the images and performing a corresponding EMHD model simulation.

6.2. Future methods to improve model accuracy

Future studies can be performed to improve the assumptions or address the shortcomings of the modeling and analysis methods presented in this work. There are also other factors to consider when pursuing future study of EMHD and LEI in cortex.

6.2.1. Computational phantom model

In this work, we used a square phantom domain with results outside of a central circle that were clipped to approximate the central slice of a spherical electrolyte phantom. A more accurate representation of the phantom results using EMHD may have been achieved by modeling a circular phantom domain. Using a finite element method with triangular elements would allow for more accurate representation of the circular shape [66]. Optimally, a three dimensional phantom model can be developed for future study. For example, a three dimensional model would allow for computing the error associated with misalignment of the phantom electrode axis with the MRI scanner's magnetic field, as discussed in section 5.3.

In the future, a more elegant and general means of constructing the EMHD model for applicability to *in vivo* experiments can be performed by taking a standard MRI image of the area of interest, thereby providing volumetric information on the object as well as highlighting water composition. Different tissue compositions can also be identified and assigned different conductivity values. This information can then be used to construct the three-dimensional EMHD model in a modeling software package like COMSOL, in which the EMHD equations described in this work can be applied to perform simulations of the fluid dynamics and compute the resulting LEI image.

The results of the EMHD model were verified based on the images of the relative signal change. These results were produced based on simulation of an MRI acquisition

6.2.2. Flow effects

Signal gain were shown in the experiment images in Chapter 3, and are due to flow effects [42]. Based on Figure 5.1B, it was also shown that signal gains and signal losses scaled similarly with |I| in the experiment. Therefore LEI signal gain is not a background phenomenon independent of the LEI protocol and its underlying mechanism requires further study through experimentation.

Furthermore, it may be useful to incorporate signal gain in the LEI measurement of current strength because of its similar response to |I| as the signal loss. Therefore, we can perform future analysis of the model and experiment results and compare the dependence on |I| of the mean signal loss (mean S_R for voxels with $S_R < 0$), mean signal gain (mean S_R for voxels with $S_R > 0$), and the mean S_R for all voxels (Figure 5.1C), and compare the trends seen between these measures and |I|. Quantifying the correlation of these trends in the experiment results with those of the model results would also be useful in determining which measure of signal loss better follows EMHD theory, and if the flow effects are contributed to by the Lorentz force and fluid dynamics in the phantom.

6.2.3. Noise and SNR

As in any imaging modality, noise and other effects play a role in the signal to noise ratio (SNR) and image contrast. Future computational EMHD models can incorporate methods for more realistic simulation of MRI image acquisition to help study the effect of noise on S_R and the detectability of the LEI contrast in other settings. Models

already exist to simulate the MRI image generation process that incorporate noise and partial volume effects [67].

Based on an analysis of the SNR, it was shown that the noise generated by a cylindrical object imaged using MRI (such as the body) is proportional to the square of the radius and the square root of the length [68]. Hence, noise in the phantom would is dependent on the phantom size. It would also be useful to determine if there is a component of noise in the phantom experiments that is dependent upon the electrical current strength.

6.3. Future EMHD model studies of LEI in the brain

In this section we discuss potential EMHD model simulations that will aid in studying and optimizing the utility of LEI as an ncMRI method for mapping neuroelectrical activity in human cortex. In traditional neuroimaging, a high resolution MRI slice may have voxel sizes as small as 1-2 mm squared. Therefore, to initially determine LEI signal detectability in the cortex, a single voxel with dimensions on the order of millimeters can be studied in the active (current on) and inactive state (current off) using gradient oscillations that are synchronized to the frequency of the underlying activity. In this section we propose EMHD model simulations for a single 1.5 mm x 1.5 mm square voxel of cortex.

6.3.1. Shorter dipole length

Current sources in the cortex have a much smaller dipole length (1-5 mm [2]) than that of the experiments in Chapter 4 (10 cm). To test the effect of smaller dipole length on the detectability of the LEI signal, we approximate an action potential or post-synaptic potential by placing two point sources of current with opposite polarities spaced 1-5 mm apart, based on the approximate length of an action potential traveling along an axon [2]. These point sources may be added as Dirichlet boundary conditions at either end of the voxel similar to simulations performed in the previous chapter but with domain sizes on the order of millimeters. In initial simulations, the point sources can be assumed to have a fixed position, with strengths alternating between an on-value or zero, allowing the electric field map to be computed once. The on-current (active) state electric field map can be alternated with a uniformly zero electric field for off-states. These assumptions simulate a neuroelectric dipole fixed along a membrane. Despite this major assumption, the effect of the neuroelectrical dipole length on EMHD will be well approximated in these simulations.

To quantify the effect of dipole length on the LEI contrast, mean relative signal changes or SRLT can be reported and studied over a range of dipole lengths. To obtain these results, EMHD model simulations can be performed using progressively smaller square domain sizes matching the dipole lengths simulated (5 mm to 1 mm in 0.5 mm increments) with the current sources placed at the left and right ends of the model domain as in Figure 2.2. In the case of cortex, the conductivity will be also be different: $\sigma = 0.333 - 2.06$ S/m [69], as opposed to $\sigma = 140$ S/m in the electrolyte phantom.

6.3.2. Higher density and smaller strength of current sources

Another difference that must be studied for using LEI in cortex compared to the phantom is the higher density of current sources (9 regular spaced dendritic currents per 15 x 15 x 100 μm voxel from SQUID MEG recordings of current density in active cortex [39], compared to one dipole source in the 10 x 10 x 10 cm phantom) with smaller current strengths (1 - 10 nA neuronal currents [2], compared to 0.5 - 5 mA currents simulated in the phantom in Chapter 4). EMHD model simulations can be performed with multiple current sources inside the 1.5 mm x 1.5 mm square cortex voxel to approximate the density of electrically active dendrites and axons in a given portion of active cortex. Unlike the phantom experiments in the previous chapter which had multiple voxels within a single dipole field, these simulations explore the effect of multiple dipole fields within a single voxel. To approximate an active portion of cortex (with 10^5 pyramidal cells / mm^2 and 1000 synapses per neuron [39]) the cortex voxel electric field can be computed using a large number of neuroelectric current sources. As opposed to using dipoles spaced millimeters apart to approximate an axonal action potential or dendritic post synaptic potential, we may alternate by placing positive and negative polarity current sources in the cortex domain to study the effect of a higher distribution of sources with opposing polarity on the EMHD dynamics and LEI signal detectability.

Multiple point sources may be added as Dirichlet boundary conditions in the EMHD model stiffness matrix used to solve the Poisson equation for computing the electric field from the current sources. In initial simulations, each source can be assumed

to have a fixed position, with all current source strengths simultaneously alternating between a specified on-value and zero, allowing the electric field map to be computed once. The on-current (active) state electric field map can be alternated with a uniformly zero electric field for off-states to compute the Lorentz force at each time step. These assumptions simulate numerous sources with current strength similar to neuroelectric potentials fixed in space exhibiting synchronous activity, allowing for simpler study of the effect of multiple small current sources on LEI signal detectability. The effect of asynchronous activity on the EMHD dynamics and LEI contrast may also be explored in future simulations by introducing varying levels of current source synchronization.

To model the multiple current sources, we can discretize the 1.5 mm x 1.5 mm cortex voxel into grid points spaced 1.5 μm apart in the x and y dimensions (1000 x 1000 grid points, as opposed to the 512 x 512 grid points used in the previous chapter simulations). Based on a current source density estimate [39], we can regularly space current sources at every third grid point in either dimension for a slice thickness of 100 μm. For a slice thickness of 5 mm as in the previous chapter simulations, more current sources can be used, forming a finer grid resolution (5000 x 5000 grid points spaced 0.3 μm apart in the x and y dimensions). Also, the current source strengths can be on the order of those generated by cortical axons and dendrites (1-10 nA [2]) to better estimate the sensitivity of LEI for imaging neuronal currents in the human cortex.

6.3.3. Varying firing rates and gradient widths

Further study is also warranted to explore optimization of LEI for varying firing rates in cortex by changing aspects of the LEI protocol (e.g., the frequency of the oscillating gradients, which must be synchronized to the neuronal currents of interest) to optimize its use as an ncMRI method. The effect of asynchronous currents on the LEI contrast mechanism is not well understood and can be studied using the EMHD model to optimize LEI in this setting. As an example, visual stimuli cause synchronous firing of neurons in the lateral geniculate nucleus (LGN) of the thalamus, which generate action potentials along axons terminating on dendritic processes in the occipital cortex [11, 70]. At the same time, other current frequencies may exist, such as those from the interneurons with electrotonic activity along their dendrites or action potentials along their axons in the same voxel of cortex.

To study the use of LEI in the occipital cortex, varying patterns of activity can be modeled and their effect on EMHD and the LEI relative signal changes can be determined. Typical LGN axon firing rates and activity from downstream dendrites due to visual stimuli are on the order of 20 - 50 Hz [70], which correspond to activity periods of 20 - 50 msecs. In this example, oscillating gradient periods of a similar period would optimize LEI detection of LGN-related activity. For interneuron axonal or dendritic activity occurring at half the rate (10 - 25 Hz) and after a brief delay, using oscillating gradient periods tuned to the LGN activity will be at half the period of the interneuron firing rate, potentially canceling out the phase shift (ϕ_R) accumulated from some of the interneuron activity. As opposed to using oscillating gradient lobe widths of 20 - 50

msecs, using 40 - 100 msecs will optimize detection of these interneuron currents but will allow LGN axon spikes to occur equally during the positive and negative gradient lobes, thereby cancelling out any phase shift accumulated from LGN activity. To maximize ϕ_R and the LEI signal loss generated by all current sources in the cortex related to the visual-evoked response, oscillating gradient periods must be optimized to both of these firing patterns.

To add more firing variation and stochastically synchronized activity, a mechanistic model of LGN firing [71] can be used for each LGN current source simulated in the cortex voxel. Similarly, various models can be used to represent activity of the interneurons or other cortical current sources. Therefore, using the EMHD model to study the dependence of LEI signal loss on the oscillating gradient period in the setting of multiple cell line firing patterns will be useful in optimizing an LEI protocol for detecting cortical activity.

6.3.4. Restricted spaces

One facet of LEI in the cortex that requires more careful consideration to represent in an EMHD model is the effect of restricted spaces on the fluid dynamics. Restricted spaces refer to microscopic compartments of intra and extracellular conducting fluid between which water molecules may not travel freely due to the presence of cell membranes, cell junctions, extracellular matrix, and cytoskeletal elements in neuronal tissue. Accounting for the effect of restricted spaces in the model may be simple and

require use of a correction factor, an additional term in the velocity update steps, or a different set of fluid dynamics equations. Or it may be more complicated and require use of a three-dimensional bioelectric model of the cortex to compute the electric field, followed by separate computations of fluid dynamics water particle phase shift accumulation in the intra- and extracellular spaces before integrating signal contributions from the intra- and extracellular water molecules within each voxel.

A future experiment may be warranted to study the fluid dynamics in cortical gray matter and determine what modifications to the fluid dynamics equations (Eq. 2.9) or the parameter values may be required to accurately model water motion in the cortex. We first estimate the diffusion and convection of water in the extracellular space of cortical gray matter based on a literature review to assess the effect of restricted spaces on water motion under baseline physiologic conditions.

Brain tissue density is approximately 1.04 g/ml, which represents a volume per weight of 0.96 ml / g of brain [72]. Next, the mean water content of normal gray matter in adult Wistar rats is 76.9 +/- 1.4% (SD), 88.9% of total tissue water is free whereas 11.1 +/- 2.8% (SD) is bound (to extracellular matrix proteins and other large molecules) [73]. A standard value for the volume fraction of extracellular fluid (ECF) in the brain is estimated at 20% (ranging from 15%-30%) [74]. Hence, roughly 20% x 88.9% = 17.8% of total gray matter is ECF free water by volume, and 17.8% x 0.96 ml/g = 0.17 ml / g of brain tissue is occupied by ECF free water. It was measured that fluid convection occurs in the interstitial fluid of rat brain at a rate of 0.11 μl / g brain / min [75]. Based on the ECF free water volume per gram of brain, this means that only ~ 0.1 % of the total ECF

free water that is moved by convection per minute, which is far less than the fluid fraction moved by convection in the electrolyte phantom. Also, this ECF fluid convection is restricted to the perivascular spaces surrounding capillaries [75], thereby making the routes for bulk fluid flow in the ECF narrow and less random than the organization of neuronal processes in the cortex.

The limited amount of the ECF free water fraction moving through bulk flow must do so through narrow channels ~ 20 nm in mean width that are tortuous, thereby hindering velocity [74]. Measurements of bulk flow velocity in the white matter are 10.5 μm/min, whereas in gray matter bulk fluid flow only occur under osmotic stress (no measureable flow velocity otherwise) at a velocity of ~ 3 μm/min [76], far less than mean velocity in the electrolyte phantom (5.2 cm/s from Table 3.2). Therefore, the feasibility of LEI to measure bulk water flow in the ECF is unclear, and would require a computational model (modified fluid dynamics equations accounting for tortuosity and restricted spaces [74]) or an experimental (radiotracer injection or iontophoresis [74]) model in a section of cortex, to estimate flow velocities and displacements under the LEI protocol. EMHD model simulation can be used to study LEI feasibility by adjusting |I| to recreate the experimentally measured flow velocities and displacement magnitudes and estimate the mean S_R and SRLT achieved in the ECF for a given LEI pulse sequence. Due to the large proportion of intracellular fluid (ICF) in cortex (~75%) [74], a similar analysis of the LEI signal change achievable in the ICF is also warranted.

6.4. Discussion

The ability for LEI images to also infer current strength, electric field strength, flow velocity, and pressure in the electrolyte phantom provides additional benefit to LEI mapping. However, the cerebral cortex is vastly different from the electrolyte phantom due to the smaller dipole lengths, higher current source density with lower strengths, and varying source firing rates. EMHD model modifications to account for these differences were discussed in sections 6.3.1, 6.3.2, and 6.3.3, respectively. Further simulation using these EMHD model modifications can be performed to approximate the LEI signal change due to activity in the cortex and how to optimize an LEI protocol for mapping experiments in the brain.

Appendix: MATLAB function code m-files

MHD_Square.m

```
function MHD_Square(method, runopt, varload, outputfile,
varargin)
% function MHD_Square(method, runopt, varload, outputfile,
% varargin)
% Created By: Navid Pourtaheri
% Last updated 3/12/2013
%
% Uses a modified version of the Navier-Stokes SIMPLE
% Method to compute velocities of particles due to the
% Lorentz force under electromagnetic fields in a square
% domain of electrolyte
% capable of varying the order of operations in
% computing particle velocity updates
%
% Computes particle displacement and phase shifts based on
% the Particle tracking method and Reynold’s Transport
% method
%
% Simulates MRI image generation from the Lorentz Effect
% Imaging protocol
%
% method 0: testrun (default)
% Other options not used in final sims, replaced by FTT
%
% Order of operation methods for velocity update
% FTT == 0, Separate force then convection update
% FTT == 1, Combined convection + force update
% FTT == 2, Separate force after convection update
% FTT == 3, Separate force after implicit viscosity
% FTT == 4, Separate force after pressure update
%
% runopt: used to determine output style (default = 2)
% No longer used in final sims, Replaced by I = runopt
% runopt 0, (save only) no display (text and signal plot
% saved)
% runopt 1, display text only (save signal plot, others not
% shown)
% runopt 2, (show only) display all text and plots, no text
```

```
% or plots saved
% runopt 3, display all text and plots, save signal plot
% runopt 4, (show & save) display all text & plots, save
% text & signal plot
%
% varload: parameter values may be loaded from varload.mat
% to overwrite
% any default value
% outputfile: where final workspace output(s) will be saved
% varargin: variables to save in outputfile (optional,
% default = all)
% ------------------------------------------------------------
% testrun = 0: uses stored or assigned space - time
% variables
% testrun = 1: overrides all space - time variables for
% default simulation

% Use tic to report predicted and final simulation run time
tic

% handle file i/o inputs, create display file for runopt
if nargin < 1, method = 1; end
if nargin < 2, runopt = 5e-3; end
if nargin < 3, varload = 'MHD_input'; end
if nargin < 4, outputfile = 'MHD_output'; end
if nargin > 4, savevars = varargin; else savevars = ''; end
numvars = length(savevars);

I = runopt;
disp(['I = ' num2str(I*1000) ' mA']);
FTT = method;
disp(['FTT = ' num2str(FTT)]);

if isempty(outputfile)
    outputfile = 'MHD_output';
end
outputfile = [outputfile '_I' num2str(I*1000)];
displayfile = [outputfile '_display'];
plotfile = [outputfile '_plot'];

% Server directory switching, server = 0 runs in current
% directory
server = 0;
```

```
% Other simulation options: on = 1, off = 0 (default)
bounce = 0;     % Bounce method (no longer used in final
sims)
PTT = 1;        % Particle tracking method
Vmulti = 0;     % Plot velocity update images for first
time step then quit
timedep = 1;    % Plot time dependent dynamics
plotextra = 0;  % Additional plots of the EMHD model
parameter space
upwind = 1;     % upwinding in N-S SIMPLE method, default =
                % 1 in final sims

% testrun
if method == 0
    method = 2; runopt = 4; testrun = 1;
    disp('*******************************');
    disp('*** Test Running MHD_Square ***');
    disp('*******************************');
    PTT = 1; Vmulti = 0;
else
    testrun = 0;
end

% Check current path. If in code dir, switch to default
% output dir
outputpath = pwd;
if server
    if length(outputpath) < 24
        outputpath = '/nefs/np2/MATLAB_OUTPUT/MHD';
    end
    if outputpath(1:23) ~= '/nefs/np2/MATLAB_OUTPUT'
        outputpath = '/nefs/np2/MATLAB_OUTPUT/MHD';
    end
    if ~exist(outputpath,'dir')
        mkdir(outputpath);
    end
end

% % use runopt to determine output style
fid = fopen([displayfile '.txt'],'wt');
disp(['display text saved to: ' displayfile]);
diary([displayfile '.txt']); diary on;

% update Phi based on qo
```

```
qupdate = 0;

% Switch to run directory for saving outputfiles
cd(outputpath);
fprintf(fid, '%s\n', ['working directory: ' pwd]);
if server
    addpath('/nefs/np2/MATLAB_CODE');
end

% Option to draw circle delineating phantom
drawcirc = 1;

%% Parameter Space
% Set default values
% Physical Parameters
Bz = 4;     % magnetic field strength (T)
% I = 5e-3; % current pulse magnitude (A)
Tp = 2e-3;  % current pulse width (s)
R = 1e3;    % phantom resistance (Ohm)
d = 10e-2;  % phantom diameter (m)
lx = d; ly = d;
V = I*R;    % inter-electrode voltage (V)
PhiW = V/2;
PhiE = -V/2;
sig = 140;  % electrical conductivity of fluid (S/m)
um = -9e-6; % magnetic permeability of the fluid (H/m =
            % Ohm*s/m)
eo = 8.854e-12; % permitivity of free space
er = 80.1;      % relative permitivity of water at 20oC
q = 1.602E-19;  % elementary charge in C
avo = 6.022e23; % Avogadros number of elementary charges
                % per mol of ion
pc = 2.8;       % density/concentration solute g/l (Kg/m3)
MOL = 249.70;   % molecular mass of hydrated CuSO4 g/mol
qom = pc/MOL*avo*q*1e3;  % C/m3 maximum charge density

% Navier-Stokes parameters
pw = 998.2;     % density of water (kg/m3)
pf = 1001;      % density of fluid (kg/m3)
eta =  1e-3;    % dynamic (static) viscosity of water at 20
                % oC m2/s

% MRI parameters
Gx = 36e-3;     % x-gradient magnitude (T/m)
```

```
Gy = 36e-3;      % y-gradient magnitude (T/m)
Tg = Tp;         % gradient lobe width
ngo = 15;        % number of gradient oscillations
g = 2*pi*42.576e6;  % gyromagnetic ratio for H1 (rad/s/T)
DZ = 5e-3;          % MRI slice thickness
MAT = [128,128];    % MRI acquisition matrix size [# rows,
                    % # cols]
FOV = [d,d];        % MRI Field of View (m)

% Simulation / Visualization Parameters
nt = 1000;                % default = 1000, number of time
                          % steps per pulse lobe
nsteps = round(nt/10)     % number of steps between
                          % visualization refresh

DX = FOV(2)/MAT(2); % voxel size along x (m)
DY = FOV(1)/MAT(1); % voxel size along y (m)

% Overwrite parameter values from .mat
if isempty(varload) || ~exist([varload '.mat'], 'file')
    varload = 'MHD_input';
else
    load(varload);
    fprintf(fid, '%s\n', ...
     ['paramaters loaded from: ' varload '.mat']);
end

% set gradient lobe width to equal current pulse width
Tg = Tp;

% Vary order of update for Navier Stokes equations
if PTT
    fprintf(fid,'%s\n', 'Particle Tracking Method');
else
    fprintf(fid,'%s\n', 'Reynold''s Transport Theorem');
end
if FTT == 0
    fprintf(fid,'%s\n', ...
    'Separate force then convection update');
end
if FTT == 1
    fprintf(fid,'%s\n', ...
    'Combined convection + force update');
end
```

```
if FTT == 2
    fprintf(fid,'%s\n', ...
    'Separate force after convection update');
end
if FTT == 3
    fprintf(fid,'%s\n', ...
    'Separate force after implicit viscosity');
end
if FTT == 4
    fprintf(fid,'%s\n', ...
    'Separate force after pressure update');
end

%% Allocate remaining variables based on set parameters
% force FD grid to be uniform square grid based on nscale *
% MAT resolution
nscale = 4;
MAT2 = round(nscale*FOV./min(FOV./MAT));
nx = MAT2(1); ny = MAT2(2);
% simulate full pulse-gradient sequence
t = 0;
tmax = 2*ngo*Tp;
ndt = 2*ngo*nt;

% allocate other variables
dt = tmax/ndt;      % time step size (sec)
tt = zeros(ndt+1,1);
vv = tt; vm = tt; vl = tt;
dd = tt; dm = tt; dl = tt;
pp = tt; pm = tt; pl = tt;

% % vars for phase approximation methods from Song (not
% used in final sims)
% ppna = zeros(2*ngo+1); pana = ppna;
% ppnb = ppna; panb = ppna;

% Approximate magnetic damping time
Td = 1/(sig*Bz^2/pf); % (sec)
fprintf(fid, '%s\n', ['magnetic damping time: ', ...
     num2str(Td) ' sec']);

% Set other equation coefficients
Re = 1/eta;
Cp = dt/pf;
```

```
Cf = dt/pf;
Cb = 1;

% Compute diffusion weighting
D = 1e-9;                   % diffusion coeff for water
b = 2/3*ngo*g^2*Gx^2*Tg^3; % diffusion weighting factor
                            % (s/m^2)
dw = exp(-b*D);             % diffusion weighting

% Save all runtime parameters to .txt file, display
% relevant ones
fprintf(fid, '%s\n', ['input file: ' varload]);
fprintf(fid, '%s\n', ['output file: ' outputfile]);
fprintf(fid, '%s%6.4e%s%6.4e%s%6.4e%s%3.1f\n', 'pf = ', ...
     pf, '; eta = ', eta, '; Re = ', Re, '; ngo = ', ngo);
save([varload '_run.mat']);
fprintf(fid, '%s\n', ['run parameters saved to: ', ...
     varload '_run.mat']);

%% Simulate water displacement during each current pulse /
% gradient lobe
% Voxel grid variables, center points for each voxel
xl = [-FOV(1)/2:DX:(FOV(1)/2-DX)] + DX/2;
yl = [-FOV(2)/2:DY:(FOV(2)/2-DY)] + DY/2;
[XX,YY] = meshgrid(xl,yl);
[nr,nc] = size(XX);
NV = nr*nc;           % number of voxel elements

% Navier-stokes grid variables
x = linspace(-d/2,d/2,nx+1); dx = d/nx;
y = linspace(-d/2,d/2,ny+1); dy = d/ny;
[X,Y] = meshgrid(x,y);
Vm = zeros(size(X)); VFx = Vm; VFy = Vm; DM = Vm; VM = Vm;

% initial velocities
vx = zeros(ny,nx-1);  % (m/s) velocity (90x89), off x, on y
vy = zeros(ny-1,nx);  % (m/s) velocity (89x90), on x, off y

% boundary conditions
uN = x*0+0e-1; vN = avg(x)*0;
uS = x*0+0;    vS = avg(x)*0;
uW = avg(y)*0+0e-2; vW = y*0;
uE = avg(y)*0; vE = y*0;
```

```
% Water proton grid variables
if PTT
    wscale = 2; % if testrun, wscale = 1; end
else
    wscale = 1;
end
nwc = wscale;  % number of water molecules per NS column,
default = 4
nwr = wscale;  % number of water molecules per NS row,
default    = 4

[xw,yw] = meshgrid([-d/2:dx/nwc:(d/2-dx/nwc)]+dx/nwc/2, ...
                   [-d/2:dy/nwr:(d/2-dy/nwr)]+dy/nwr/2);
ph = zeros(size(xw));
xc = xw; yc = yw;

if PTT
    % set current locations
    xi = xw; yi = yw;
    XI = xw; YI = yw;
else
    phdx = ph; phdy = ph;
end
nw = numel(xw);

% store original pulse-gradient values
Vo = 1;     % 1 = pulse on
Gxo = Gx;
Gyo = Gy;
V = I*R;    % inter-electrode voltage (V)
PhiW = V/2; PhiE = -V/2;

%% Form Laplacian matrices, permutation arrays, and
% Cholesky factorizations

% Create electric potential and connectivity matrices

Phi = zeros((ny+1)*(nx+1),1);

Ubc = dt*eta*([2*uS(2:end-1); zeros(ny-2,nx-1); ...
     2*uN(2:end-1)]/dx^2 + [uW' zeros(ny,nx-3) uE']/dy^2);

Vbc = dt*eta*([vS; zeros(ny-3,nx); vN]/dx^2 + ...
    [2*vW(2:end-1)' zeros(ny-1,nx-2) 2*vE(2:end-1)']/dy^2);
```

```
% Pressure update matrices
P = zeros(ny,nx);
p = reshape(P,[],1);
PM = P;
NP = 1:length(p);
Lp = kron(K1(nx,dx,1),speye(ny)) + ...
     kron(speye(nx),K1(ny,dy,1));

% force center node WP to pressure P = 0
WP = round((ny)*((nx)+(1-rem((nx),2)))/2);
Lp(WP,:) = [];
Lp(:,WP) = [];
NP(WP) = [];
p2 = zeros(length(NP),1);

% Create pressure permutation array and Cholesky
% factorization matrix using approximate minimum degree
% permutation
perp = symamd(Lp);
Rp = chol(Lp(perp,perp));
Rpt = Rp';

% Implicit viscosity update matrices

Lu = speye(ny*(nx-1))+dt*eta*(kron(K1(nx 1,dx,2), ...
     speye(ny)) + kron(speye(nx-1),K1(ny,dy,3)));

Lv = speye((ny-1)*nx) + dt*eta*(kron(K1(nx,dx,3), ...
     speye(ny-1)) + kron(speye(nx),K1(ny-1,dy,2)));

% Create viscosity permutation array and Cholesky
% factorization matrix using approximate minimum degree
% permutation
peru = symamd(Lu);
Ru = chol(Lu(peru,peru));
Rut = Ru';
perv = symamd(Lv);
Rv = chol(Lv(perv,perv));
Rvt = Rv';

% Electrical potential update matrix
M = kron(K1(nx+1,dx,1),speye(ny+1)) + ...
    kron(speye(nx+1),K1(ny+1,dy,1)));
```

```
% Remove rows and cols of fixed potential points WN, EN, NN
WN = round((ny+1)/2);
EN = (ny+1)*nx+round((ny+1)/2);
NN = 1:((ny+1)*(nx+1));

% Add contribution of fixed potentials to Laplacian of
% other grid points
LSWN = sum(M(:,WN),2);
LSEN = sum(M(:,EN),2);

% form contribution vector PhiB for poisson equation
PhiB = PhiW*LSWN+PhiE*LSEN;
M([WN EN],:) = [];
M(:,[WN EN]) = [];
NN([WN EN]) = [];
PhiM = zeros(length(NN),1);

% Create permutation array and Cholesky factorization
% matrix solving for electrical potential in Poisson's
% equation using approximate minimum degree permutation
perM = amd(M);
RM = chol(M(perM,perM));
RMt = RM';

% Solve for initial potentials
rhs = -PhiB;
rhs([WN EN]) = [];
% rhs = reshape(qo'/eo/er,[],1)+PhiB;
PhiM(perM) = RM\(RMt\rhs(perM));

% place back in dirichlet potentials
Phi(NN) = PhiM; Phi(WN) = PhiW; Phi(EN) = PhiE;
Phi2 = reshape(Phi,ny+1,nx+1);

% qo formulation for non-uniform charge density (final sims
% used uniform charge density
qo = zeros(size(Phi2));
QMEAN = mean(abs(qo(:)));
PMEAN = mean(abs(Phi2(:)));

% Plot initial electric potentials
figure; contourf(x,y,Phi2,20,'w-'), colorbar
Phi = sort(Phi2(:));
```

```
caxis(Phi([1 end]));

% Solve for Electric Fields
Ex = -diff(Phi2,1,2)/dx; % (V/m) stimulus (91x90)
Ey = -diff(Phi2,1,1)/dy; % (V/m) stimulus (90x91)
[Xavg, Yavg] = meshgrid(avg(x),avg(y));
[EX, N] = exbound(avg(Ex),Xavg,Yavg,d/2,0, 0,'circle',0);
[EY, N] = exbound(avg(Ey')',Xavg,Yavg,d/2,0,0,'circle',0);
EM = sqrt(EX.^2 + EY.^2);
disp(['Ex(min, mean, max) = (' num2str(min(Ex(:))), ...
     ', ', num2str(mean(Ex(:))) ', ', ...
     num2str(max(Ex(:))) ') V/m']);
disp(['Ey(min, mean, max) = (' num2str(min(Ey(:))), ...
     ', ', num2str(mean(Ey(:))) ', ', ...
     num2str(max(Ey(:))) ') V/m']);
disp(['EX(min, mean, max) = (' num2str(min(EX(:))), ...
     ', ', num2str(sum(EX(:))/N) ', ', ...
     num2str(max(EX(:))) ') V/m']);
disp(['EY(min, mean, max) = (' num2str(min(EY(:))), ...
     ', ', num2str(sum(EY(:))/N) ', ', ...
     num2str(max(EY(:))) ') V/m']);
disp(['EM(min, mean, max) = (' num2str(min(EM(:))), ...
     ', ', num2str(sum(EM(:))/N) ', ', ...
     num2str(max(EM(:))) ') V/m']);

% Display simulation parameters
fprintf(fid, '%s\n', ['-- Stimulus Parameters --']);
fprintf(fid, '%s\n', ['current pulse width: '
num2str(Tp*1000) ' ms']);
fprintf(fid, '%s\n', ['current pulse strength: '
num2str(I*1000) ' mA']);
fprintf(fid, '%s\n', ['electrode potentials: +/-'
num2str(V/2) ' V']);
fprintf(fid, '%s\n', ['Ex(min, mean, max) = ('
num2str(min(Ex(:))) ', ', num2str(mean(Ex(:))) ', ', ...
   num2str(max(Ex(:))) ') V/m']);
fprintf(fid, '%s\n', ['Ey(min, mean, max) = (', ...
   num2str(min(Ey(:))) ', ', num2str(mean(Ey(:))) ', ', ...
   num2str(max(Ey(:))) ') V/m']);
fprintf(fid, '\n');
fprintf(fid, '%s\n', ['-- MRI Parameters --']);
fprintf(fid, '%s\n', ['B-field, |Bz|: ' num2str(Bz) ' T']);
fprintf(fid, '%s\n', ['[Gx,Gy]: [' num2str(Gx*1000), ...
     ',', num2str(Gy*1000) '] mT/m']);
```

```
fprintf(fid, '%s\n', ['gradient lobe width: ', ...
     num2str(Tg*1000) ' ms']);
fprintf(fid, '%s\n', ['matrix size: ' num2str(MAT(1)), ...
     'x', num2str(MAT(2)) ' voxels']);
fprintf(fid, '%s\n', ['FOV: [' num2str(FOV(1)*100) ',', ...
    num2str(FOV(2)*100) '] cm']);
fprintf(fid, '%s\n', ['b-factor: ' num2str(b*1e-6), ...
     ' s/mm^2']);
fprintf(fid, '%s\n', ['diffusion weighting: ', ...
     num2str(dw)]);
fprintf(fid, '\n');
fprintf(fid, '%s\n', ['-- MHD Parameters --']);
fprintf(fid, '%s\n', ['total simulation time: ', ...
     num2str(tmax*1000) ' ms']);
fprintf(fid, '%s\n', ['simulation time step: ', ...
     num2str(dt*1000) ' ms']);

% Estimate simulation run time using MHD_SquareTimed
% version of code compute simulation loop for one time step
loadtime = toc; tic;
MHD_SquareTimed;
runtime = toc*tmax/dt + 2*loadtime;
fprintf(fid, '%s\n', ['estimated run time: ', ...
     s2hms(runtime)]);

%==========================================================
%% EMHD and LEI simulation
j = 0; l = 0; if Vmulti, jjj = 0; end
tt(1) = 0; tmag = 0;
VM = zeros(size(X));

% initialize time-dependent variables for plotting
if timedep
    Vx = avg([uS; [uW' vx uE']; uN]);
    Vy = avg([vW' [vS; vy; vN] vE']')';
    Vf = sqrt(Vx.^2 + Vy.^2);
    [VF, N] = exbound(Vf, X, Y, d/2, 0, 0, 'circle', 0);
    vv(j+1) = max(VF(:));
    vm(j+1) = sum(VF(:))/N;
    [DM, N] = exbound(sqrt((xc-xw).^2 + (yc-yw).^2), ...
        xw, yw, d/2, 0, 0, 'circle', 0);
    dd(j+1) = max(DM(:));
    dm(j+1) = sum(DM(:))/N;
    [PM, N] = exbound(ph, xw, yw, d/2, 0, 0, 'circle', 0);
```

```
    pp(j+1) = max(PM(:));
    pm(j+1) = sum(PM(:))/N;
end

% simulation loop
for t = dt:dt:tmax
    % initial velocity at each time step
    vxo = [uW' vx uE'];
    vyo = [vS; vy; vN];
    % EM force correction %%%%%%%%%%%%%%%%%%%%%%%%%%%%%%%%%%
    if FTT == 0  % EM force update first
        % first order model
        % v = E x B / B2 = [vx = Ey*Bz; vy = -Ex*Bz]
        % v = J x B
        % J = sigma*(E + v x B)
        % fx = +Bz*sig*(Vo*Ey(:,2:end-1) - Bz*vx);
        % fy = -Bz*sig*(Vo*Ex(2:end-1,:) + Bz*vy);
        % fx is a small negative number dominated by -Bz*vx
        % fy is a large negative number dominated by Ex
        Jx = sig*(Vo*Ex(2:(end-1),:) + Cb*Bz*vy);
        Jy = sig*(Vo*Ey(:,2:(end-1)) - Cb*Bz*vx);
        % f = J x B volumetric Lorentz force on a
        % conducting fluid
        fx = Bz*Jy;
        fy = -Bz*Jx;
        % Update velocity due to EM force
        vx = vx+Cf*fx;
        vy = vy+Cf*fy;
        if Vmulti == 1
            disp(['Vfig #' num2str(jjj+1), ...
                ': after Lorentz force correction']); Vfig;
        end
    end

    % compute velocity at the end of each time step
    % Navier-Stokes SIMPLE Method
    % treat nonlinear terms
    Vxo = [uW' vx uE'];
    Vyo = [vS; vy; vN];
    gamma = min(1.2*dt*max(max(abs(vx(:))) / ...
         dx,max(abs(vy(:)))/dy),1);
    Ue = [2*uS-Vxo(1,:); Vxo; 2*uN-Vxo(end,:)];
    Ve = [2*vW'-Vyo(:,1) Vyo 2*vE'-Vyo(:,end)];
    Ua = avg(Ue);
```

```
Ud = diff(Ue,1,1)/2;
Va = avg(Ve')';
Vd = diff(Ve,1,2)/2;
UVx = diff(Ua.*Va-gamma*abs(Ua).*Vd,1,2)/dx;
UVy = diff(Ua.*Va-gamma*Ud.*abs(Va),1,1)/dy;

Ua = avg(Ue(2:end-1,:)')';
Ud = diff(Ue(2:end-1,:),1,2)/2;
Va = avg(Ve(:,2:end-1));
Vd = diff(Ve(:,2:end-1),1,1)/2;

U2x = diff(Ua.^2-gamma*abs(Ua).*Ud,1,2)/dx;
V2y = diff(Va.^2-gamma*abs(Va).*Vd,1,1)/dy;

if ~upwind
% Remove gamma term, no upwinding
    Ue = [2*uS-vxo(1,:); vxo; 2*uN-vxo(end,:)];
    Ve = [2*vW'-vyo(:,1) vyo 2*vE'-vyo(:,end)];
    Ua = avg(Ue);
    Va = avg(Ve')';
    UVx = diff(Ua.*Va,1,2)/dx;
    UVy = diff(Ua.*Va,1,1)/dy;
    Ua = avg(Ue(2:end-1,:)')';
    Va = avg(Ve(:,2:end-1));
    U2x = diff(Ua.^2,1,2)/dx;
    V2y = diff(Va.^2,1,1)/dy;
end

% update velocity due to convective acceleration
if FTT == 1  % Combine convection and force update
    vx = vx-dt*(UVy(:,2:end-1)+U2x) + Cf*fx;
    vy = vy-dt*(UVx(2:end-1,:)+V2y) + Cf*fy;
    if Vmulti == 1
        disp(['Vfig #' num2str(jjj+1), ...
        ': after Lorentz force and convection', ...
        ' correction']); Vfig;
    end
else         % Convection update only
    vx = vx-dt*(UVy(:,2:end-1)+U2x);
    vy = vy-dt*(UVx(2:end-1,:)+V2y);
    if Vmulti == 1
        disp(['Vfig #' num2str(jjj+1), ...
            ': after convective acceleration', ...
            ' correction']);
```

```
        Vfig;
    end
end

if FTT == 2  % EM force update after convection update
    Jx = sig*Vo*(Ex(2:(end-1),:) + Cb*Bz*vy);
    Jy = sig*Vo*(Ey(:,2:(end-1)) - Cb*Bz*vx);
    % f = J x B volumetric Lorentz force on a
    % conducting fluid
    fx = Bz*Jy;
    fy = -Bz*Jx;
    % Update velocity due to EM force
    vx = vx+Cf*fx;
    vy = vy+Cf*fy;
    if Vmulti == 1
        disp(['Vfig #' num2str(jjj+1), ...
        ': after Lorentz force correction']); Vfig;
    end
end

% update velocity due to implicit viscosity
% vectorize matrices, compute cholesky solution to
% inverse problem
rhs = reshape(vx+Ubc,[],1);
u(peru) = Ru\(Rut\rhs(peru));
vx = reshape(u,ny,nx-1);
rhs = reshape(vy+Vbc,[],1);
v(perv) = Rv\(Rvt\rhs(perv));
vy = reshape(v,ny-1,nx);
if Vmulti == 1
    disp(['Vfig #' num2str(jjj+1), ...
    ': after implicit viscosity correction']); Vfig;
end

if FTT == 3  % EM force update after viscosity
    Jx = sig*Vo*(Ex(2:(end-1),:) + Cb*Bz*vy);
    Jy = sig*Vo*(Ey(:,2:(end-1)) - Cb*Bz*vx);
    % f = J x B volumetric Lorentz force on a
    % conducting fluid
    fx = Bz*Jy;
    fy = -Bz*Jx;
    % Update velocity due to EM force
    vx = vx+Cf*fx;
    vy = vy+Cf*fy;
```

```
    if Vmulti == 1
        disp(['Vfig #' num2str(jjj+1), ...
        ': after Lorentz force correction']); Vfig;
    end
end

% Pressure correction by solving linear system from
% Poisson Equation
% -Laplacian(P)/pf = -(1/dt)*grad(v)
rhs = reshape(diff([uW' vx uE'],1,2)/dx + ...
    diff([vS; vy; vN],1,1)/dy,[],1)/Cp;
rhs(WP) = [];
p2(perp) = -Rp\(Rpt\rhs(perp));
p(NP) = p2; p(WP) = 0;
P = reshape(p,ny,nx);
vx = vx-Cp*diff(P,1,2)/dx;
vy = vy-Cp*diff(P,1,1)/dy;
if Vmulti == 1
    disp(['Vfig #' num2str(jjj+1), ...
    ': after pressure correction']); Vfig;
end

if FTT == 4  % EM force update after pressure update
    Jx = sig*(Vo*Ex(2:(end-1),:) + Cb*Bz*vy);
    Jy = sig*(Vo*Ey(:,2:(end-1)) - Cb*Bz*vx);
    % f = J x B volumetric Lorentz force on a
    % conducting fluid
    fx = Bz*Jy;
    fy = -Bz*Jx;
    % Update velocity due to EM force
    vx = vx+Cf*fx;
    vy = vy+Cf*fy;
    if Vmulti == 1
        disp(['Vfig #' num2str(jjj+1), ...
        ': after Lorentz force correction']); Vfig;
    end
end

if PTT
    %%%%%%%%%%%%%%%%%%%%%%%%%%%%%%%%%%%%%%%%%%%%%%%%%%%
    % Compute mean velocity and distance traveled
    % vm = mean velocity per time step at each point
    vxm = ([uW' vx uE']+vxo)/2;
    vym = ([vS; vy; vN]+vyo)/2;
```

```
% Compute distance traveled for each molecule based
% on location within voxel using linear
% approximation
% D = (vi + vf)/2*dt
XI = fix((xc+d/2-eps*10)/dx)+1;
YI = fix((yc+d/2-eps*10)/dy)+1;
xrem = rem((xc+d/2),dx)/dx;
yrem = rem((yc+d/2),dy)/dy;
ddx = dt*(xrem.*vxm(YI+ny*XI) + ...
    (1-xrem).*vxm(YI+ny*(XI-1)));
ddy = dt*(yrem.*vym(YI+1+(ny+1)*(XI-1)) + ...
    (1-yrem).*vym(YI+(ny+1)*(XI-1)));

% Compute phase from xo, yo and update xc, yc
xo = xc; yo = yc;
xc = xc + ddx; yc = yc + ddy;
% Limit water to region inside square
K2 = find( (abs(xc) > (d/2-eps)) | ...
     (abs(yc) > (d/2-eps)) );
if ~isempty(K2)
    % bounce water off boundary (inelastic, deflect
    % distance = eps)
    % determine intersection of trajectory and
    % circle
    deltax = ddx(K2);
    deltay = ddy(K2);
    xoo = xo(K2);
    yoo = yo(K2);
    xi = xc(K2);
    yi = yc(K2);
    mi = deltay./deltax;     % slope
    bi = yoo - mi.*xoo;      % intercept
    IS = abs(deltax) <= eps; % infinite slope index

    % if infinite slope
    K4 = find(IS);
    yi(K4) = sign(deltay(K4))*(d/2-eps);
    xi(K4) = xoo(K4);
    % wrong intersection condition
    KW = find(abs(xi(K4)) > (d/2-eps));
    xi(K4(KW)) = sign(deltax(K4(KW)))*(d/2-eps);
    yi(K4(KW)) = ...
         [mi(K4(KW)).*xi(K4(KW))+bi(K4(KW))];
```

```
        % if non-infinite slope
        K3 = find(~IS);
        xi(K3) = sign(deltax(K3))*(d/2-eps);
        yi(K3) = [mi(K3).*xi(K3)+bi(K3)];
        % wrong intersection condition
        KW = find(abs(yi(K3)) > (d/2-eps));
        yi(K3(KW)) = sign(deltay(K3(KW)))*(d/2-eps);
        xi(K3(KW)) = [(yi(K3(KW)) - ...
             bi(K3(KW)))./mi(K3(KW))];

        % determine incidence (a) and intersection
        % (theta) angles
        % resultant angle (rang) is in opposite
        % direction of motion
        % rang = pi + 2*theta - a
        if bounce
            rang = pi + (2*atan2(yi,xi) - ...
            atan2(deltay,deltax));
        else
            rang = pi+atan2(yi,xi);
        end
        xc(K2) = xi+eps.*cos(rang);
        yc(K2) = yi+eps.*sin(rang);
        % update differential displacement
        ddx(K2) = xc(K2) - xoo;
        ddy(K2) = yc(K2) - yoo;
    end

    K3 = find( (abs(xc) > (d/2-eps)));
    xc(K3) = sign(xc(K3))*d/2;
    K4 = find( (abs(yc) > (d/2-eps)));
    yc(K4) = sign(yc(K4))*d/2;
    % Warning when correcting out of bounds error
    if ( ~isempty(K3) || ~isempty(K4) )
        fprintf(fid, '%s\n', ...
            ['warning out of bounds: past xlim = ' ...
            num2str(length(K3)) ', past ylim = ', ...
            num2str(length(K4)) ' at t = ', ...
            num2str(t*1000) 'msec']);
    end
else
    ddx = dt*avg(([uW' vx uE']+vxo)')'/2;
    ddy = dt*avg([vS; vy; vN]+vyo)/2;
    xc = xc + ddx;
```

```
    yc = yc + ddy;
end

%% Compute phase accumulating over each time step
j = j+1;
if PTT
    ph = ph + g*dt*(Gx*(xc-ddx/2)+Gy*(yc-ddy/2));
else
    % include boundary nodes
    vxm = [uW' vx uE'];
    vym = [vS; vy; vN];
    [phdx,phdy] = gradient(ph,dx,dy);
    ph = ph + dt*(g*(Gx*xw+Gy*yw) - ...
    phdx.*avg(vxm')'-phdy.*avg(vym));
end

% store mean and max velocity, displacement, and phase
Vx = avg([uS; [uW' vx uE']; uN]);
Vy = avg([vW' [vS; vy; vN] vE']')';
Vf = sqrt(Vx.^2 + Vy.^2);   % ny+1 x nx+1
Dm = sqrt((xc-xw).^2 + (yc-yw).^2);

% store time dependent plot variables
tt(j+1) = t;
if timedep
    % final velocity in circular phantom region
    [VF, N] = exbound(Vf,X,Y,d/2,0,0,'circle', 0);
    vl(j+1) = min(VF(:));
    vv(j+1) = max(VF(:));
    vm(j+1) = sum(VF(:))/N;
    % final displacement in circular phantom region
    [DM, N] = exbound(Dm,xw,yw,d/2,0,0,'circle',0);
    dl(j+1) = min(DM(:));
    dd(j+1) = max(DM(:));
    dm(j+1) = sum(DM(:))/N;
    % final phase shift in circular phantom region
    [PM, N] = exbound(ph,xw,yw,d/2,0,0,'circle',0);
    pl(j+1) = min(PM(:));
    pp(j+1) = max(PM(:));
    pm(j+1) = sum(PM(:))/N;
end

% Determine lobe parameters
% current lobe number (final lobenum = 2*ngo)
```

```
lobenum = ceil(j/nt);

% End of negative lobe
if (t>(Tg-dt))&&(rem(j,2*nt) == 0)
    % positive-pulse gradient sequence initiation
    fprintf(fid, '\n%s\n', ['-- End of lobe #', ...
        num2str(lobenum), ', t = ' num2str(t*1000), ...
        ' msec, Gx = ' num2str(Gx*1000), ...
        ' mT/m, I = ' num2str(I*Vo*1000) ' mA --']);
    Vo = 1; Gx = Gxo; Gy = Gyo;
end
% End of positive lobe
if (t>(Tg-dt))&&(rem(j,2*nt) == nt)
    % store final parameter values at end of each pos
    % gradient lobe
    VFx = Vx; VFy = Vy; Vm = Vf; tmag = t; PR = P;
    EMx = Ex; EMy = Ey;
    % negative-pulse gradient sequence initiation
    fprintf(fid, '\n%s\n', ['-- End of lobe #', ...
         num2str(lobenum), ', t = ', ...
         num2str(t*1000) ' msec, Gx = ', ...
         num2str(Gx*1000), ' mT/m, I = ', ...
         num2str(I*Vo*1000) ' mA --']);
    % set new gradient and current lobe magnitudes
    Vo = 0; Gx = -Gxo; Gy = -Gyo;
end

if qupdate
    % Update qo and Phi
    % dq/dt = -sig*div(E + v x B)
    % dq/dt = -sig*div(Ex + vy*Bz, Ey - vx*Bz)
    % dq/dt = -sig*(diff(Ex + vy*Bz,1,2)/dx +, ...
    % diff(Ey - vx*Bz,1,1)/dy)
    LEx = Vo*diff(Ex,1,2)/dx;
    LEy = Vo*diff(Ey,1,1)/dy;
    qo(2:(end-1),2:(end-1)) = qo(2:(end-1), ...
         2:(end-1)) - dt*sig*(LEx(2:(end-1),:) + ...
         LEy(:,2:(end-1)));
    % rhs from qo and removed dirichlet nodes from Phi
    rhs = -Vo*PhiB - reshape(qo,[],1)/eo/er;
    rhs([WN EN]) = [];

    PhiM(perM) = RM\(RMt\rhs(perM));
    % place back in dirichlet potentials
```

```
    Phi(NN) = PhiM;
    Phi(WN) = Vo*PhiW;
    Phi(EN) = Vo*PhiE;
    Phi2 = reshape(Phi,ny+1,nx+1);
    QMEAN = mean(abs(qo(:)));
    PMEAN = mean(abs(Phi2(:)));

    % Update Electric Fields
    Ex = -diff(Phi2,1,2)/dx;   % (V/m) stimulus (91x90)
    Ey = -diff(Phi2,1,1)/dy;   % (V/m) stimulus (90x91)
end

% display average and final velocity, displacement and
% phase at the end
% of each pulse-gradient lobe at time t = tmag
if (t>(Tg-dt))&&(rem(j,nt) == 0)
    l = l+1;
    % display final velocity, phase, and displacement;
    fprintf(fid,'%s\n',['|v| (min, mean, max): (', ...
    num2str(vl(j+1)), ', ' num2str(vm(j+1)), ...
    ', ' num2str(vv(j+1)) ') m/s']);
    fprintf(fid,'%s\n',['|d| (min, mean, max): (', ...
         num2str(dl(j+1)), ', ' num2str(dm(j+1)), ...
         ', ' num2str(dd(j+1)) ') m']);
    fprintf(fid,'%s\n',['phi (min, mean, max): (', ...
         num2str(pl(j+1)), ', ' num2str(pm(j+1)), ...
         ', ' num2str(pp(j+1)) ') rad']);
end

% visualization during simulation
if (floor(50*j/ndt)>floor(50*(j-1)/ndt))&&(j<=ndt)
    fprintf(fid, '%s\n', [num2str(100*j/ndt), ...
    '% complete']);
end
if (runopt >= 2)&&(rem(j,nsteps)==1)
   if qupdate
       % plot updated potentials map for charge density
       % redistribution, not used in final sims
       figure(H1);
       clf, contourf(x*100,y*100,Phi2,20,'w-');
       colorbar; drawnow;
   end
end
if Vmulti
```

```
        break;
    end
end

%% Display Navier-Stokes Variables

[Xavg, Yavg] = meshgrid(avg(x),avg(y));
if (runopt >= 2)
    % Plot electric potential contour map
    H1 = figure;
    contourf(x*100,y*100, ...
         exbound(Phi2,X,Y,d/2,0,0,'circle',0),20,'w-');
    caxis([min(Phi2(:)) max(Phi2(:))]);
    [cmin cmax] = caxis; axis square;
    colorbar; cmap = colormap('gray');
    cref = round((0-cmin)/(cmax-cmin)*length(cmap));
    if cref < 1, cref = 1; end
    refcolor = cmap(cref,:);
    % widen field of view to match JMR paper
    axis([-6, 6, -6, 6]); axis ij;
    set(gca, 'Color', refcolor);
    if drawcirc, hold on;
         circle(0,0,100*d/2,'-r','LineWidth',2); end
    xlabel('x (cm)'); ylabel('y (cm)');
    title(['Electric potential contours for I = ', ...
        num2str(I*1000), ' mA, at t = ', ...
        num2str(t*1000) ' msec']);
    if (runopt ~= 2)
        saveas(H1,[sprintf(plotfile) '_Phi.fig'],'fig')
        saveas(H1,[sprintf(plotfile) '_Phi.png'],'png')
        fprintf(fid, '%s\n', ['Phi plot saved to: ', ...
        plotfile '_Phi']);
    end

    % Plot pressure contour map
    H2 = figure;
    contourf(avg(x)*100,avg(y)*100, ...
       exbound(PR,Xavg,Yavg,d/2,0,0,'circle',0),20,'w-');
    caxis([min(PR(:)) max(PR(:))]);
    [cmin cmax] = caxis; axis square;
    colorbar; cmap = colormap('gray');
    cref = round((0-cmin)/(cmax-cmin)*length(cmap));
    if cref < 1, cref = 1; end
    refcolor = cmap(cref,:);
```

```
% widen field of view to match JMR paper
axis([-6, 6, -6, 6]); axis ij;
set(gca, 'Color', refcolor);
if drawcirc, hold on;
   circle(0,0,100*d/2,'-r','LineWidth',2); end
xlabel('x (cm)'); ylabel('y (cm)');
title(['Pressure contours for I = ', ...
   num2str(I*1000), ' mA at t = ' num2str(tmag*1000)]);
if (runopt ~= 2)
   saveas(H2,[sprintf(plotfile) '_PR.fig'],'fig')
   saveas(H2,[sprintf(plotfile) '_PR.png'],'png')
   fprintf(fid, '%s\n', ['PR plot saved to: ', ...
   plotfile '_PR']);
end

% Plot pressure contour map
H3 = figure;
contourf(avg(x)*100,avg(y)*100, ...
    exbound(P, Xavg, Yavg, d/2, 0, 0, 'circle', ...
    0),20,'w-');
caxis([min(P(:)) max(P(:))]);
[cmin cmax] = caxis; axis square;
colorbar; cmap = colormap('gray');
cref = round((0-cmin)/(cmax-cmin)*length(cmap));
if cref < 1, cref = 1; end
refcolor = cmap(cref,:);
% widen field of view to match JMR paper
axis([-6, 6, -6, 6]); axis ij;
set(gca, 'Color', refcolor);
if drawcirc, hold on;
     circle(0,0,100*d/2,'-r','LineWidth',2); end
xlabel('x (cm)'); ylabel('y (cm)');
title(['Pressure contours for I = ', ...
     num2str(I*1000), ' mA at t = ' num2str(t*1000)]);
if (runopt ~= 2)
    saveas(H3,[sprintf(plotfile) '_PF.fig'],'fig')
    saveas(H3,[sprintf(plotfile) '_PF.png'],'png')
    fprintf(fid, '%s\n', ['PF plot saved to: ', ...
         plotfile '_PF']);
end

% draw streamslice of electric field lines in clipped
% circular phantom
EX = exbound(avg(Ex),Xavg,Yavg,d/2,0,0,'circle',0);
```

```
EY = exbound(avg(Ey')',Xavg,Yavg,d/2,0,0,'circle',0);
EM = sqrt(EX.^2 + EY.^2);
H32 = figure;
contourf(avg(x)*100,avg(y)*100,EM,20,'w-');
caxis([min(EM(:)), 50]); hold on;
[cmin cmax] = caxis; axis square;
colorbar; cmap = colormap('gray');
cref = round((0-cmin)/(cmax-cmin)*length(cmap));
if cref < 1, cref = 1; end
refcolor = cmap(cref,:);
HS = streamslice2(avg(x)*100,avg(y)*100,EX,EY,1.5);
set(HS,'Color','white');
if drawcirc, circle(0,0,100*d/2,'-r','LineWidth',2);
end
% widen field of view to match JMR paper
axis([-6, 6, -6, 6]); axis ij;
set(gca, 'Color', refcolor);
xlabel('x (cm)'); ylabel('y (cm)');
title(['Electric field lines for I = ', ...
     num2str(I*1000), ' mA at t = ', ...
     num2str(tmag*1000) ' msec']);

VM = exbound(Vm, X, Y, d/2, 0, 0, 'circle', 0);
% Display Image of VM (speeds in phantom at end of
% final current pulse)
% plot VM values in full square phantom domain
H4 = figure;
contourf(x*100,y*100,VM,20,'w-');
caxis([min(VM(:)), max(VM(:))]); hold on;
[cmin cmax] = caxis; axis square;
colorbar; cmap = colormap('gray');
cref = round((0-cmin)/(cmax-cmin)*length(cmap));
if cref < 1, cref = 1; end
refcolor = cmap(cref,:);
% Add velocity streamslice
HS = streamslice2(X*100,Y*100, ...
    exbound(VFx,X,Y,d/2,0,0,'circle',0), ...
    exbound(VFy,X,Y,d/2,0,0,'circle',0),1.5);
set(HS,'Color','white');
if drawcirc, circle(0,0,100*d/2,'-r','LineWidth',2);
end
% widen field of view to match JMR paper
axis([-6, 6, -6, 6]); axis ij;
set(gca, 'Color', refcolor);
```

```
xlabel('x (cm)'); ylabel('y (cm)');
title(['VM and velocity streamlines for I = ', ...
     num2str(I*1000), ' mA at t = ' num2str(tmag), ...
     ' msec']);
if (runopt ~= 2)
    saveas(H4,[sprintf(plotfile) '_VM.fig'],'fig')
    saveas(H4,[sprintf(plotfile) '_VM.png'],'png')
    fprintf(fid, '%s\n', ['VM plot saved to: ', ...
         plotfile '_VM']);
end

% plot VM values in clipped circular phantom domain
[VF, N] = exbound(Vf, X, Y, d/2, 0, 0, 'circle', 0);
fprintf(fid, '%s\n', ['|v| (min, mean, max): (', ...
     num2str(min(VF(:))), ', ', ...
     num2str(sum(VF(:))/N) ', ', ...
     num2str(max(VF(:))) ') m/s']);
% Display Image of VF (speeds in phantom)
H42 = figure;
contourf(x*100,y*100,VF,20,'w-');
caxis([min(VF(:)), max(VF(:))]); hold on;
[cmin cmax] = caxis; axis square;
colorbar; cmap = colormap('gray');
cref = round((0-cmin)/(cmax-cmin)*length(cmap));
if cref < 1, cref = 1; end
refcolor = cmap(cref,:);
% Add velocity streamslice
HS = streamslice2(X*100,Y*100,
     exbound(Vx,X,Y,d/2,0,0,'circle',0), ...
     exbound(Vy,X,Y,d/2,0,0,'circle',0),1.5);
set(HS,'Color','white');
if drawcirc, circle(0,0,100*d/2,'-r','LineWidth',2);
end
% widen field of view to match JMR paper
axis([-6, 6, -6, 6]); axis ij;
set(gca, 'Color', refcolor);
xlabel('x (cm)'); ylabel('y (cm)');
title(['VF and velocity streamlines for I = ', ...
     num2str(I*1000), ' mA at t = ', ...
     num2str(t*1000) ' msec']);
if (runopt ~= 2)
    saveas(H42,[sprintf(plotfile) '_VF.fig'],'fig')
    saveas(H42,[sprintf(plotfile) '_VF.png'],'png')
    fprintf(fid, '%s\n', ['VF plot saved to: ', ...
```

```
            plotfile '_VF']);
    end
end

%% Display MRI image
fprintf(fid, '\n');
fprintf(fid, '%s\n', ['-- MRI capture after ', ...
     num2str(round(j/nt/2)), ' oscillations, tf = ', ...
     num2str(t*1000) ' msec --']);

% form signal matrix based on voxel grid
S = zeros(nr,nc);    % signal per voxel (with current)
N = zeros(nr,nc);    % number of spin particles per voxel
                     % (with current)
N0 = zeros(nr,nc);   % number of ref spin particles per
                     % voxel (no current)
ND = zeros(nr,nc);   % mean displacement per voxel (with
                     % current)
DD = zeros(nr,nc);   % mean displacement per voxel (with
                     % current)
PH = zeros(nr,nc);   % mean phase per voxel (with current)

% place water in voxels to compute signal loss
if PTT
    % water molecules positions with current applied
    xi = fix((xc+FOV(1)/2-eps)/DX)+1;
    yi = fix((yc+FOV(2)/2-eps)/DY)+1;
    % water molecule positions without current applied
    % (reference signal)
    xi0 = fix((xw+FOV(1)/2-eps)/DX)+1;
    yi0 = fix((yw+FOV(2)/2-eps)/DY)+1;
else
    % water molecule positions without current applied
    % (reference signal)
    xi = fix((xw+FOV(1)/2-eps)/DX)+1;
    yi = fix((yw+FOV(2)/2-eps)/DY)+1;
end

% store phi from -pi to +pi
p2 = ang2(ph(:));

% compute SR = (S-S0)/S = 1/N*sum(S)-1
for k = 1:nw
    % sum mean phase per voxel
```

```
    PH(yi(k),xi(k)) = (PH(yi(k),xi(k))*N(yi(k),xi(k)) + ...
         ph(k))/(N(yi(k),xi(k)) + 1);
    % add contribution to signal strength S for each
    % particle
    if PTT
         S(yi(k),xi(k)) = S(yi(k),xi(k)) + exp(1i*ph(k));
         % mean displacement per voxel
         DD(yi(k),xi(k)) = (DD(yi(k),xi(k)) * ...
         N(yi(k),xi(k)) + Dm(k))/(N(yi(k),xi(k)) + 1);
         % ref number of particles / voxel with current off
         N0(yi0(k),xi0(k)) = N0(yi0(k),xi0(k)) + 1;
    else
         S(yi(k),xi(k)) = S(yi(k),xi(k)) + exp(1i*ph(k));
    end
    % add to number of particles in voxel
    N(yi(k),xi(k)) = N(yi(k),xi(k)) + 1;
end

% Compute phase "flow" of signal vector per voxel
SP = atan2(imag(S),real(S));

if PTT
    % Other parameters to be plotted
    % Difference between number of particles per voxel with
    % reference
    ND = (N-N0)./(N0+eps);

    % Compute magnitude of S relative to S0 in the phantom
    % with no current
    S = (abs(S)-N0)./(N0+eps);
    % note: S = dw*S and S0 = dw*N0, but in difference
    % image dw divides out
else
    S = abs(S)./(N+eps) - 1;
end

%% Display results

% Report and plot final values for v, d, and S
fprintf(fid, '%s\n', ['Final values computed at t = ', ...
    num2str(t*1000), ' msec']);

% Compute and report velocity magnitude in circular phantom
[VF, N] = exbound(Vf, X, Y, d/2, 0, 0, 'circle', 0);
```

```
[VFX, N] = exbound(VFx, X, Y, d/2, 0, 0, 'circle', 0);
[VFY, N] = exbound(VFy, X, Y, d/2, 0, 0, 'circle', 0);
[VX, N] = exbound(Vx, X, Y, d/2, 0, 0, 'circle', 0);
[VY, N] = exbound(Vy, X, Y, d/2, 0, 0, 'circle', 0);
[VM, N] = exbound(Vm, X, Y, d/2, 0, 0, 'circle', 0);

% Report magnitude of velocity at end of gradients
fprintf(fid, '%s\n', ['VF(Min,Mean,Max): (', ...
    num2str(min(VF(:))), ',', ...
    num2str(sum(VF(:))/N), ',', num2str(max(VF(:))), ...
    ') at t = ', num2str(t*1000), ' msec']);

% Report magnitude of velocity at end of last current pulse
fprintf(fid, '%s\n', ['VM(Min,Mean,Max): (', ...
    num2str(min(VM(:))), ',', ...
    num2str(sum(VM(:))/N), ',', num2str(max(VM(:))), ...
    ') at t = ', num2str(tmag*1000), ' msec']);

% Report particle displacement from original location in
% circular phantom
Dx = xc - xw; Dy = yc - yw;
[DX, N] = exbound(Dx, xw, yw, d/2, 0, 0, 'circle', 0);
[DY, N] = exbound(Dy, xw, yw, d/2, 0, 0, 'circle', 0);
[DM, N] = exbound(sqrt(Dx.^2 + Dy.^2), ...
          xw, yw, d/2, 0, 0, 'circle', 0);
fprintf(fid, '%s\n', ...
    ['DM(Min,Mean,Max) (cm) starting in phantom: (', ...
    num2str(100*min(DM(:))), ',', ...
    num2str(100*sum(DM(:))/N), ',', ...
    num2str(100*max(DM(:))), ') at t = ', ...
    num2str(t*1000), ' msec']);

% Report mean displacement per voxel in circular phantom
[DD, N] = exbound(DD, XX, YY, d/2, 0, 0, 'circle', 0);
fprintf(fid, '%s\n', ...
    ['DD(Min,Mean,Max) (cm) in phantom: (', ...
    num2str(100*min(DD(:))), ',', ...
    num2str(100*sum(DD(:))/N), ',', ...
    num2str(100*max(DD(:))), ') at t = ', ...
    num2str(t*1000), ' msec']);

% Report relative signal change in the full square domain
fprintf(fid, '%s\n', ['mean(Sphase): '
num2str(sum(SP(:))/NV) ' rad']);
```

```
fprintf(fid, '%s\n', ['%S(Min,Mean,Max) (%) in FOV: (', ...
    num2str(100*min(S(:))), ', ', ...
    num2str(100*mean(S(:))), ', ', ...
    num2str(100*max(S(:))), ')%']);

% Report relative signal change in the clipped circular
% phantom domain
[SD, N] = exbound(S, XX, YY, d/2, 0, 0, 'circle', 0);
fprintf(fid, '%s\n', ...
    ['SD(Min,Mean,Max) (%) in phantom: (', ...
    num2str(100*min(SD(:))), ',', ...
    num2str(100*sum(SD(:))/N), ',', ...
    num2str(100*max(SD(:))), ')']);

if plotextra
    % visualize velocity
    H3 = figure;
    contourf(x*100,y*100,VM,20,'w-');
    caxis([min(VM(:)), max(VM(:))]); hold on;
    [cmin cmax] = caxis; axis square;
    colorbar; cmap = colormap('gray');
    cref = round((0-cmin)/(cmax-cmin)*length(cmap));
    if cref < 1, cref = 1; end
    refcolor = cmap(cref,:);
    HS = streamslice2(X*100,Y*100,VFX,VFY,1.5);
    set(HS,'Color','white');
    if drawcirc, circle(0,0,100*d/2,'-r','LineWidth',2);
end
    % widen field of view to match JMR paper
    axis([-6, 6, -6, 6]); axis ij;
    set(gca, 'Color', refcolor);
    xlabel('x (cm)'); ylabel('y (cm)');
    title(['|vm| and streamlines for I = ', ...
         num2str(I*1000), ...
         ' mA at t = ' num2str(tmag*1000) ' msec']);

    H32 = figure;
    contourf(x*100,y*100,VF,20,'w-');
    caxis([min(VF(:)), max(VF(:))]); hold on;
    [cmin cmax] = caxis; axis square;
    colorbar; cmap = colormap('gray');
    cref = round((0-cmin)/(cmax-cmin)*length(cmap));
    if cref < 1, cref = 1; end
    refcolor = cmap(cref,:);
```

```
    HS = streamslice2(X*100,Y*100,VX,VY,1.5);
    set(HS,'Color','white');
    if drawcirc, circle(0,0,100*d/2,'-r','LineWidth',2);
    end
    % widen field of view to match JMR paper
    axis([-6, 6, -6, 6]); axis ij;
    set(gca, 'Color', refcolor);
    xlabel('x (cm)'); ylabel('y (cm)');
    title(['|vf| and streamlines for I = ', ...
         num2str(I*1000), ...
         ' mA at t = ' num2str(t*1000) ' msec']);

    % visualize displacement
    H4 = figure;
    imageFOV(DM, xw*100, yw*100, 12, 12, 0, 0, 0);
    caxis([min(DM(:)), max(DM(:))]); hold on;
    [cmin cmax] = caxis; axis square;
    colorbar; cmap = colormap('gray');
    cref = round((0-cmin)/(cmax-cmin)*length(cmap));
    if cref < 1, cref = 1; end
    refcolor = cmap(cref,:);
    HS = streamslice2(xw*100,yw*100,DX,DY,1.5);
    set(HS,'Color','white');
    if drawcirc, circle(0,0,100*d/2,'-r','LineWidth',2);
    end
    % widen field of view to match JMR paper
    axis([-6, 6, -6, 6]); axis ij;
    set(gca, 'Color', refcolor);
    xlabel('x (cm)'); ylabel('y (cm)');
    title(['|d| and streamlines for I = ', ...
         num2str(I*1000), ...
         ' mA at t = ' num2str(t*1000) ' msec']);
end

% Visualize uncorreted relative signal change in full
% square phantom domain
H6 = figure;
imageFOV(SD*100, XX*100, YY*100, 12, 12, 0, 0, 0);
caxis([-40, 40]);
[cmin cmax] = caxis; axis square;
colorbar; cmap = colormap('gray');
cref = round((0-cmin)/(cmax-cmin)*length(cmap));
if cref < 1, cref = 1; end
refcolor = cmap(cref,:);
```

```
% widen field of view to match JMR paper
if drawcirc, hold on; circle(0,0,100*d/2,'-
r','LineWidth',2); end
axis([-6, 6, -6, 6]); axis ij; set(gca, 'Color', refcolor);
xlabel('x (cm)'); ylabel('y (cm)');
title('SD: % signal magnitude change per voxel');

if plotextra
    % display SD plot compare data
    fprintf(fid, '%s\n', ['SD plot compare data:']);
    LEIcompare(SD, -0.40, XX, YY, d/2, 0, 0, 'circle');

    % Display uncorrected LEI signal image in full square
    % phantom domain
    H5 = figure;
    imageFOV(S*100, XX*100, YY*100, 12, 12, 0, 0, 0);
    % narrow scale to 40% of maximum (higher contrast) to
    % match JMR paper
    caxis([-40, 40]);
    [cmin cmax] = caxis; axis square;
    colorbar; cmap = colormap('gray');
    cref = round((0-cmin)/(cmax-cmin)*length(cmap));
    if cref < 1, cref = 1; end
    refcolor = cmap(cref,:);
    % widen field of view to match JMR paper
    if drawcirc, hold on;
         circle(0,0,100*d/2,'-r','LineWidth',2); end
    axis([-6, 6, -6, 6]); axis ij;
    set(gca, 'Color', refcolor);
    xlabel('x (cm)'); ylabel('y (cm)');
    title('SR: % signal magnitude change per voxel');
    fprintf(fid, '%s\n', ['SR plot compare data:']);
    LEIcompare(S, -0.40, XX, YY, d/2, 0, 0, 'circle');
end

%% Plot time-dependent dynamics

if timedep
    % Plot mean velocity in clipped circular phantom over
    % time
    figure;
    plot([0:dt:tmax]*1000,vm);
    axis([0, tmax*1000, 0, max(vm)*1.1]);
    xlabel('t (ms)'); ylabel('mean |v| (m/s)');
```

```
title('mean velocity over time');
[val ind] = max(vm);
text(tt(ind)*1000,val, ...
     ['vmean = ' num2str(val) ' m/s']);

% Plot max velocity in clipped circular phantom over
% time
figure;
plot([0:dt:tmax]*1000,vv);
axis([0, tmax*1000, 0, max(vv)*1.1]);
xlabel('t (ms)'); ylabel('max |v| (m/s)');
title('max velocity over time');
[val ind] = max(vv);
text(tt(ind)*1000,val,['vmax = ' num2str(val) ' m/s']);

% Plot mean distance in clipped circular phantom over
% time
figure;
plot([0:dt:tmax]*1000,dm);
axis([0, tmax*1000, 0, max(dm)*1.1]);
xlabel('t (ms)'); ylabel('mean |d| (m)');
title('mean displacement over time');
[val ind] = max(dm);
text(tt(ind)*1000,val,['dmean = ' num2str(val) ' m']);

% Plot max distance in clipped circular phantom over
% time
figure;
plot([0:dt:tmax]*1000,dd);
axis([0, tmax*1000, 0, max(dd)*1.1]);
xlabel('t (ms)'); ylabel('max |d| (m)');
title('max displacement over time');
[val ind] = max(dd);
text(tt(ind)*1000,val,['dmax = ' num2str(val) ' m']);

% Plot mean phi in clipped circular phantom over time
figure;
plot([0:dt:tmax]*1000,pm);
axis([0, tmax*1000, min(pm)*1.1, max(pm)*1.1]);
xlabel('t (ms)'); ylabel('mean \phi (rad)');
title('mean phi over time');
[val ind] = max(pm);
text(tt(ind)*1000,val, ...
     ['pmean = ' num2str(val) ' rad']);
```

```
    % Plot max phi in clipped circular phantom over time
    figure;
    plot([0:dt:tmax]*1000,pp);
    axis([0, tmax*1000, min(pp)*1.1, max(pp)*1.1]);
    xlabel('t (ms)'); ylabel('max \phi (rad)');
    title('max phi over time');
    [val ind] = max(pp);
    text(tt(ind)*1000,val,['pmax = ' num2str(val) ' rad']);
end

%% Display images of signal and related parameters

if plotextra
    % Display MRI phase "flow" Image
    figure;
    imageFOV(SP, XX*100, YY*100, 12, 12, 0, 0, 0);
    [cmin cmax] = caxis; axis square;
    colorbar; cmap = colormap('gray');
    cref = round((0-cmin)/(cmax-cmin)*length(cmap));
    if cref < 1, cref = 1; end
    refcolor = cmap(cref,:);
    % widen field of view to match JMR paper
    axis([-6, 6, -6, 6]); axis ij;
    set(gca, 'Color', refcolor);
    xlabel('x (cm)'); ylabel('y (cm)');
    title('<M/M_0> signal phase per voxel');
    if drawcirc, hold on;
         circle(0,0,100*d/2,'-r','LineWidth',2); end

    % Display MRI Signal image in full square phantom
    % domain
    H5 = figure;
    imageFOV(exbound(S*100,XX,YY,d/2,0,0,'circle',0), ...
         XX*100, YY*100, 12, 12, 0, 0, 0);
    % narrow scale to 40% of maximum to match JMR paper
    caxis([-40, 40]);
    [cmin cmax] = caxis; axis square;
    colorbar; cmap = colormap('gray');
    cref = round((0-cmin)/(cmax-cmin)*length(cmap));
    if cref < 1, cref = 1; end
    refcolor = cmap(cref,:);
    % widen field of view to match JMR paper
    if drawcirc, hold on;
```

```
         circle(0,0,100*d/2,'-r','LineWidth',2); end
    axis([-6, 6, -6, 6]); axis ij;
    set(gca, 'Color', refcolor);
    xlabel('x (cm)'); ylabel('y (cm)');
    title('SR: % signal magnitude change per voxel');
    if (runopt ~= 2)
        saveas(H5,[sprintf(plotfile), ...
             '_SRsquare.fig'],'fig')
        saveas(H5,[sprintf(plotfile), ...
             '_SRsquare.png'],'png')
        fprintf(fid, '%s\n', ['signal plot saved to: ', ...
            plotfile '_SRsquare']);
    end
end

% Display MRI Signal Image, in clipped circular phantom
% domain
SD = exbound(S, XX, YY, d/2, 0, 0, 'circle', 0)*100;
fprintf(fid, '%s\n', ['SD(Min,Mean,Max): (', ...
     num2str(min(SD(:))) ',', ...
     num2str(mean(SD(:))) ',' num2str(max(SD(:))) ')']);

H6 = figure;
imageFOV(SD, XX*100, YY*100, 12, 12, 0, 0, 0);
% narrow scale to 40% of maximum to match JMR paper
caxis([-40, 40]);
[cmin cmax] = caxis; axis square;
colorbar; cmap = colormap('gray');
cref = round((0-cmin)/(cmax-cmin)*length(cmap));
if cref < 1, cref = 1; end
refcolor = cmap(cref,:);
% widen field of view to match JMR paper
if drawcirc, hold on;
     circle(0,0,100*d/2,'-r','LineWidth',2); end
axis([-6, 6, -6, 6]); axis ij; set(gca, 'Color', refcolor);
xlabel('x (cm)'); ylabel('y (cm)');
title('SR: % signal magnitude change per voxel');
if (runopt ~= 2)
    saveas(H6,[sprintf(plotfile) '_SR.fig'],'fig')
    saveas(H6,[sprintf(plotfile) '_SR.png'],'png')
    fprintf(fid, '%s\n', ['signal plot saved to: ', ...
        plotfile '_SR']);
end
```

```
% Display Image of PH (mean phase shift per voxel)
if plotextra
    PH = ang2(PH);
    H7 = figure;
    imageFOV(exbound(PH,XX,YY,d/2,0,0,'circle',0), ...
         XX*100, YY*100, 12, 12, 0, 0, 0);
    caxis([min(PH(:)), max(PH(:))]);
    [cmin cmax] = caxis; axis square;
    colorbar; cmap = colormap('gray');
    cref = round((0-cmin)/(cmax-cmin)*length(cmap));
    if cref < 1, cref = 1; end
    refcolor = cmap(cref,:);
    % widen field of view to match JMR paper
    axis([-6, 6, -6, 6]); axis ij;
    set(gca, 'Color', refcolor);
    if drawcirc, hold on;
         circle(0,0,100*d/2,'-r','LineWidth',2); end
    xlabel('x (cm)'); ylabel('y (cm)');
    title('PH: mean phase shift per voxel (rad)');
    if (runopt ~= 2)
        saveas(H7,[sprintf(plotfile) '_PH.fig'],'fig')
        saveas(H7,[sprintf(plotfile) '_PH.png'],'png')
        fprintf(fid, '%s\n', ...
             ['PH plot saved to: ' plotfile '_PH']);
    end
end

if PTT
    if plotextra
    % Report ND values in the clipped circular phantom
    % domain
    [NC, N] = exbound(ND, XX, YY, d/2, 0, 0, 'circle', 0);
    IDD = find(NC > 0); NC(IDD) = 0;
    fprintf(fid,'%s\n',['ND2(Min,Mean,Max): (', ...
         num2str(100*min(NC(:))), ',', ...
         num2str(100*sum(NC(:))/N) ',', ...
         num2str(100*max(NC(:))) ')']);

    % Image of ND in the clipped circular phantom domain
    H92 = figure;
    imageFOV(NC*100, XX*100, YY*100, 12, 12, 0, 0, 0);
    caxis([-40 40]);
    [cmin cmax] = caxis; axis square;
    colorbar; cmap = colormap('gray');
```

```
    cref = round((0-cmin)/(cmax-cmin)*length(cmap));
    if cref < 1, cref = 1; end
    refcolor = cmap(cref,:);
    % widen field of view to match JMR paper
    axis([-6, 6, -6, 6]); axis ij;
    set(gca, 'Color', refcolor);
    if drawcirc, hold on;
         circle(0,0,100*d/2,'-r','LineWidth',2); end
    xlabel('x (cm)'); ylabel('y (cm)');
    title('ND2: % difference in number of particles, ...
         per voxel');
    if (runopt ~= 2)
         saveas(H92,[sprintf(plotfile) '_ND2.fig'],'fig')
         saveas(H92,[sprintf(plotfile) '_ND2.png'],'png')
         fprintf(fid, '%s\n', ['ND2 plot saved to: ', ...
         plotfile '_ND2']);
    end
    end
end

if plotextra
    [DD, N] = exbound(DD,XX,YY,d/2,0,0,'circle',0);
    % Display Image of DD in full square phantom domain
    % (mean displacements per voxel)
    H10 = figure;
    imageFOV(DD, XX*100, YY*100, 12, 12, 0, 0, 0);
    caxis([min(DD(:)), max(DD(:))]);
    [cmin cmax] = caxis; axis square;
    colorbar; cmap = colormap('gray');
    cref = round((0-cmin)/(cmax-cmin)*length(cmap));
    if cref < 1, cref = 1; end
    refcolor = cmap(cref,:);
    % widen field of view to match JMR paper
    axis([-6, 6, -6, 6]); axis ij;
    set(gca, 'Color', refcolor);
    if drawcirc, hold on;
        circle(0,0,100*d/2,'-r','LineWidth',2); end
    xlabel('x (cm)'); ylabel('y (cm)');
    title('DD: mean distances traveled per voxel (m)');
    if (runopt ~= 2)
        saveas(H10,[sprintf(plotfile) '_DD.fig'],'fig')
        saveas(H10,[sprintf(plotfile) '_DD.png'],'png')
        fprintf(fid, '%s\n', ['DD plot saved to: ', ...
            plotfile '_DD']);
```

```
    end
end

%% Save workspace
save([outputfile '.mat']); fprintf(fid, '%s\n', ...
     ['workspace saved to: ' outputfile '.mat']);
fprintf(fid, '%s\n', ['completed run time: ', ...
     s2hms(loadtime + toc)]);
fprintf(fid, '%s\n', ['estimated run time: ', ...
     s2hms(runtime)]);
if runopt == 0, fclose(fid); end  % close displayfile
diary off;     % close diary
disp('DONE!');
end % End function MHD_Square
```

MHD_SquareTimed.m

```
%% MHD_SquareTimed.m
% simplified iteration of MHD_Square for estimating
% simulation run time

j = 1; l = 0; t=0;
% EM force correction %%%%%%%%%%%%%%%%%%%%%%%%%%%%%%%%%%%%%%%%%%%%
if FTT
    % first order model
    % v = E x B / B2 = [vx = Ey*Bz; vy = -Ex*Bz]
    % v = J x B
    % J = sigma*(E + v x B)
    % fx = +Bz*sig*(Ey(:,2:end-1) - Bz*vx);
    % fy = -Bz*sig*(Ex(2:end-1,:) + Bz*vy);
    % fx is a small negative number dominated by -Bz*vx
    % fy is a large negative number dominated by Ex
    Jx = sig*(Ex(2:(end-1),:) + Cb*Bz*vy);
    Jy = sig*(Ey(:,2:(end-1)) - Cb*Bz*vx);
    % f = J x B volume Lorentz force on conducting fluid
    fx = Bz*Jy;
    fy = -Bz*Jx;
end

% initial velocity at each time step
vxo = [uW' vx uE'];
vyo = [vS; vy; vN];
% compute velocity at the end of each time step
% Navier-Stokes SIMPLE Method
% treat nonlinear terms
gamma = min(1.2*dt*max(max(abs(vx(:))) / ...
    dx,max(abs(vy(:)))/dy),1);
Ue = [2*uS-vxo(1,:); vxo; 2*uN-vxo(end,:)];
Ve = [2*vW'-vyo(:,1) vyo 2*vE'-vyo(:,end)];
Ua = avg(Ue);
Ud = diff(Ue,1,1)/2;
Va = avg(Ve')';
Vd = diff(Ve,1,2)/2;
UVx = diff(Ua.*Va-gamma*abs(Ua).*Vd,1,2)/dx;
UVy = diff(Ua.*Va-gamma*Ud.*abs(Va),1,1)/dy;

Ua = avg(Ue(2:end-1,:)')';
Ud = diff(Ue(2:end-1,:),1,2)/2;
```

```
Va = avg(Ve(:,2:end-1));
Vd = diff(Ve(:,2:end-1),1,1)/2;

U2x = diff(Ua.^2-gamma*abs(Ua).*Ud,1,2)/dx;
V2y = diff(Va.^2-gamma*abs(Va).*Vd,1,1)/dy;

% update velocity due to convective acceleration
if FTT
    vx = vx-dt*(UVy(:,2:end-1)+U2x) + Cf*fx;
    vy = vy-dt*(UVx(2:end-1,:)+V2y) + Cf*fy;
else
    vx = vx-dt*(UVy(:,2:end-1)+U2x);
    vy = vy-dt*(UVx(2:end-1,:)+V2y);
end

% update velocity due to implicit viscosity
% vectorize matrices, compute cholesky solution to inverse
% problem
rhs = reshape(vx+Ubc,[],1);
u(peru) = Ru\(Rut\rhs(peru));
vx = reshape(u,ny,nx-1);

rhs = reshape(vy+Vbc,[],1);
v(perv) = Rv\(Rvt\rhs(perv));
vy = reshape(v,ny-1,nx);

% Pressure correction by solving linear system from Poisson
% Equation
% -Laplacian(P)/pf = -(1/dt)*grad(v)
rhs = reshape(diff([uW' vx uE'],1,2)/dx+diff([vS; vy;
vN],1,1)/dy,[],1)/Cp;
rhs(WP) = [];
p2(perp) = -Rp\(Rpt\rhs(perp));
p(NP) = p2; p(WP) = 0;
P = reshape(p,ny,nx);
vx = vx-Cp*diff(P,1,2)/dx;
vy = vy-Cp*diff(P,1,1)/dy;

if ~FTT
    Jx = sig*(Ex(2:(end-1),:) + Cb*Bz*vy);
    Jy = sig*(Ey(:,2:(end-1)) - Cb*Bz*vx);
    % f = J x B Lorentz force on a conducting fluid
    fx = Bz*Jy;
    fy = -Bz*Jx;
```

```
    % Update velocity due to EM force
    vx = vx+Cf*fx;
    vy = vy+Cf*fy;
end

if PTT
    %%%%%%%%%%%%%%%%%%%%%%%%%%%%%%%%%%%%%%%%%%%%%%%%%%%%%%%%%%%%
    % Compute mean velocity and distance traveled
    % vm = mean velocity per time step at each point
    vxm = ([uW' vx uE']+vxo)/2;
    vym = ([vS; vy; vN]+vyo)/2;
    % Compute distance traveled for each water molecule
    % based on location
    % within voxel using linear approximation
    % D = (vi + vf)/2*dt
    XI = fix((xc+d/2-eps*10)/dx)+1;
    YI = fix((yc+d/2-eps*10)/dy)+1;
    xrem = rem((xc+d/2),dx)/dx;
    yrem = rem((yc+d/2),dy)/dy;
    ddx = dt*(xrem.*vxm(YI+ny*XI) + ...
        (1-xrem).*vxm(YI+ny*(XI-1)));
    ddy = dt*(yrem.*vym(YI+1+(ny+1)*(XI-1)) + ...
        (1-yrem).*vym(YI+(ny+1)*(XI-1)));

    % Limit water to region inside square %%%%%%%%%%
    % Compute phase from xo, yo and update xc, yc
    xo = xc; yo = yc;
    xc = xc + ddx; yc = yc + ddy;
    K2 = find( (abs(xc) > (d/2-eps)) | ...
        (abs(yc) > (d/2-eps)) );
    if ~isempty(K2)
        % bounce water off boundary (inelastic, deflect
        % distance = eps)
        % determine intersection of trajectory and circle
        deltax = ddx(K2);
        deltay = ddy(K2);
        xoo = xo(K2);
        yoo = yo(K2);
        xi = xc(K2);
        yi = yc(K2);
        mi = deltay./deltax;          % slope
        bi = yoo - mi.*xoo;           % intercept
        IS = abs(deltax) <= eps;      % infinite slope index
```

```
    % if infinite slope
    K4 = find(IS);
    yi(K4) = sign(deltay(K4))*(d/2-eps);
    xi(K4) = xoo(K4);

    % wrong intersection
    KW = find(abs(xi(K4)) > (d/2-eps));
    xi(K4(KW)) = sign(deltax(K4(KW)))*(d/2-eps);
    yi(K4(KW)) = [mi(K4(KW)).*xi(K4(KW))+bi(K4(KW))];

    % if non-infinite slope
    K3 = find(~IS);
    xi(K3) = sign(deltax(K3))*(d/2-eps);
    yi(K3) = [mi(K3).*xi(K3)+bi(K3)];

    % wrong intersection
    KW = find(abs(yi(K3)) > (d/2-eps));
    yi(K3(KW)) = sign(deltay(K3(KW)))*(d/2-eps);
    xi(K3(KW)) = [(yi(K3(KW))-bi(K3(KW)))./mi(K3(KW))];

    % determine incidence (a) and
    % intersection (theta) angles
    % resultant angle (rang) is in opposite direction
    % of motion
    % rang = pi + 2*theta - a
    if bounce
        rang = pi+(2*atan2(yi,xi) - ...
            atan2(deltay,deltax));
    else
        rang = pi+atan2(yi,xi);
    end
    xc(K2) = xi+eps.*cos(rang);
    yc(K2) = yi+eps.*sin(rang);

    % update differential displacement
    ddx(K2) = xc(K2) - xoo;
    ddy(K2) = yc(K2) - yoo;
end

K3 = find( (abs(xc) > (d/2-eps)));
xc(K3) = sign(xc(K3))*d/2;
K4 = find( (abs(yc) > (d/2-eps)));
yc(K4) = sign(yc(K4))*d/2;
```

```
    % Display warning when correcting out of bounds error
    if ( ~isempty(K3) || ~isempty(K4) )
        fprintf(fid, '%s\n',
            ['warning out of bounds: past xlim = ' ...
            num2str(length(K3)) ', past ylim = ', ...
            num2str(length(K4)), ' at t = ', ...
            num2str(t*1000) 'msec']);
    end
end

%% Compute phase accumulating over each time step
%  ph = ph + g*dt*(Gx*xc+Gy*yc);
if PTT
    ph = ph + g*dt*(Gx*(xc-ddx/2)+Gy*(yc-ddy/2));
    % nwr x nwc
    dmag = sqrt((xc(:)-xw(:)).^2 + (yc(:)-yw(:)).^2);
else
    % include boundary nodes
    vxm = [uW' vx uE'];
    vym = [vS; vy; vN];
    [phdx,phdy] = gradient(ph,dx,dy);
    ph = ph + dt*(g*(Gx*xw+Gy*yw) + ...
        phdx.*avg(vxm')'+phdy.*avg(vym));
end

% store average and max velocity, displacement, and phase
Vx = avg([uS; [uW' vx uE']; uN]);
Vy = avg([vW' [vS; vy; vN] vE']')';
vmag = sqrt(Vx(:).^2 + Vy(:).^2);   % ny+1 x nx+1

% Determine lobe parameters
LEx = diff(Ex,1,2)/dx;
LEy = diff(Ey,1,1)/dy;
qo(2:(end-1),2:(end-1)) = qo(2:(end-1),2:(end-1)) -
dt*sig*(LEx(2:(end-1),:) + LEy(:,2:(end-1)));

% rhs contributions of qo and removed dirichlet nodes from
% Phi and qo
% Solve for initial potentials
rhs = -PhiB;
rhs([WN EN]) = [];
% rhs = reshape(qo'/eo/er,[],1)+PhiB;
PhiM(perM) = RM\(RMt\rhs(perM));
```

```
% place back in dirichlet potentials
Phi(NN) = PhiM; Phi(WN) = PhiW; Phi(EN) = PhiE;
Phi2 = reshape(Phi,ny+1,nx+1);

qo = zeros(size(Phi2));
QMEAN = mean(abs(qo(:)));
PMEAN = mean(abs(Phi2(:)));

% Reset Electric Fields
Ex = -diff(Phi2,1,2)/dx;   % (V/m) stimulus (91x90)
Ey = -diff(Phi2,1,1)/dy;   % (V/m) stimulus (90x91)

% reset initial velocities and positions
vx = zeros(ny,nx-1);   % (m/s) velocity (90x89)
vy = zeros(ny-1,nx);   % (m/s) velocity (89x90)
ph = zeros(size(xw));
if PTT
    PHI1a = ph;
    PHI1b = ph;
    PHIna = ph;
    PHInb = ph;
    % store gradient interval locations
    XCWi = xw; YCWi = yw;
    % set current locations
    xc = xw; yc = yw;
    xi = xw; yi = yw;
    XI = xw; YI = yw;
end
```

avg.m

```
function B = avg(A,k)
% function B = avg(A,k)
% computes average values for vertical midway points of
% meshgrid matrix A

% if k <= 1
if nargin<2, k = 1; end

% if row vector, make column vector
if size(A,1)==1, A = A'; end

% if k > 1
if k<2, B = (A(2:end,:)+A(1:end-1,:))/2;
else B = avg(A,k-1); end

% if A was originally a column vector, return a row vector
if size(A,2)==1, B = B'; end
```

K1.m

```
function A = K1(n,h,bc)
% function A = K1(n,h,bc)
% bc = boundary conditions:
%      Neumann=1, Dirichlet=2, Dirichlet mid=3;
% forms connectivity matrix

A = spdiags([-1 a11 0;ones(n-2,1)*[-1 2 -1]; ...
    0 a11 -1],-1:1,n,n)'/h^2;
```

rsize.m

```
function B = rsize(A,nx,ny)
% function B = rsize(A,nx,ny)
% resizes a matrix to new dimensions nx,ny by clipping off
% the first and last row(s) / column(s)
% or by adding on

[i,j] = size(A);
bx = floor((nx-i)/2);
by = floor((ny-j)/2);
rx = mod(nx-i,2);
ry = mod(ny-j,2);
if (bx < 0)
   B = A((1-bx):(i+bx),:);
else
   B = [zeros(bx,j); A; zeros(bx,j)];
end
if (by < 0)
   B = B(:,(1-by):(j+by));
else
   B = [zeros(i+2*bx,by) B zeros(i+2*bx,by)];
end
B = [B; zeros(rx,j+2*by)];B = [B zeros(i+2*bx+rx,ry)];
```

ang2.m

```
function p2 = ang2(p1)
% function p2 = ang2(p1)
% Returns vector angle (in radians) between -pi and pi

p2 = rem(p1,2*pi);
% if p2 > +pi; p2 = p2 - 2*pi; end
% if p2 < -pi; p2 = p2 + 2*pi; end
pu = find(p2 > +pi); pd = find(p2 < -pi);
p2(pu) = p2(pu) - 2*pi;
p2(pd) = p2(pd) + 2*pi;
```

circle.m

```
function circle(xo,yo,r,varargin)
% function circle(xo,yo,r,varargin)
% plot a circle based on input style parameters
% x and y are the coordinates of the center of the circle
% r is the radius of the circle
% 0.01 is the angle step, bigger values will draw the
% circle faster but will not be as smooth

if nargin < 3
    disp('circle: not enough input arguments');
    return;
end
if nargin < 4, styles = ':k'; else styles = varargin; end

ang = 0:0.01:2*pi;
xp = r*cos(ang);
yp = r*sin(ang);

% plot the circle
plot(xo+xp,yo+yp,styles{:});
```

exbound.m

```
function [M, N] = exbound(M, X, Y, r, x0, y0, bound, value)
% function [M, N] = exbound(M, X, Y, r, x0, y0, bound,
% value)
% exclude image pixles outside of a boundary object
%
% edits image matrix M, with meshgrid coordinates X, Y
% by determining which image pixels are outside of a
% boundary object and assigns them a specified value
% (default = zero)
% Also returns N, the number of pixels within the bounds
%
% Optional Inputs:
% x0, y0 = center of boundary object (default = [0,0])
% bound = boundary object shape: 'square' or 'circle'
% ('circle' = default)
% value = double precision number (default = 0)
%
% Required Inputs:
% X, Y = meshgrid coordinates for image matrix
% M = image pixel values
% r = boundary object radius (or half width)

if nargin < 4
    warning('exbound:insufficientInputs', ...
        'exbound: insufficient input arguments, aborting');
    help('exbound');
    return;
end

if sum(size(X) ~= size(M)) + sum(size(Y) ~= size(M)) > 0,
    warning('exbound:matrixSizeMismatch', ...
        'exbound: M, X, and Y, size mismatch, aborting');
    return;
end

if nargin < 6, x0 = 0; y0 = 0; end
if nargin < 7, bound = 'circle'; end
if nargin < 8, value = 0; end

% exclude pixels of M that are outside of boundary object
if bound == 'square'
```

```
    I = find((abs(X-x0) > r)||abs((Y-y0) > r));
else
    bound = 'circle';
    I = find((X-x0).^2 + (Y-y0).^2 > r^2);
end
N = numel(M) - numel(I);
M(I) = value;
```

imageFOV.m

```
function [M2,X,Y] = imageFOV(M,X,Y,xb,yb,x0,y0,value)
% function [M2, X, Y] = imageFOV(M,X,Y,xb,yb,x0,y0,value)
% clip or place image object within a square FOV
%
% edits image matrix M, with meshgrid coordinates X, Y
% by determining resolution of image and padding with
% pixels and assigns them a specified value (default = 0)
%
% Optional Inputs:
% x0, y0 = center of imaged object (default = [0,0])
% value = double precision number for padded pixels
% (default = 0)
%
% Required Inputs:
% M = image pixel values
% X, Y = meshgrid coordinates for image matrix
% [xb, yb] = FOV dimensions

if nargin < 4,
    warning('expandFOV:insufficient_inputs', ...
      'expandFOV: insufficient input arguments, aborting');
    help('expandFOV');
    return;
end
if sum(size(X) ~= size(M)) + sum(size(Y) ~= size(M)) > 0,
    warning('expandFOV:matrixSizeMismatch', ...
      'expandFOV: M, X, and Y, size mismatch, aborting');
    help('expandFOV');
    return;
end
% assume same FOV bound for both dimensions
if nargin < 5, yb = xb; end
if (xb < 0), xb = -xb; end
if (yb < 0), yb = -yb; end
% assume object centered at 0,0
if nargin < 7, x0 = 0; y0 = 0; end
if nargin < 8, value = 0; end

%% determine image resolution and bounds
dx = X(1,2) - X(1,1);
if (dx < 0), dx = -dx; X = fliplr(X); M = fliplr(M); end
```

```
dy = Y(2,1) - Y(1,1);
if (dy < 0), dy = -dy; Y = flipud(Y); M = flipud(M); end

Xmin = min(X(1,:)); Xmax = max(X(1,:)); XL = Xmax - Xmin;
Ymin = min(Y(:,1)); Ymax = max(Y(:,1)); YL = Ymax - Ymin;

if (min(X(:)) ~= Xmin)||(max(X(:)) ~= Xmax)
    warning('expandFOV:non-meshgrid', ...
        'expandFOV: X is not a meshgrid');
    help('expandFOV');
    return;
end
if (min(Y(:)) ~= Ymin)||(max(Y(:)) ~= Ymax)
    warning('expandFOV:non-meshgrid', ...
        'expandFOV: X is not a meshgrid');
    help('expandFOV');
    return;
end

%% Setup FOV matrix
x = (-xb/2):dx:(xb/2);
y = (-yb/2):dy:(yb/2);
if (XL > xb)
    warning('expandFOV:object_xbounds', ...
      ['expandFOV: object x-dim greater than FOV', ...
       ', clipping will occur']);
end
if (YL > yb)
    warning('expandFOV:object_ybounds', ...
      ['expandFOV: object y-dim greater than FOV', ...
       ', clipping will occur']);
end

% find nearest x,y points for object center within FOV
[D,Ix0] = min(abs(x - x0)); x0 = x(Ix0);
[D,Iy0] = min(abs(y - y0)); y0 = y(Iy0);
% determine object bounds within FOV
Ixclipl = round( (min(x)-(x0-XL/2))/dx );
Ixclipu = round( ((x0+XL/2)-max(x))/dx );
Iyclipl = round( (min(y)-(y0-YL/2))/dy );
Iyclipu = round( ((y0+YL/2)-max(y))/dy );

%% Place object within FOV
% clip object image to fit within FOV
```

```
if( Ixclipl > 0 )
    warning('expandFOV:xlowerbound', ...
      ['expandFOV: object outside FOV x-lower bound', ...
       ', clipping object']);
    X(:,1:Ixclipl) = []; M(:,1:Ixclipl) = []; Ixclipl = 0;
else Ixclipl = -Ixclipl; end
if( Ixclipu > 0 )
    warning('expandFOV:xupperbound', ...
      ['expandFOV: object outside FOV x-upper bound', ...
      ', clipping object']);
    X(:,(end-Ixclipu+1):end) = []; M(:,(end-Ixclipu+1):end)
= []; Ixclipu = 0;
else Ixclipu = -Ixclipu; end
if( Iyclipl > 0 )
    warning('expandFOV:ylowerbound', ...
      ['expandFOV: object outside FOV y-lower bound', ...
       ', clipping object']);
    Y(1:Iyclipl,:) = []; M(1:Iyclipl,:) = []; Iyclipl = 0;
else Iyclipl = -Iyclipl; end
if( Iyclipu > 0 )
    warning('expandFOV:yupperbound', ...
      ['expandFOV: object outside FOV y-upper bound', ...
      ', clipping object']);
    X((end-Iyclipu+1):end,:) = [];
    M((end-Iyclipu+1):end,:) = [];
    Iyclipu = 0;
else
    Iyclipu = -Iyclipu;
end

[nr,nc] = size(M);
[X,Y] = meshgrid(x,y);
if (value == 0)
    M2 = zeros(size(X))
Else
    M2 = value*ones(size(X));
end
M2([(Iyclipl+1):(Iyclipl+nr)], ...
   [(Ixclipl+1):(Ixclipl+nc)]) = M;

% Display clipped image
imagesc(x,y,M2);
```

LEIcompare.m

```
function LEIcompare(S, thresh, X, Y, r, x0, y0, bound)
% function LEIcompare(S, thresh, X, Y, r, x0, y0, bound)
% Compute LEI inter-image comparison statistics for image
% matrix SD
% Show S min, mean, max within field of view
% Quantify area of signal loss based on an inter-image
% comparison with predefined threshold
% Quadrant-based sum of total signal and SRLT to indicate
% symmetry
% default thresh = 40;

if nargin < 1
    error('LEIcompare', ...
        'LEIcompare: not enough input args');
    return;
else
    exb = 1;
    [nr, nc] = size(S);
end
if nargin < 2, thresh = -0.40; end
if nargin < 4
    x = linspace(-nc/2,nc/2,nc);
    y = linspace(-nr/2,nr/2,nr);
    [X, Y] = meshgrid(x,y);
end
if nargin < 5, exb = 0; N = numel(S); r = nc; end
if nargin < 7, x0 = 0; y0 = 0; end
if nargin < 8, bound = 'circle'; end

if exb, [S, N] = exbound(S, X, Y, r, x0, y0, bound, 0); end
disp('-----------------------------------');
disp('- Inter-image compare statistics -');
disp([' SD(min, mean, max): ', ...
    num2str(100*min(S(:))) ', ', ...
    num2str(100*sum(S(:))/N), ...
    ', ' num2str(100*max(S(:))), ')']);

%% Quadrant comparison
% Extract image parameters for quadrant comparison

% Compute relative S per quadrant
```

```
A1 = sum(S(find( (X(:) <= x0) & (Y(:) <= y0) )));
A2 = sum(S(find( (X(:) >= x0) & (Y(:) <= y0) )));
A3 = sum(S(find( (X(:) >= x0) & (Y(:) >= y0) )));
A4 = sum(S(find( (X(:) <= x0) & (Y(:) >= x0) )));
ATOT = (A1 + A2 + A3 + A4)/100;
disp(['A1: ', num2str(A1/ATOT) '%']);
disp(['A2: ', num2str(A2/ATOT) '%']);
disp(['A3: ', num2str(A3/ATOT) '%']);
disp(['A4: ', num2str(A4/ATOT) '%']);

% Compute SRLT: percentage of S area <= thresh
S = (S <= thresh);
disp(['area of SD <= thresh: ',...
    num2str(100*sum(S(:))/N) '%']);
A1 = sum(S(find( (X(:) <= x0) & (Y(:) <= y0) )));
A2 = sum(S(find( (X(:) >= x0) & (Y(:) <= y0) )));
A3 = sum(S(find( (X(:) >= x0) & (Y(:) >= y0) )));
A4 = sum(S(find( (X(:) <= x0) & (Y(:) >= x0) )));
ATOT = (A1 + A2 + A3 + A4)/100;
disp(['A1<t: ', num2str(A1/ATOT) '%']);
disp(['A2<t: ', num2str(A2/ATOT) '%']);
disp(['A3<t: ', num2str(A3/ATOT) '%']);
disp(['A4<t: ', num2str(A4/ATOT) '%']);
disp('-----------------------------------');
```

dispimg.m

```
%% dispimg.m
% Load raw signal data from MRI experiment file 'img'
% Display MRI Signal Image, clip into circle
% Analyze reformatted image

if ~exist('img');
    load('img.mat');
end
plotfile = ['ImgFig'];
rsize = size(img,2);
csize = size(img,1);
nsize = size(img,3);
FOV = 0.12;  % m
d = 0.10;    % m
drawcirc = 1;
saveimage = 0;

I = [0 0.1 0.2 0.5 1 2 5 -0.1 -0.2 -0.5 -1 -2 -5];

fid = 1;
exb = 1;

dx = FOV/csize;
dy = FOV/rsize;
xl = (-FOV/2+dx/2):dx:(FOV/2-dx/2);
yl = (-FOV/2+dy/2):dy:(FOV/2-dy/2);
[XX,YY] = meshgrid(xl,yl);
SO = img(:,:,1)';

if exb
    [SO, N] = exbound(SO, XX, YY, d/2, 0, 0, 'circle', 0);
    mS = sum(SO(:))/N;
else
    mS = mean(SO(:));
end

for fignum = 1:nsize
    plotfile = ['Fig3_' num2str(fignum)];
    disp(['Loading image for ' plotfile ', ...
        I = ' num2str(I(fignum)) ' mA']);
    if exb, SD = exbound(img(:,:,fignum)', ...
```

```
            XX, YY, d/2, 0, 0, 'circle', 0);
    else SD = img(:,:,fignum)';
    end
    SD = (SD-SO)/mS;

    H4 = figure; imagesc(xl*100,yl*100,SD*100);
    % narrow scale to 40% of maximum to match JMR paper
    % caxis([min(S(:))*0.40, max(S(:))*0.40]);
    caxis([-40, 40]);
    [cmin cmax] = caxis; axis square;
    colorbar; cmap = colormap('gray');
    cref = round((0-cmin)/(cmax-cmin)*length(cmap));
    if cref < 1, cref = 1; end
    refcolor = cmap(cref,:);
    % widen field of view to match JMR paper
    axis([-6, 6, -6, 6]); set(gca, 'Color', refcolor);
    xlabel('x (cm)'); ylabel('y (cm)');
    title('SR: % signal magnitude change per voxel');
    if drawcirc
        hold on;
        circle(0,0,100*d/2,'-r','LineWidth',2);
    end
    if saveimage
        saveas(H4,[sprintf(plotfile) '_SR.fig'],'fig')
        saveas(H4,[sprintf(plotfile) '_SR.png'],'png')
        fprintf(fid, '%s\n', ...
             ['signal plot saved to: ' plotfile '_SR']);
    end
    if exb
        fprintf(fid, '%s\n', ...
            ['SD(Min,Mean,Max): (', ...
            num2str(100*min(SD(:))), ',', ...
            num2str(100*sum(SD(:))/N), ',', ...
            num2str(100*max(SD(:))), ')']);
    else
        fprintf(fid, '%s\n', ...
            ['SD(Min,Mean,Max): (', ...
            num2str(100*min(SD(:))), ',', ...
            num2str(100*mean(SD(:))), ',', ...
            num2str(100*max(SD(:))), ')']);
    end
    LEIcompare(SD, -0.40, XX, YY, d/2, 0, 0, 'circle');
end
```

Works Cited

1. Bandettini, P.A., N. Petridou, and J. Bodurka, *Direct detection of neuronal activity with MRI: Fantasy, possibility, or reality?* Applied Magnetic Resonance, 2005. **29**(1): p. 65-88.

2. Purves, D., *Neuroscience*. 4th ed2008, Sunderland, Mass.: Sinauer. xvii, 857, G-16, IC-7, I-29 p.

3. Dale, A.M. and M.I. Sereno, *Improved Localization of Cortical Activity by Combining Eeg and Meg with Mri Cortical Surface Reconstruction - a Linear-Approach.* Journal of Cognitive Neuroscience, 1993. **5**(2): p. 162-176.

4. Jansen, B.H. and V.G. Rit, *Electroencephalogram and Visual-Evoked Potential Generation in a Mathematical-Model of Coupled Cortical Columns.* Biological Cybernetics, 1995. **73**(4): p. 357-366.

5. Ramon, C., P.H. Schimpf, and J. Haueisen, *Influence of head models on EEG simulations and inverse source localizations.* Biomed Eng Online, 2006. **5**: p. 10.

6. Kuruvilla, A. and R. Flink, *Intraoperative electrocorticography in epilepsy surgery: useful or not?* Seizure, 2003. **12**(8): p. 577-84.

7. Belliveau, J.W., et al., *Functional Mapping of the Human Visual-Cortex by Magnetic-Resonance-Imaging.* Science, 1991. **254**(5032): p. 716-719.

8. Hirsch, J., et al., *An Integrated Functional Magnetic Resonance Imaging Procedure for Preoperative Mapping of Cortical Areas Associated with Tactile, Motor, Language, and Visual Functions.* Neurosurgery, 2000. **47**(3): p. 711-722.

9. Miller, K.J., et al., *Real-time functional brain mapping using electrocorticography.* NeuroImage, 2007. **37**(2): p. 504-7.

10. Singh, M., S. Kim, and T.S. Kim, *Correlation between BOLD-fMRI and EEG signal changes in response to visual stimulus frequency in humans.* Magn Reson Med, 2003. **49**(1): p. 108-14.

11. Whittingstall, K., et al., *Correspondence of visual evoked potentials with FMRI signals in human visual cortex.* Brain Topogr, 2008. **21**(2): p. 86-92.

12. Dougherty, R.F., et al., *Visual field representations and locations of visual areas V1/2/3 in human visual cortex.* Journal of Vision, 2003. **3**(10): p. 586-598.

13. Huettel, S.A., A.W. Song, and G. McCarthy. *Functional magnetic resonance imaging*. [Table of contents] 2004; xviii, 492 p. ill. (chiefly col.) 29 cm. + 1 CD-ROM (4 3/4 in.)]. Available from: http://www.loc.gov/catdir/toc/ecip0413/2004000500.html.

14. Ogawa, S., et al., *Functional brain mapping by blood oxygenation level-dependent contrast magnetic resonance imaging. A comparison of signal characteristics with a biophysical model.* Biophys J, 1993. **64**(3): p. 803-12.

15. Logothetis, N.K., *The neural basis of the blood–oxygen–level–dependent functional magnetic resonance imaging signal.* Philosophical Transactions of the Royal Society of London. Series B: Biological Sciences, 2002. **357**(1424): p. 1003-1037.

16. Truong, T.K. and A.W. Song, *Finding neuroelectric activity under magnetic-field oscillations (NAMO) with magnetic resonance imaging in vivo.* Proc Natl Acad Sci U S A, 2006. **103**(33): p. 12598-601.

17. Roux, F.-E., et al., *Language Functional Magnetic Resonance Imaging in Preoperative Assessment of Language Areas: Correlation with Direct Cortical Stimulation.* Neurosurgery, 2003. **52**(6): p. 1335-1347 10.1227/01.NEU.0000064803.05077.40.

18. Logothetis, N.K., *What we can do and what we cannot do with fMRI.* Nature, 2008. **453**(7197): p. 869-878.

19. Attwell, D. and C. Iadecola, *The neural basis of functional brain imaging signals.* Trends Neurosci, 2002. **25**(12): p. 621-5.

20. Logothetis, N.K., et al., *Neurophysiological investigation of the basis of the fMRI signal.* Nature, 2001. **412**(6843): p. 150-157.

21. Jasanoff, A., *Bloodless fMRI.* Trends in Neurosciences, 2007. **30**(11): p. 603-610.

22. Xue, Y.Q., J.H. Gao, and J.H. Xiong, *Direct MRI detection of neuronal magnetic fields in the brain: Theoretical modeling.* NeuroImage, 2006. **31**(2): p. 550-559.

23. Cassara, A.M., et al., *Realistic simulations of neuronal activity: A contribution to the debate on direct detection of neuronal currents by MRI.* NeuroImage, 2008. **39**(1): p. 87-106.

24. Hagberg, G.E., M. Bianciardi, and B. Maraviglia, *Challenges for detection of neuronal currents by MRI.* Magn Reson Imaging, 2006. **24**(4): p. 483-93.

25. Xiong, J., P.T. Fox, and J.H. Gao, *Directly mapping magnetic field effects of neuronal activity by magnetic resonance imaging.* Hum Brain Mapp, 2003. **20**(1): p. 41-9.

26. Bodurka, J., et al., *Current-induced magnetic resonance phase imaging.* Journal of Magnetic Resonance, 1999. **137**(1): p. 265-271.

27. Petridou, N., et al., *Direct magnetic resonance detection of neuronal electrical activity.* Proceedings of the National Academy of Sciences, 2006. **103**(43): p. 16015-16020.

28. Kamei, H., et al., *Neuronal current distribution imaging using magnetic resonance.* Ieee Transactions on Magnetics, 1999. **35**(5): p. 4109-4111.

29. Park, T.S., et al., *Observation of the fast response of a magnetic resonance signal to neuronal activity: a snail ganglia study.* Physiol Meas, 2006. **27**(2): p. 181-90.

30. Park, T.S. and S.Y. Lee, *Effects of neuronal magnetic fields on MRI: numerical analysis with axon and dendrite models.* NeuroImage, 2007. **35**(2): p. 531-8.

31. Konn, D., P. Gowland, and R. Bowtell, *MRI detection of weak magnetic fields due to an extended current dipole in a conducting sphere: A model for direct detection of neuronal currents in the brain.* Magnetic Resonance in Medicine, 2003. **50**(1): p. 40-49.

32. Chow, L.S., et al., *Investigation of MR signal modulation due to magnetic fields from neuronal currents in the adult human optic nerve and visual cortex.* Magnetic Resonance Imaging, 2006. **24**(6): p. 681-691.

33. Chow, L.S., et al., *Investigation of axonal magnetic fields in the human corpus callosum using visual stimulation based on MR signal modulation.* Journal of Magnetic Resonance Imaging, 2007. **26**(2): p. 265-273.

34. Wijesinghe, R.S. and B.J. Roth, *Lorentz effect imaging of ionic currents in solution using correct values for ion mobility.* Journal of Magnetic Resonance, 2010. **204**(2): p. 225-227.

35. Wijesinghe, R.S. and B.J. Roth, *Detection of Peripheral Nerve and Skeletal Muscle Action Currents Using Magnetic Resonance Imaging.* Annals of Biomedical Engineering, 2009. **37**(11): p. 2402-2406.

36. Chow, L.S., et al., *Investigating direct detection of axon firing in the adult human optic nerve using MRI.* NeuroImage, 2006. **30**(3): p. 835-46.

37. Joy, M., G. Scott, and M. Henkelman, *In vivo detection of applied electric currents by magnetic resonance imaging.* Magn Reson Imaging, 1989. **7**(1): p. 89-94.

38. Scott, G.C., et al., *Measurement of Nonuniform Current-Density by Magnetic-Resonance.* Ieee Transactions on Medical Imaging, 1991. **10**(3): p. 362-374.

39. Hamalainen, M., et al., *Magnetoencephalography - Theory, Instrumentation, and Applications to Noninvasive Studies of the Working Human Brain.* Reviews of Modern Physics, 1993. **65**(2): p. 413-497.

40. Song, A.W. and A.M. Takahashi, *Lorentz effect imaging.* Magn Reson Imaging, 2001. **19**(6): p. 763-7.

41. Truong, T.K., J.L. Wilbur, and A.W. Song, *Synchronized detection of minute electrical currents with MRI using Lorentz effect imaging.* J Magn Reson, 2006. **179**(1): p. 85-91.

42. Truong, T.K., A. Avram, and A.W. Song, *Lorentz effect imaging of ionic currents in solution.* J Magn Reson, 2008. **191**(1): p. 93-9.

43. Pauling, L., *Magnetic properties and structure of oxyhemoglobin.* Proceedings of the National Academy of Sciences of the United States of America, 1977. **74**(7): p. 2612-2613.

44. Coyne, K. *MRI: A Guided Tour*. Magnet Academy [cited 2013 March 1].

45. Brown, M.A. and R.C. Semelka, *MRI : basic principles and applications*. Magnetic Resonance Imaging: Hoboken, N.J. : Wiley-Blackwell/John Wiley & Sons, c2010.

46. Bernstein, M.A., K.F. King, and Z.J. Zhou, *Handbook of MRI pulse sequences*2004, Amsterdam ; Boston: Academic Press. xxii,1017 p.

47. Basford, A.T., et al., *Lorentz-force-induced motion in conductive media.* Magn Reson Imaging, 2005. **23**(5): p. 647-51.

48. Muthupillai, R., et al., *Magnetic resonance elastography by direct visualization of propagating acoustic strain waves.* Science, 1995. **269**(5232): p. 1854-7.

49. Dresner, M.A., et al., *Magnetic resonance elastography of skeletal muscle.* J Magn Reson Imaging, 2001. **13**(2): p. 269-76.

50. Kruse, S.A., et al., *Tissue characterization using magnetic resonance elastography: preliminary results.* Phys Med Biol, 2000. **45**(6): p. 1579-90.

51. Wu, T., et al., *Assessment of thermal tissue ablation with MR elastography.* Magn Reson Med, 2001. **45**(1): p. 80-7.

52. Roth, B.J. and P.J. Basser, *Mechanical Model of Neural Tissue Displacement During Lorentz Effect Imaging.* Magnetic Resonance in Medicine, 2009. **61**(1): p. 59-64.

53. Wolynes, P.G., *Dynamics of Electrolyte-Solutions.* Annual Review of Physical Chemistry, 1980. **31**: p. 345-376.

54. Meton, M. and P. Gerard, *Hall-Effect in Dilute Electrolytes.* Chemical Physics Letters, 1976. **44**(3): p. 582-585.

55. Friedman, H.L., *Calculation of Hall Effect in Ionic Solutions.* Journal of Physical Chemistry, 1965. **69**(8): p. 2617-&.

56. Chialvo, A.A., et al., *Solvation in high-temperature electrolyte solutions. I. Hydration shell behavior from molecular simulation.* Journal of Chemical Physics, 1999. **110**(2): p. 1064-1074.

57. Ohtaki, H. and T. Radnai, *Structure and Dynamics of Hydrated Ions.* Chemical Reviews, 1993. **93**(3): p. 1157-1204.

58. Jackson, J.D., *Classical electrodynamics*. 3rd ed1999, New York: Wiley. xxi, 808 p.

59. Griffiths, D.J., *Introduction to electrodynamics*. 3rd ed1999, Upper Saddle River, N.J.: Prentice Hall. xv, 576 p.

60. Vandervoort, P.O., *The relativistic motion of a charged particle in an inhomogeneous electromagnetic field.* Annals of Physics, 1960. **10**(3): p. 401-453.

61. Lauterbur, P.C., *Image Formation by Induced Local Interactions - Examples Employing Nuclear Magnetic-Resonance.* Nature, 1973. **242**(5394): p. 190-191.

62. Ozturk, C., J.A. Derbyshire, and E.R. McVeigh, *Estimating Motion From MRI Data.* Proc IEEE Inst Electr Electron Eng, 2003. **9**(10): p. 1627-1648.

63. Stejskal, E.O. and J.E. Tanner, *Spin Diffusion Measurements: Spin Echoes in the Presence of a Time-Dependent Field Gradient.* Journal of Chemical Physics, 1965. **42**(1): p. 288-+.

64. Elkins, C.J. and M.T. Alley, *Magnetic resonance velocimetry: applications of magnetic resonance imaging in the measurement of fluid motion.* Experiments in Fluids, 2007. **43**(6): p. 823-858.

65. Strang, G. and Massachusetts Institute of Technology., *Computational science and engineering*2007, Wellesley, MA: Wellesley-Cambridge Press. xi, 713 p.

66. Pourtaheri, N., et al., *Thresholds for Transverse Stimulation: Fiber Bundles in a Uniform Field.* Ieee Transactions on Neural Systems and Rehabilitation Engineering, 2009. **17**(5): p. 478-486.

67. Kwan, R.S., A. Evans, and G.B. Pike, *An extensible MRI simulator for post-processing evaluation*, in *Visualization in Biomedical Computing*, K. Höhne and R. Kikinis, Editors. 1996, Springer Berlin Heidelberg. p. 135-140.

68. Macovski, A., *Noise in MRI.* Magnetic Resonance in Medicine, 1996. **36**(3): p. 494-497.

69. Geddes, L.A. and L.E. Baker, *The specific resistance of biological material--a compendium of data for the biomedical engineer and physiologist.* Med Biol Eng, 1967. **5**(3): p. 271-93.

70. Alitto, H.J., et al., *A comparison of visual responses in the lateral geniculate nucleus of alert and anaesthetized macaque monkeys.* The Journal of Physiology, 2011. **589**(1): p. 87-99.

71. Norheim, E.S., et al., *A minimal mechanistic model for temporal signal processing in the lateral geniculate nucleus.* Cognitive Neurodynamics, 2012. **6**(3): p. 259-281.

72. Barber, T.W., J.A. Brockway, and L.S. Higgins, *THE DENSITY OF TISSUES IN AND ABOUT THE HEAD.* Acta Neurologica Scandinavica, 1970. **46**(1): p. 85-92.

73. Furuse, M., et al., *Thermal analysis on water components in brain tissue--quantitative determination of free and bound water fractions.* No to shinkei = Brain and nerve, 1987. **39**(8): p. 761-767.

74. Sykova, E. and C. Nicholson, *Diffusion in brain extracellular space.* Physiol Rev, 2008. **88**(4): p. 1277-340.

75. Cserr, H.F., et al., *Efflux of radiolabeled polyethylene glycols and albumin from rat brain.* Am J Physiol, 1981. **240**(4): p. F319-28.

76. Rosenberg, G.A., W.T. Kyner, and E. Estrada, *Bulk flow of brain interstitial fluid under normal and hyperosmolar conditions.* Am J Physiol, 1980. **238**(1): p. F42-9.

Biography

Navid Pourtaheri was born in Buffalo, NY and raised in New Orleans, LA. He attended Tulane University in New Orleans, where he received Bachelor's degrees in electrical engineering and in computer engineering, with minors in math and business in 2003. He then attended Duke University in Durham, NC where he received a Master's degree in biomedical engineering before starting medical school at Duke University in 2008. He completed the PhD and MD degrees at Duke in May 2013.

Navid's academic honors while at Duke included the: Alpha Omega Alpha Society inducted as a junior medical student in 2011, Barham merit-based scholarship awarded for medical school, Albert Schweitzer Fellowship awarded in 2010, Samuel D. Cook Society Award in 2011, John A. Feagin Leadership Scholars Program in 2010-2011, Duke Community Care Fund grant two-time recipient in 2011, 2012, Doing Good in the Neighborhood Grant two-time recipient in 2009, 2010.

Navid's activities while at Duke University included: founding the largest health education outreach program at the School of Medicine, entitled "Duke Med Elementary" in 2008, President of the Davison Council medical student body in 2010-2011, member of the Duke University Board of Trustees Medical Center Academic Affairs Committee in 2010-2011, and member of the Enterprise Wide Planning Committee in 2012 where he was engaged as the only student in a six-month health system wide reform process.

After graduating, Navid will train in a six-year plastic and reconstructive surgery residency program at Case Western Reserve University in Cleveland, Ohio. Navid has aspirations for a career in which he will practice plastic surgery and conduct research in the biomedical sciences at an academic medical center.

Publications and presentations from graduate work

Pourtaheri, N., Truong, T-K., Henriquez, CS. "Study of Lorentz Effect Imaging in Neuronal Current MRI using Electromagnetohydrodynamic Models." Journal of Magnetic Resonance. *Manuscript in progress.*

Pourtaheri, N., Truong, T-K., Henriquez, CS. "Electromagnetohydrodynamic Modeling of Lorentz Effect Imaging." Journal of Magnetic Resonance. *Submitted, in review.*

Pourtaheri, N., Ying, W., Kim, JM., Henriquez, CS. "Thresholds for Transverse Stimulation: Fiber Bundles in a Uniform Field." IEEE Transactions on Neural Systems and Rehabilitation Engineering. Page(s): 478-486. Oct. 2009.

Ying, W, Pourtaheri, N, Henriquez, CS. "Field Stimulation of Cells in Suspension: Use of a Hybrid Finite Element Method." EMBS 28th Annual International Conference, NY, NY. Sept. 2006. *Proceedings paper and podium presentation.*

Pourtaheri, N, Truskey, GA. "Real-Time Theoretical Compartmental Model of Blood-Brain Barrier Drug Delivery." EMBS 26th Annual International Conference, San Francisco, CA. Sept. 2004. *Proceedings paper and podium presentation.*

Pourtaheri, N. "1-D Blood Vessel Modeling: Vessel Area and Flow Rate Control.". EMBS 25th Annual International Conference, Cancun, MX. Sept. 2003. *Proceedings paper and podium presentation.*

Pourtaheri, N., Truong, T-K., Henriquez, CS. "Electromagnetohydrodynamic Modeling in Lorentz Effect MRI" Duke University School of Medicine AOA Day, Durham, NC. Aug. 2012. *Abstract and poster presentation.*

Pourtaheri, N, Ying, W, Henriquez, CS. "Near-Field Stimulation of Axon Bundle Cross-Sections.". BMES Annual Meeting, Chicago, IL. Oct. 2006. *Abstract and poster presentation.*